

1-1-2009

The effect of temperature on fatigue strength and damage of FRP composite laminates

Hossein Mivehchi
Ryerson University

Follow this and additional works at: <http://digitalcommons.ryerson.ca/dissertations>

 Part of the [Mechanical Engineering Commons](#)

Recommended Citation

Mivehchi, Hossein, "The effect of temperature on fatigue strength and damage of FRP composite laminates" (2009). *Theses and dissertations*. Paper 903.

130498

THE EFFECT OF TEMPERATURE ON FATIGUE STRENGTH AND DAMAGE OF FRP COMPOSITE LAMINATES

By

Hossein Mivehchi

B.Sc. in Physics,

Guilan University, Rasht, Iran, 2004

A thesis

presented to Ryerson University,

in partial fulfilment of the

requirements for the degree of

Master of Applied Science

in the program of

Mechanical Engineering

Toronto, Ontario, Canada, 2009

© Hossein Mivehchi

PROPERTY OF
RYERSON UNIVERSITY LIBRARY

A problem worthy of attack proves its worth by fighting back.

E. G. HARDY.

AUTHOR'S DECLARATION

I hereby declare that I am the sole author of this thesis.

A handwritten signature in black ink, appearing to read "S. Micheli". The signature is written in a cursive style with a long horizontal stroke at the end.

I authorize the Ryerson University to lend this thesis to other institutions or individuals for the purpose of scholarly research.

I further authorize the Ryerson University to reproduce this thesis by photocopying or by other means, in total or in part, at the request of other institutions or individuals for the purpose of scholarly research.

Ryerson University requires the signatures of all persons using or photocopying this thesis.
Please sign below, and give address and date.

ACKNOWLEDGEMENTS

I would like to extend my deepest thanks to my advisor Professor Ahmad Varvani-Farahani for his encouragement, advice, and support. He has provided me with guidance, inspiration, and motivation, and he definitely contributed to the success of this work very much.

I would like to express my sincerest appreciation to my lovely parents and siblings for their love, patience, inspiration, and unconditional support. This work undoubtedly owes a lot to them.

I would also like to thank my friends who morally supported me over the period of this study, particularly Dr. Hossein Haftchenari, Dr. Amir Zabet-Khosousi, and Mr. Alireza Shirazi for their availability and constructive comments.

Also, the financial support of NSERC of Canada, through Professor Ahmad Varvani-Farahani of the Department of Mechanical and Industrial Engineering, Ryerson University, is greatly appreciated.

And, Thanks to God for all the blessings He has given me.

ABSTRACT

The Effect of Temperature on Fatigue Strength and Damage of FRP Composite Laminates, Hossein Mivehchi, Masters of Applied Science Thesis in Mechanical Engineering, Ryerson University, Toronto, Canada, 2009.

The present study intends to investigate the effect of temperature on cumulative fatigue damage of laminated fibre-reinforced polymer (FRP) composites. The effect of temperature on fatigue damage is formulated based on a previously proposed residual stiffness fatigue damage model. The fatigue strength of FRP composite laminates is also formulated to have temperature dependent parameters.

This research work is divided into three main parts: the first part reviews the fatigue damage mechanism in fibre-reinforced composites based on stiffness degradation. The recent residual stiffness model of Varvani-Shirazi was used as the backbone structure of damage analysis in this thesis. This model is capable of damage assessment while the effects of maximum stress, stress ratio and fibre orientation of FRP composites were recognized. The Varvani-Shirazi damage model was further developed to assess fatigue damage of FRP composites at various temperatures (T). Inputs of the damage model are temperature dependent parameters including Young's modulus (E), ultimate tensile strength (σ_{ult}), and fatigue life (N_f). As the next part of the proposed analysis, the temperature dependency of each parameter is formulated, and the relations of $E-T$ and $\sigma_{ult}-T$ are substituted in the Varvani-Shirazi fatigue model. Finally, all terms and equations are evaluated with the experimental data available in the literature.

Six sets of fatigue data were used in this thesis to evaluate fatigue damage of FRP specimens. The predicted results were found to be in good agreement with the experimentally obtained data. The proposed fatigue damage model was found promising to predict the fatigue damage of unidirectional (UD) and woven FRP composites at different temperatures. Temperature dependant parameters of Young's modulus, ultimate tensile strength, and S-N diagram were also found to be responsive when used for UD, cross-ply, and quasi-isotropic FRP laminates.

TABLE OF CONTENTS

AUTHOR'S DECLARATION	iii
ACKNOWLEDGEMENTS	v
ABSTRACT	vi
TABLE OF CONTENTS	vii
LIST OF FIGURES	x
LIST OF TABLES	xv
NOMENCLATURE	xvi
OBJECTIVE AND SCOPE OF THE THESIS	xix
PREFACE	xxi
CHAPTER 1: Introduction and Application of FRP Composites	1
1.1 Introduction.....	1
1.2 Applications of FRP Composites.....	3
CHAPTER 2: Material Characteristics and Stress/Strain Constitutive Relation in FRP Composites	6
2.1 Fibre-Reinforced Composite.....	6
2.1.1 Mechanical Properties of GFRP and CFRP Composites.....	8
2.1.1.1 Glass Fibre-Reinforced Polymer Composites.....	8
2.1.1.2 Mechanical Properties of GFRP and CFRP Composites.....	9
2.2 Strains and Stresses.....	10
2.3 Effect of Fibre Orientation on the Strengths of Unidirectional FRP Composites	14
2.3.1 Young's and Shear Moduli of Off-Axis Unidirectional FRP Composites	15

2.3.2 Ultimate Tensile Strength of Off-Axis Unidirectional FRP Composites	18
CHAPTER 3: Fatigue Damage and Temperature Effect in FRP Composites.....	22
3.1 The Concept of Cumulative Fatigue Damage in FRP Composites.....	22
3.2 Fatigue Damage Models for FRP Composites.....	24
3.2.1 Ramakrishnan- Jayaraman Model.....	24
3.2.2 Varvani- Shirazi Model.....	25
3.3 Effect of Temperature on Fatigue Damage.....	26
3.4 Effect of Temperature on Young's Modulus and Tensile Strength	26
3.4.1 Young's Modulus and Temperature	27
3.4.2 Ultimate Tensile Strength and Temperature	29
CHAPTER 4: Temperature Dependent Fatigue Damage Model and its Parameters for FRP Composites.....	30
4.1 Mechanical Properties and Temperature Effect.....	30
4.2 The Proposed Temperature Dependant Relations for Monotonic Properties	31
4.3 The Elements of Proposed Temperature Dependent Relations	33
4.3.1 Temperature Variables.....	33
4.3.2 $E(T_0)$ and $\sigma_{ult}(T_0)$ and Temperature Effect on Tsai-Hill Relationship	33
4.3.3 Constant C in Shift Factor Relation.....	34
4.4 Fatigue Strength and Temperature.....	35
4.4.1 Temperature Effect on Intercept (A).....	36
4.4.2 Temperature Effect on Slope (m).....	37
4.5 Inclusion of Temperature Dependent Parameters in Fatigue Damage Model	39
4.5.1 Algorithm/Flowchart of Fatigue Damage Analysis for FRP Composites	40
CHAPTER 5: Evaluation of the Temperature Dependent Analysis and Results.....	42

5.1 Evaluation of the Temperature Dependent Monotonic Properties Model	42
5.1.1 Jen <i>et al.</i> Data.....	42
5.1.2 Shen and Springer Data	42
5.1.3 Calculated $\sigma_{ult}(T)$ and $E(T)$ Results.....	43
5.2. Evaluation of the Fatigue S-N Relation.....	56
5.2.1 Jen <i>et al.</i> Data.....	56
5.2.2 Kawai and Taniguchi Data.....	56
5.2.3 Calculated Fatigue S-N Results	57
5.3 Evaluation of the Fatigue Damage Model	73
5.3.1 Calculated Fatigue Damage Model Results.....	73
CHAPTER 6: Discussion of Results	80
6.1 General Outlook.....	80
6.2 Temperature and the Monotonic Properties.....	81
6.3 Temperature and Fatigue Strength.....	83
6.4 Temperature and Fatigue Damage	86
CHAPTER 7: Conclusion and Recommendation	88
7.1 Conclusion	88
7.2 Recommendation	89
REFERENCES.....	91
APPENDIX A: Testing Conditions and Mechanical Properties	96
APPENDIX B: Experimental Data	103

LIST OF FIGURES

Figure 2.1: A simple on-axis unidirectional composite lamina under tensile loading.	6
Figure 2.2: Schematic illustration of the stress-strain curves of composite and its fibre and matrix phases.....	7
Figure 2.3: The global x, y, z and the local 1, 2, 3 coordinate systems.	12
Figure 2.4: The stresses in the global x, y, z and the local 1, 2, 3 coordinate systems [21].	12
Figure 2.5: Stress-strain curves of polyester resin, glass fibre, and GRP composite: (a) matrix: polyester, (b) fibre: glass fibre, and (c) GRP composite [21].	13
Figure 2.6: Stress-strain response for CFRP composite: (a) tensile test, and (b) shear test [21].	14
Figure 2.7: An off-axis UD specimen under plane stress condition.	15
Figure 2.8: (a) The elastic modulus and (b) the shear modulus of GRP as off-axis angle changes [21].	17
Figure 2.9: (a) The elastic modulus and (b) the shear modulus of CFRP composite as off-axis angle changes [21].	18
Figure 2.10: Variation of tensile strength versus off-axis angles for GRP and CFRP [21].	18
Figure 2.11: An off-axis UD specimen under uniaxial tension and plane stress condition.	20
Figure 3.1: Three regions of cracking mechanism in unidirectional composites.	22
Figure 3.2: Temperature dependence of Young's modulus in a typical polymer.	28
Figure 3.3: Temperature dependence of Young's modulus in typical laminated FRP composites.	28
Figure 4.1: A typical curve of $\sigma_{ult} - T$ or $E - T$ plotted with Equations (4.9) or (4.10) in the defined cases.	35
Figure 4.2: Illustration of intercept-temperature curve generated using Equation (4.17).	37
Figure 4.3: Typical illustration of slope-temperature curve plotted using Equation (4.18).	38
Figure 4.4: Flowchart of generalized material property degradation technique.	40

Figure 5.1: (a) Ultimate tensile strength and (b) tensile modulus of 0° boron/epoxy as a function of temperature. Data of Ref. 33 modeled by Equations (4.9) and (4.10), respectively.	44
Figure 5.2: (a) Ultimate tensile strength and (b) tensile modulus of 0° aramid/epoxy as a function of temperature. Data of Ref. 33 modeled by Equations (4.9) and (4.10), respectively.	45
Figure 5.3: (a) Ultimate tensile strength and (b) tensile modulus of 0° S-glass/epoxy as a function of temperature. Data of Ref. 33 modeled by Equations (4.9) and (4.10), respectively.	46
Figure 5.4: (a) Ultimate tensile strength and (b) tensile modulus of 0° E-glass/epoxy as a function of temperature. Data of Ref. 33 modeled by Equations (4.9) and (4.10), respectively.	47
Figure 5.5: (a) Ultimate tensile strength and (b) tensile modulus of 0° alumina/PEEK as a function of temperature. Data of Ref. 33 modeled by Equations (4.9) and (4.10), respectively.	48
Figure 5.6: (a) Ultimate tensile strength and (b) tensile modulus of [0/90] _{4S} AS-4/PEEK as a function of temperature. Data of Ref. 34 modeled by Equations (4.9) and (4.10), respectively.	49
Figure 5.7: (a) Ultimate tensile strength and (b) tensile modulus of [0/+45/90/-45] _{2S} AS-4/PEEK as a function of temperature. Data of Ref. 34 modeled by Equations (4.9) and (4.10), respectively.	50
Figure 5.8: (a) Ultimate tensile strength and (b) buckling modulus of 90° Thornel 300/Fiberite 1034 as a function of temperature. Data of Refs. 28 and 29 modeled by Equations (4.9) and (4.10), respectively.	51
Figure 5.9: (a) Ultimate tensile strength and (b) tensile modulus of 90° Thornel 300/Narmco 5208 as a function of temperature. Data of Refs. 28 and 29 modeled by Equations (4.9) and (4.10), respectively.	52

Figure 5.10: (a) Ultimate tensile strength and (b) tensile modulus of 90° HT-S/(8183/137-NDA-BF₃:MEA) as a function of temperature. Data of Refs. 28 and 29 modeled by Equations (4.9) and (4.10), respectively. 53

Figure 5.11: (a) Ultimate tensile strength of 90° Hercules AS-5/3501 as a function of temperature. Data of Ref. 28 modeled by Equation (4.9). 54

Figure 5.12: (a) Ultimate tensile strength of 90° boron/Narmco 5505 as a function of temperature. Data of Ref. 28 modeled by Equation (4.9). 54

Figure 5.13: (a) Tensile modulus of 90° Courtaulds HMS/Hercules 3002M as a function of temperature. Data of Ref. 29 modeled by Equation (4.10). 55

Figure 5.14: The relationships of (a) intercept and (b) slope with temperature for [0/90]_{4S} AS-4/PEEK respectively modeled by Equations (4.17) and (4.18) and correlated with the experimentally obtained intercepts and slopes. 58

Figure 5.15: S-N equations of [0/90]_{4S} AS-4/PEEK at different temperatures. Data extracted from Ref. 34 modeled by Equation (4.20). 59

Figure 5.16: Comparison of experimental fatigue lives extracted from Ref. 34 with the fatigue lives predicted with Equation (4.20) for [0/90]_{4S} AS-4/PEEK at different temperatures. 60

Figure 5.17: The relationships of (a) intercept and (b) slope with temperature for [0/+45/90/-45]_{2S} AS-4/PEEK respectively modeled by Equations (4.17) and (4.18) and correlated with the experimentally obtained intercepts and slopes. 61

Figure 5.18: S-N equations of [0/+45/90/-45]_{2S} AS-4/PEEK at different temperatures. Data extracted from Ref. 34 modeled by Equation (4.20). 62

Figure 5.19: Comparison of experimental fatigue lives extracted from Ref. 34 with the fatigue lives predicted with Equation (4.20) for [0/+45/90/-45]_{2S} AS-4/PEEK at different temperatures. 63

Figure 5.20: The relationships of (a) intercept and (b) slope with temperature for plain-woven (15°) T300/Epoxy#2500 respectively modeled by Equations (4.17) and (4.18) and correlated with the experimentally obtained intercepts and slopes. 64

Figure 5.21: S-N equations of plain-woven (15°) T300/Epoxy#2500 at different temperature Data extracted from Ref. 40 modeled by Equation (4.20).	6
Figure 5.22: Comparison of experimental fatigue lives extracted from Ref. 40 with the fatigue lives predicted with Equation (4.20) for plain-woven (15°) T300/Epoxy#2500 at different temperatures.	6
Figure 5.23: The relationships of (a) intercept and (b) slope with temperature for plain-woven (30°) T300/Epoxy#2500 respectively modeled by Equations (4.17) and (4.18) and correlated with the experimentally obtained intercepts and slopes.....	6
Figure 5.24: S-N equations of plain-woven (30°) T300/Epoxy#2500 at different temperatures: Data extracted from Ref. 40 modeled by Equation (4.20).	6
Figure 5.25: Comparison of experimental fatigue lives extracted from Ref. 40 with the fatigue lives predicted Equation (4.20) for plain-woven (30°) T300/Epoxy#2500 at different temperatures.	6
Figure 5.26: The relationships of (a) intercept and (b) slope with temperature for plain-woven (45°) T300/Epoxy#2500 respectively modeled by Equations (4.17) and (4.18) and correlated with the experimentally obtained intercepts and slopes.....	7
Figure 5.27: S-N equations of plain-woven (45°) T300/Epoxy#2500 at different temperatures: Data extracted from Ref. 40 modeled by Equation (4.20).	7
Figure 5.28: Comparison of experimental fatigue lives extracted from Ref. 40 with the fatigue lives predicted with Equation (4.20) for plain-woven (45°) T300/Epoxy#2500 at different temperatures.	7
Figure 5.29: Fatigue damage of glass cloth/polyvinyle ester versus number of cycles under σ_{max} $=130$ MPa, $f = 16.7$ Hz, and $R = 0$ at 298 K. Data of Ref. 41 modeled by Equation (4.21).	7
Figure 5.30: Fatigue damage of glass cloth/polyvinyle ester versus number of cycles under σ_{max} $=130$ MPa, $f = 16.7$ Hz, and $R = 0$ at 323 K. Data of Ref. 41 modeled by Equation (4.21).	7

Figure 5.31: Fatigue damage of glass cloth/polyvinyle ester versus number of cycles under $\sigma_{max} = 130$ MPa, $f = 16.7$ Hz, and $R = 0$ at 343 K. Data of Ref. 41 modeled by Equation (4.21).	76
Figure 5.32: Fatigue damage of glass mat/polyvinyle ester versus number of cycles under $\sigma_{max} = 90$ MPa, $f = 16.7$ Hz, and $R = 0$ at 298 K. Data of Ref. 41 modeled by Equation (4.21).	77
Figure 5.33: Fatigue damage of glass mat/polyvinyle ester versus number of cycles under $\sigma_{max} = 90$ MPa, $f = 16.7$ Hz, and $R = 0$ at 373 K. Data of Ref. 41 modeled by Equation (4.21).	78
Figure 5.34: Fatigue damage of glass mat/polyvinyle ester versus number of cycles under $\sigma_{max} = 90$ MPa, $f = 16.7$ Hz, and $R = 0$ at 423 K. Data of Ref. 41 modeled by Equation (4.21).	79
Figure 6.1: (a) Ultimate tensile strength and (b) buckling modulus of 90° Thornel 300/Fiberite 1034 as a function of temperature. Data of Refs. 28 and 29 modeled by Equations (4.9) and (4.10), respectively.	82
Figure 6.2: Experimentally obtained S-N curves for $[0/90]_{4S}$ AS-4/PEEK at different temperatures. Data extracted from Ref. 34.	84
Figure 6.3: Experimentally obtained S-N curves for $[0/+45/90/-45]_{2S}$ AS-4/PEEK at different temperatures. Data extracted from Ref. 34.	85
Figure 6.4: Comparison of experimental life data with the predicted fatigue lives of Equation (4.20) for sixteen different sets of data extracted from Refs. 34 and 40.	86
Figure 6.5: Fatigue damage of glass cloth/polyvinyle ester versus number of cycles under $\sigma_{max} = 130$ MPa, $f = 16.7$ Hz, and $R = 0$ at 298 K, 323 K and 343 K. Data of Ref. 41 modeled by Equation (4.21).	87

LIST OF TABLES

Table 2.1: E-glass fibres properties [18].....	9
Table 2.2: Carbon fibres properties [18].....	10

NOMENCLATURE

A	Intercept of S-log N curve
$a(T)$	Temperature-dependant shift factor
B	Bulk moduli
C	Temperature-dependant shift factor constant
CFRP	Carbon Fibre Reinforced Polymer
D	Fatigue Damage
E	Young's modulus (moduli) or modulus of elasticity
E_b	Buckling modulus
E_C	Compressive modulus
E_c	Composite modulus of elasticity
E_f	Fibre modulus of elasticity
E_m	Matrix modulus of elasticity
E_N	Young's modulus of the damaged material in cycle N
E_t	Tensile modulus
E_x	Composite Young's modulus along off-axis direction
E_0	Initial Young's modulus of the undamaged material
E_1	Composite Young's modulus along fibre direction
E_2	Composite Young's modulus normal to fibre direction
f	Fatigue loading frequency
f^*	Fibre/matrix interface strength parameter
FRP	Fibre-Reinforced Polymer

GFRP	Glass Fibre-Reinforce Polymer or (GRP: Glass-Reinforced Polymer)
G	Shear modulus or moduli
G_C	The gas constant
G_{xy}	Composite shear modulus in x-y plane
G_{12}	Composite shear modulus in 1-2 (fibre/matrix interface) plane
K_f	The portion of the fibre volume fraction in the load direction
m	Slope of S-log N curve
N	Number of fatigue cycles
N_f	Fatigue life or number of cycles to failure
n	The assumed percentage of run-out or drop in stiffness
R	Stress-ratio (minimum stress/maximum stress)
RT	Room Temperature
\bar{S}_{ij}	Elements of the compliance matrix in x, y, z coordinate system
T	Temperature
T_g	Glass transition temperature
T_m	Polymer melting point
T_0	Reference temperature
UD	Unidirectional fibrous composite
V_f	Fibre volume fraction
V_m	Matrix volume fraction
WLF	Williams-Landel-Ferry
γ_{xy}	Engineering shear strain in x-y plane
γ_{12}	Engineering shear strain in 1-2 (fibre/matrix interface) plane
ε	Normal strain or strain

ε_c	Composite fracture strain
ε_{xy}	Normal strain in x-y plane
ε_{11}	Normal strain in fibre direction
$\varepsilon_{22}, \varepsilon_{33}$	Normal strains perpendicular to fibre direction
η	Polymer tensile viscosity
θ	The angle between fibre and the load direction
ν_{12}	Poisson's ratio in 1-2 (fibre/matrix interface) plane
$\Delta\sigma$	Applied cyclic stress range
σ_a	Amplitude cyclic stress
σ_{appl}	Applied tensile fatigue stress
σ_f	Stress in fibre
σ_m	Stress in matrix
σ_{max}	Maximum cyclic stress
σ_{mean}	Mean cyclic stress
σ_{min}	Minimum cyclic stress
σ_{ult}	Ultimate tensile strength
σ_{xy}	Normal stress to x-y plane
σ_{11}	Normal stress in fibre direction
σ_{22}, σ_{33}	Normal stresses perpendicular to fibre direction
τ_{xy}	Shear stress in x-y plane
τ_{12}	Shear stress in 1-2 (fibre/matrix interface) plane

OBJECTIVE AND SCOPE OF THE THESIS

Fibre-reinforced polymer (FRP) composites are extensively used in various industries including aerospace, automotive, sporting goods, marine, electrical, and construction. In comparison with traditional metals and alloy-based structures, FRP composites have superior strength-to-weight ratio, greater corrosion resistance, and high resistance to fatigue failure.

Fatigue failure in FRP composites involves a gradual damage progress when subjected to repeated or fluctuating stresses below the ultimate tensile strength of the material. This damage which is caused by the initiation and accumulation of microcracks results in the degradation of mechanical properties such as strength and stiffness leading to failure of FRP components. The complexity of fatigue damage in FRP composites is that they are inhomogeneous and anisotropic, and therefore crack/damage progress changes its rate over the matrix, fibre, and matrix-fibre interface.

The mechanical properties of FRP composites as viscoelastic materials are significantly influenced by temperature variation. FRP components working at various operating temperatures show an increasing trend in degradation of mechanical properties and therefore a non-uniform triphasic failure mechanism.

The present study intends to investigate the effect of temperature on fatigue strength and damage of FRP composite laminates. The fatigue damage analysis has been developed based on the stiffness reduction of materials in a triphasic manner including regions of the matrix, the matrix-fibre interface, and the fibre as the number of cycles progresses. The effect of operating temperature variations on the stiffness reduction and strength of FRP composites has been further investigated. This investigation considers the temperature effects on both static and fatigue responses of the FRP composite and its microconstituents in three stages specified as I, II, and III.

The ultimate objective of this study is to achieve a better understanding of the damage mechanism in FRP composites under cyclic loads and in the presence of various

temperatures. This enables engineers to control and predict the stiffness, damage progress and eventual failure life of FRP laminates subjected to fatigue loads at different operating temperatures. This analysis further leads to a more reliable design of machinery parts and components when using such composite laminates under the studied load and environmental conditions.

PREFACE

The following provides a brief description of materials covered in the chapters of this thesis.

Chapter 1 reviews the importance of fatigue damage analysis and the application of laminated FRP composites in industry.

Chapter 2 covers a brief description of material characteristics and the stress/strain constitutive relationship in FRP composites. As two examples, the characteristics of glass fibre-reinforced polymer (GFRP) and carbon fibre-reinforced polymer (CFRP) composites and the mechanical properties of these materials influenced by the matrix, fibre, volume fraction and orientation of the fibre are addressed. In this chapter, the effects of fibre orientation on the elastic moduli and the ultimate tensile strength of unidirectional FRP composites are also analyzed.

Chapter 3 presents the concept of fatigue damage in FRP composites and introduces two recent cumulative fatigue damage models. The concept of temperature effect on the fatigue damage and the temperature dependent static and dynamic mechanical properties affecting the cumulative fatigue damage are discussed.

Chapter 4 includes the derivation and development of the temperature dependent fatigue damage model and its parameters such as Young's modulus, the ultimate tensile strength, and the fatigue strength for FRP composite laminates.

Chapter 5 evaluates the proposed temperature dependent relations with the available experimental data in the literature. The predictions and the experimental data are compared in this chapter.

Chapter 6 discusses all the evaluation results and analyzes the overall efficiency of the proposed relations by comparing them together.

Chapter 7 summarizes the conclusion obtained by this study. It gives the key points related to the temperature dependent fatigue assessment of laminated FRP composites and includes future work recommendations.

Appendix A lists testing conditions and material properties of the FRP composites studied in this thesis and Appendix B tabulates experimentally obtained values of E , σ_{ult} , S-N, and D-N at various operating temperatures extracted from literature.

CHAPTER ONE

Introduction and Application of FRP Composites

1.1 Introduction

Composite materials or composites are formed by combining two or more materials that have quite different mechanical properties. The materials or constituents do not dissolve or blend into each other and maintain their separate (at least microscopic) identities in the composite, but they give the composite unique properties and characteristics that are different from those of the constituents. There are two categories of constituents: matrix and reinforcement. The matrix has a continuous state, and the reinforcement exists in two forms of fibres or particulates. In composites, the reinforcements are surrounded by the matrix material [1]. Changing the volume fraction of the reinforcements in the matrix and also changing their orientation and arrangement in it, allow designers to produce wide varieties of composites with different mechanical properties.

In the last three decades, the field of composite materials has had much rapid advancement. The vast use of these materials in aerospace, automotive, electronics, sporting goods and many other types of industrial equipment has turned them into one of the most interesting topics for research. Among the different research issues, investigating the fatigue behaviour of composites is a challenging and favorable topic.

Fatigue is the phenomenon leading to fracture under repeated or fluctuating stresses having a maximum value less than the ultimate static strength of the material [2]. All materials except glasses are susceptible to fatigue. Almost all engineering components such as connecting rods and crankshafts of engines, steam or gas turbine blades, connections or supports for bridges, railroad wheels and axels, and other parts are subjected to varying loads throughout their working life. And, fatigue is easily the most common and the most imperfectly understood cause

of failure in service [3,4].

One of the earliest papers on fatigue of metals was published in 1867, by A. Wohler, a German engineer [5]. However, research on the fatigue performance of advanced composites started at the beginning of the 1970s, just after their introduction, with glass, boron and carbon fibre composites. These early works served as a basis for later understanding of the complex fatigue behaviour of composites [6].

In general, the fatigue of composite materials is quite a complex phenomenon, and an extensive research effort is being spent on it today. Composite materials are inhomogeneous and anisotropic, and their behaviour is more complicated than that of homogeneous and isotropic materials such as metals. The main reasons for this are the occurrence of different damage types, their interactions and their different growth rates in composites. Damages of composites in their constituents include fibre fracture, matrix cracking, matrix crazing, fibre buckling, fibre-matrix interface failure, and delamination [7].

Some of the parameters that influence the fatigue performance of composites are:

- fibre type (e.g., carbon, glass, and aramid),
- matrix type (polymeric (thermoset resins and thermoplastics), metallic, and ceramic),
- type of reinforcement structure (e.g., unidirectional (continuous and discontinuous), woven, knitted, and braided),
- type of FRP composite structure (laminated, sheet molded compound, and injection molded),
- laminate stacking sequence (e.g., unidirectional, angle ply, and cross ply),
- environmental conditions (e.g., temperature, moisture, and UV radiation), and
- loading conditions (e.g., maximum stress, stress ratio R , and cycling frequency).

In this research, among the large number of criteria affecting the fatigue behaviour of composites, the effect of temperature on the fatigue damage of unidirectional fibre-reinforced polymer (FRP) composites is discussed mainly. In fact, this goal is conducted based on two previously proposed fatigue damage models [8,9]. The models have already considered the

effects of maximum stress, stress ratio and fibre orientation on the cumulative fatigue damage of FRP composites.

The major fatigue models and life time methodologies for FRP composites are classified in three categories: (i) fatigue life models, which do not take into account the actual degradation mechanisms, such as matrix cracks and fibre fracture, but use S-N curves or Goodman-type diagrams and introduce some sort of fatigue failure criteria [7,10-12], (ii) phenomenological models for residual stiffness/strength [7-9,13,14], and (iii) progressive damage models which use one or more damage variables related to measurable manifestations of damage (transverse matrix cracks, delamination size) [7,15-17].

The fatigue damage model employed in this study is constructed based on stiffness degradation of materials over life cycles. Stiffness degradation damage models [8,9,13] are reliable approaches relating damage progress of FRP composite material properties, including the properties of the matrix, fibre, and fibre-matrix interface as the number of stress cycles progresses. One of such damage models developed lately [9] is extensively used in this thesis. Mechanical properties of FRP composite laminates including their microconstituents are further formulated as a function of operating temperatures. Temperature dependent parameters of Young's modulus, ultimate tensile strength, and fatigue strength as inputs of the damage model characterize the damage of FRP composite specimens. However, before discussing the topics in detail, some applications of the composites are briefly addressed in the rest of this chapter.

1.2 Applications of FRP Composites

Composite materials were first used in aircraft engine rotor blades in the 1960s. Nowadays, composite materials, and especially fibre-reinforced ceramic composites, are vastly considered for many high-temperature applications in advanced aerospace vehicles and gas turbine engine components. The use of composite materials has been shown to reduce major cost due to failure of components and structures [18]. Striking examples of breakthroughs based on the utilization of composite materials and especially fibre-reinforced polymer composites are increasingly found in transportation vehicles (e.g., aircraft, space shuttle, and automobile), civil infrastructure

(e.g., buildings, bridges, and highway barriers), and sporting goods (e.g., tennis rackets, golf clubs, bicycle frames, fishing rods, and sailboats).

FRP composites also have many electrical applications. Some electrical applications include E-glass fibre polymers in transformer housings, motor casings, switch components, and circuit breaker arms. Also, printed circuit boards (PCBs) in electronic packages are made of E-glass fabric reinforced epoxy. The excellent electrical insulation properties and low cost of E-glass fibres and the relatively high resistance of thermoset polymers, such as epoxies, to creep, to elevated temperature, and to chemicals, are the main reasons for their inevitable applications [1].

Glass-reinforced polymers (GRPs) are also applied to make hot tubes, pipes for drinking water, sewers, chemicals, and oil sucker rods. Sucker rods are employed in moving underground oil upwards to the surface. The major advantages of the GRP sucker rods to steel sucker rods are that the GRP rods have less weight and stronger corrosion resistance [1]. Therefore, it is concluded that FRPs and especially GRP composites have both onshore and offshore applications. The most successful offshore applications for composites have been in pipework for aqueous liquids. Performance-based guidelines for the design of glass fibre reinforced epoxy (GRP) pipes have significantly accelerated these applications. The chemical resistance of GRP and the maximum use temperature in a particular fluid depends on the type of resin and hardener used. GRP tubes are largely immune to the effects of hydrogen sulphide and carbon dioxide [18].

Some other industrial applications of FRP composites include the use of the materials in pressure vessels, rollers, and wind turbine blades. Composite pressure vessels are made by filament winding carbon, S-glass, or Kevlar 49 fibre reinforced epoxy around an aluminum alloy or a blow molded high density polyethylene tube. The vessels can be used for the storage of water, diesel, oxygen, nitrogen, and other gases and chemicals. The pressure vessels can also be used as liquid oxygen, nitrogen, hydrogen, and helium tanks. It is known that the temperature of the liquids is in the range of 90 K to 4 K and few materials can stand the cryogenic temperatures. The major advantages of using the FRP composites to other materials as the tanks are that the composites have a lighter weight and are more corrosion resistance. The future is expected to bring more widespread use in tanks, as well as in vessels operating at higher pressures than at

present. This will probably lead eventually to applications in separators and other high pressure processing equipment where thermal and corrosion requirements can be very demanding.

CHAPTER TWO

Material Characteristics and Stress/Strain Constitutive Relation in FRP Composites

2.1 Fibre-Reinforced Composite

Figure 2.1 schematically shows a simple *on-axis* unidirectional composite lamina reinforced with continuous fibres (black strips) which are initially well bonded to the matrix so that, under load, fibres and matrix deform together. The applied load is transferred to the matrix and fibres, and the stress on the composite, σ_c , can be expressed by the rule of mixtures:

$$\sigma_c = \sigma_f V_f + \sigma_m (1 - V_f) \quad (2.1)$$

where σ_f and σ_m are the stresses in the fiber and the matrix, respectively. In Equation (2.1), V_f corresponds to the volume fraction of the fiber, and $(1 - V_f)$ represents the matrix volume fraction or V_m . Generally, when the fibres make an angle with the load direction, the composite is called an *off-axis* unidirectional fibre-reinforced composite.

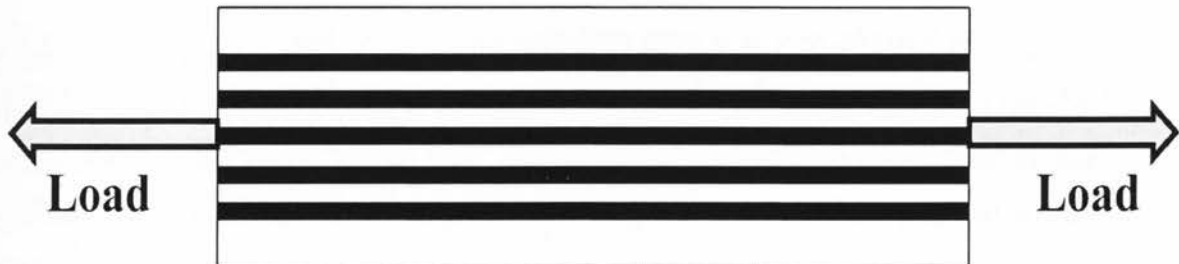


Figure 2.1: A simple on-axis unidirectional composite lamina under tensile loading.

In most practical composites, the high-performance reinforcing fibres are regarded as being brittle, i.e., they deform elastically to failure, showing little or no non-linear deformation. In metal- and polymer-matrix composites, the matrix is usually capable of some irreversible plastic deformation, and, in such materials, the matrix failure strain is usually much greater than that of the fibres.

Figure 2.2 illustrates the difference between stress-strain properties of a composite material and its fibre and matrix phases. In the figure, ϵ_c corresponds to the fracture strain of the composite under a uniaxial tension load. The stiffness of matrix by itself is very low. As fibres are reinforced within the matrix phase, the resulting material becomes a composite with much higher stiffness and strength. Reinforcement fibers with different stiffness can dramatically change the mechanical properties of composites.

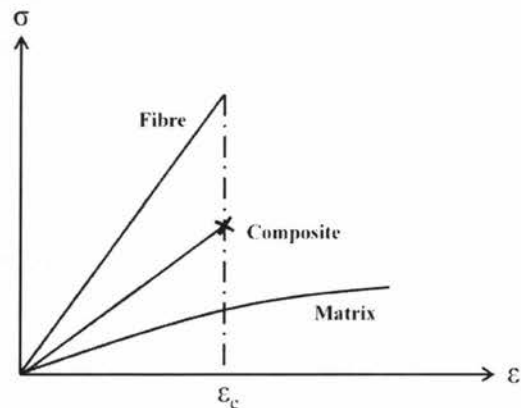


Figure 2.2: Schematic illustration of the stress-strain curves of composite and its fibre and matrix phases.

When reinforcing fibres are loaded perpendicularly to the fibre direction, commonly referred to as the transverse direction, the entire load is not transmitted through the fibre and failure is controlled by rupture or plastic flow of the matrix, or by fibre/matrix separation, and, therefore, the strength of the composites in this direction is relatively weak. In other words, transverse properties of a composite depend on the strength of the interface bond between the fibres and the matrix. If this bond is weak, the transverse properties of the composite material are poor, and poor interface leads to poor transverse strength. Progressive failure of the interfaces leads to what can be interpreted as low

stiffness in the transverse direction. A poor interface results in high resistance to thermal and electrical conduction. Considerable research is directed toward improving the bond at the interface between the fibre and matrix by treating the surface of the fibre before it is combined with the matrix material to form a composite [18].

The type of fibre and matrix, the strength of fibre/matrix interface, and the fibre orientation and concentration have crucial effects on the strength and stiffness of composites including FRP composites. To understand these effects more clearly, the properties of two extensively used FRP composites, namely, glass fibre-reinforced polymer (GFRP) and carbon fibre-reinforced polymer (CFRP) composites, are discussed in the following sections. The effects of fibre orientation on stiffness and strength of the materials are also briefly addressed.

2.1.1 Mechanical Properties of GFRP and CFRP Composites

2.1.1.1 Glass Fibre-Reinforced Polymer Composites

The GFRP composite, popularly called “fibreglass”, is simply a composite consisting of glass fibres contained within a polymer matrix such as polyester, vinyl ester, and epoxy. The glass that is drawn into fibres is generally composed of SiO_2 , Al_2O_3 , and smaller amounts of other oxides. The glass fibre type “E” is the most widely used for composites [19]. It has good physical and electrical properties and reasonable weathering ability. In Table 2.1, some typical properties of E-glass fibres are given. There are also other types of glass including “A” and “S”. “A” is a soda-lime glass with poor physical and electrical properties, but it has good resistance to acid attack and is also inexpensive. “S” glass, a silica alumina magnesia mixture, has better strength properties than the others and can be used at higher temperatures, but it is more expensive [4].

Glass fibres for composites have a good combination of properties: moderate stiffness, high strength, and moderate density. Most fibreglass materials are limited to service temperatures below 200°C . To improve the stiffness of GFRPs and their service

temperature to approximately 300°C, high-purity fused silica for the fibres and high-temperature polymers such as the polyimide resins are used [20].

Table 2.1: E-glass fibres properties [18].

Properties	Value	Properties	Value
Fibre diameter	10-20 μm [19]	Coefficient of thermal expansion	$4.7-5 \times 10^{-6} / ^\circ\text{C}$
Tensile strength	1.4-3.45 GPa	Dielectric constant at 1 MHz	6.4
Elongation	1.8-3.2 %	Thermal conductivity	1.04-1.3 W/m/ $^\circ\text{C}$
Tensile modulus	72.4 GPa	Density	2540 Kg/m ³
Poisson's ratio	0.2	Hardness (Vickers 50g-15g)	5.6

2.1.1.2 Carbon Fibre-Reinforced Polymer Composites

The advent of high-modulus carbon (graphite) fibres obtained from continuous polyacrylonitrile (PAN) filaments has caused considerable technical interest in recent years. Although a continuous spectrum of fibre strength and modulus values can be obtained by varying the process details, especially the maximum temperature at which the fibres are pyrolyzed, they are usually marked in the three basic forms often referred to as Types I, II, III fibres. For practical purposes, the fibres can only be used in conjunction with polymeric matrices such as epoxy and polyester resins. Typical properties of carbon fibres are given in Table 2.2.

It should be noted that the high modulus of carbon fibres causes more anisotropy in strength, modulus, and thermal expansion coefficients than similar composites incorporating glass fibres. For instance, as seen in Table 2.2, the thermal expansion of carbon fibres is negative in the longitudinal direction, and it is positive in the transverse direction. For a given type of fibre, the axial tensile strength and modulus of a composite depends on the volume fraction of fibres and only to a slight extent on the resin system employed. The axial compressive strength is substantially lower than the tensile strength.

Table 2.2: Carbon fibres properties [18].

Properties	Value	Properties	Value
Fibre diameter	4-10 μm [20]	Longitudinal and (transverse) coefficient of thermal expansion	$-0.5 \times 10^{-6} / ^\circ\text{C}$ and $(7-12 \times 10^{-6} / ^\circ\text{C})$
Tensile strength	2.4-2.9 GPa	Specific heat	950 J/Kg/ $^\circ\text{C}$
Elongation	1 %	Thermal conductivity	20 W/m/ $^\circ\text{C}$
Tensile modulus	228-276 GPa	Density	1950 Kg/m ³
Poisson's ratio	0.3	Shear modulus	5.5 GPa

2.2 Strains and Stresses

Fibre reinforced polymer (FRP) composites consist of continuous or discontinues brittle fibres embedded in a matrix. Such a composite is heterogeneous (i.e., the properties vary from point to point). On a scale that is large with respect to the fibre diameter, the fibre and matrix properties may be averaged, and the material may be treated as homogeneous. The material is considered to be quasi-homogeneous, which implies that the properties are taken to be the same at every point. These properties are not the same as the properties of either the fibre or the matrix but are a combination of the properties of the constituents.

The study of the stress-strain response of a single layer is assumed to be equivalent to determining the relations between the stresses applied to the bonding surfaces of the layer and the deformations of the layer as a whole. The strain of an individual fibre or element of matrix is of no consequence to this level of analysis. The effect of the fibre reinforcement is smeared over the volume of material, and it is assumed that the two materials, fibre-matrix system, are equivalent to a single homogenous material. This is an important concept because it makes the analysis of a fibre-reinforced composite easier. Equally important is the fact that this single material does not have the same properties in

all directions. A composite system is obviously stronger and stiffer in the fibre direction (direction 1) than in the matrix directions (directions 2 and 3) (See Figure 2.3). In addition, just because the matrix directions are both perpendicular to the fibre direction, the properties in these two directions are not necessarily equal to each other. A material with different properties in three mutually perpendicular directions is called an orthotropic material. Hence, a layer with this characteristic is said to be orthotropic [18]. The 1-2, 1-3 and 2-3 are three planes, and the material properties are symmetric with respect to each of these planes.

In this chapter, equations are presented for calculating the stress and strains when the structure undergoes only small deformations and the material behaves in a linearly elastic manner. A unidirectional FRP composite consists of fibres reinforced within the matrix phase with an off-axis angle θ with respect to the applied loading axis. It is therefore convenient to employ two coordinate systems: a local coordinated system aligned, at a point, with the fibres and a global coordinate system attached to a fixed reference point. Figure 2.3 presents global and local coordinate systems used for fibrous composites. The local and global Cartesian coordinate systems are designated by 1, 2, 3 and x, y, z axes, respectively.

In the x, y, z coordinate system, the normal stresses are denoted by σ_{xx} , σ_{yy} , σ_{zz} and the shear stresses by τ_{xy} , τ_{yz} , τ_{zx} . Accordingly, the corresponding normal and shear strains are ϵ_{xx} , ϵ_{yy} , ϵ_{zz} and γ_{xy} , γ_{yz} , γ_{zx} . In the 1, 2, 3 principal material coordinate system, the normal stresses are denoted by σ_{11} , σ_{22} , σ_{33} and the shear stresses are denoted by τ_{12} , τ_{23} , τ_{32} . The corresponding normal and shear strains are ϵ_{11} , ϵ_{22} , ϵ_{33} and γ_{12} , γ_{23} , γ_{31} , respectively. The symbol γ represents engineering shear strain. Figure 2.4 presents all tensorial stresses in x, y, z and 1, 2, 3 coordinates. Based on the figure, the stiffness matrix, [C], which is obtained by the generalized Hook's law relation for anisotropic materials is a square matrix and has 36 constants. Moreover, the compliance matrix, [S], defined by the inverse of the stress-strain relations is also a 6 by 6 matrix with obviously 36 elements. In this thesis, C_{ij} and \bar{C}_{ij} are considered as the elements of the stiffness matrix in 1, 2, 3 coordinates and x, y, z coordinates, respectively. And, S_{ij} and \bar{S}_{ij} are considered as

the elements of the compliance matrix in 1, 2, 3 and x, y, z coordinates, respectively.

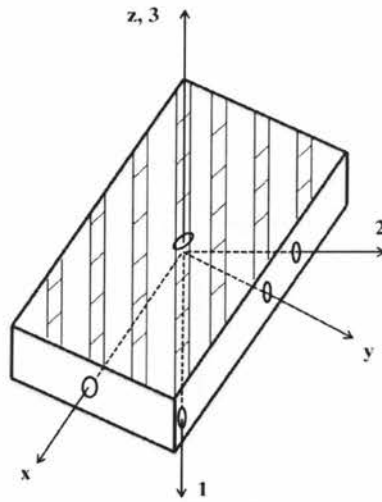


Figure 2.3: The global x, y, z and the local 1, 2, 3 coordinate systems.

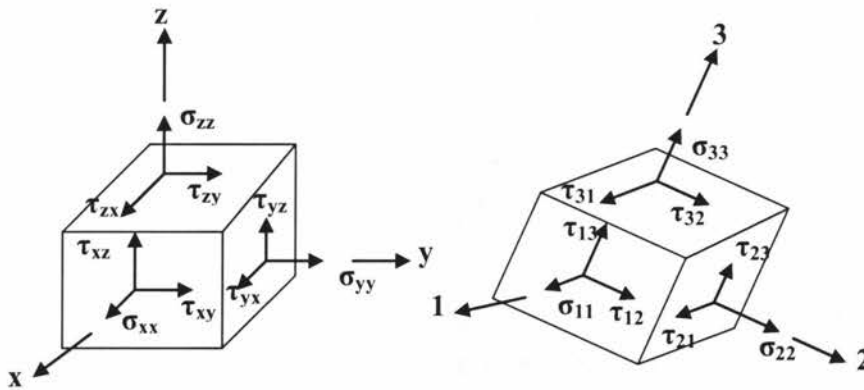


Figure 2.4: The stresses in the global x, y, z and the local 1, 2, 3 coordinate systems [21].

It is noteworthy that, for elastic materials, the stiffness and compliance matrices are symmetric, so only 21 of the 36 constants are independent. In the next section, it will be shown that the matrices can be turned into 3 by 3 matrices for unidirectional FRP composites under plane stress conditions. The tensile stress-strain curves for a glass fibre, polyester resin, and on-axis UD GRP composite are illustrated and compared with each

other in Figure 2.5. These curves show that the glass fibre is a brittle material and has a linear behavior until failure, but the polyester resin is ductile and shows a nonlinear stress-strain curve.

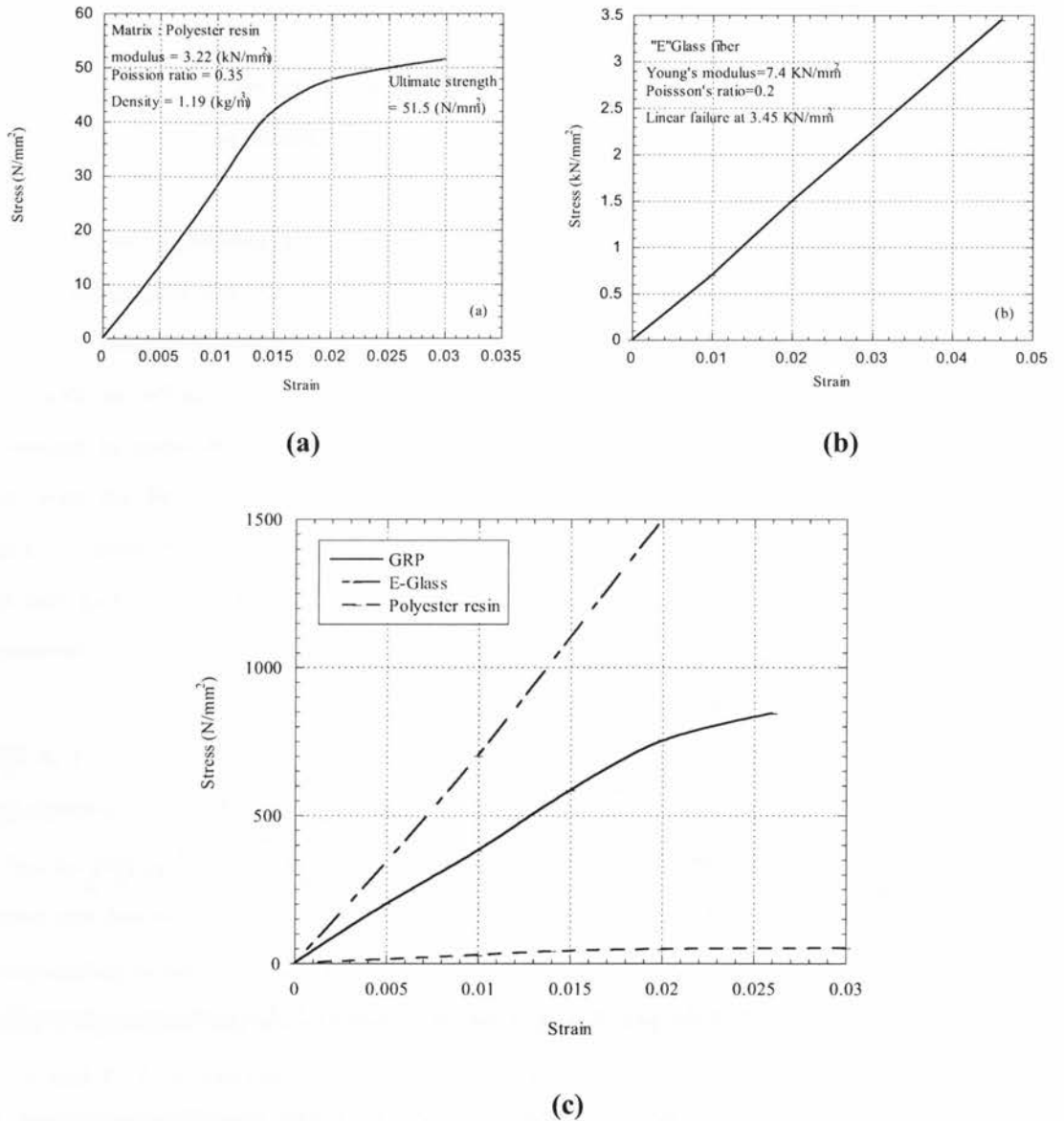


Figure 2.5: Stress-strain curves of polyester resin, glass fibre, and GRP composite: (a) matrix: polyester, (b) fibre: glass fibre, and (c) GRP composite [21].

Figure 2.6a presents the tensile stress-strain curve for a 0° (on-axis) CFRP composite. The curve is almost linear until failure which shows that fibre properties are dominant. Figure 2.6b presents the shear stress-strain curve of the CFRP composite, which is non-linear, and this non-linearity is due to matrix ductility. It is noteworthy to express that, in a tension test, the Young's modulus or moduli, E , can be obtained from the slope of the stress-strain curve in the elastic region (i.e., $E = \sigma/\epsilon$), and in a shearing test, the shear modulus or moduli, G , will be obtained as $G = \tau/\gamma$.

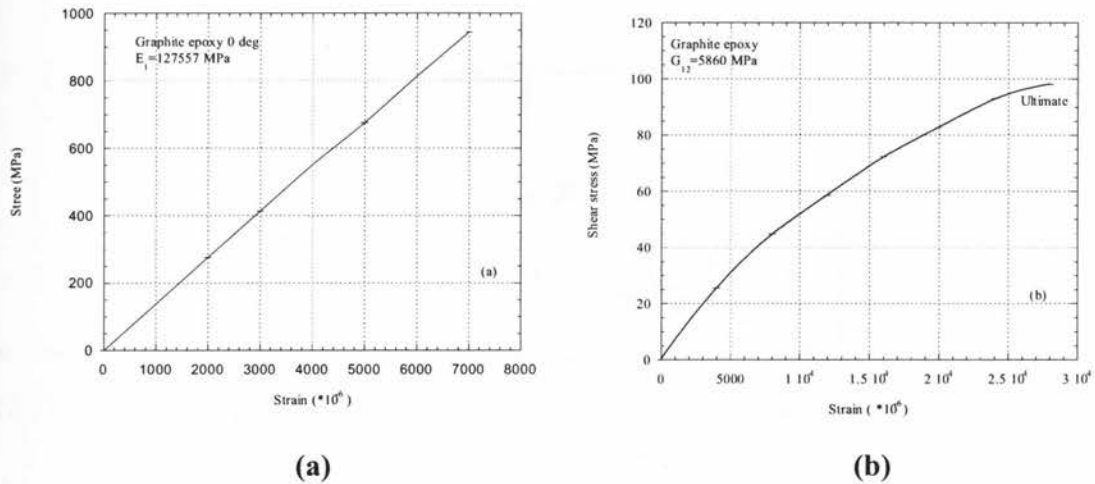


Figure 2.6: Stress-strain response for CFRP composite: (a) tensile test, and (b) shear test [21].

2.3 Effect of Fibre Orientation on the Strengths of Unidirectional FRP Composites

As it was mentioned in the previous section, the stiffness and compliance matrices for anisotropic materials are square matrices with 36 elements. However, in case of having a unidirectional lamina, as seen from Figure 2.3, the planes of material property symmetry are increased, and most of the 36 elements become zero. Moreover, since the lamina cannot withstand high stresses in any direction other than that of the fibres, the stress components in the z and 3 directions can be considered negligible. Therefore, to analyze the strengths of off-axis UD FRP composites, the plane stress condition can be

considered. Figure 2.7 represents an off-axis UD specimen under the plane stress condition of $\sigma_{zz} = \tau_{yz} = \tau_{zx} = 0$ and σ_{xx} , σ_{yy} , and $\tau_{xy} \neq 0$. M_{xy} is the moment in x-y plane.

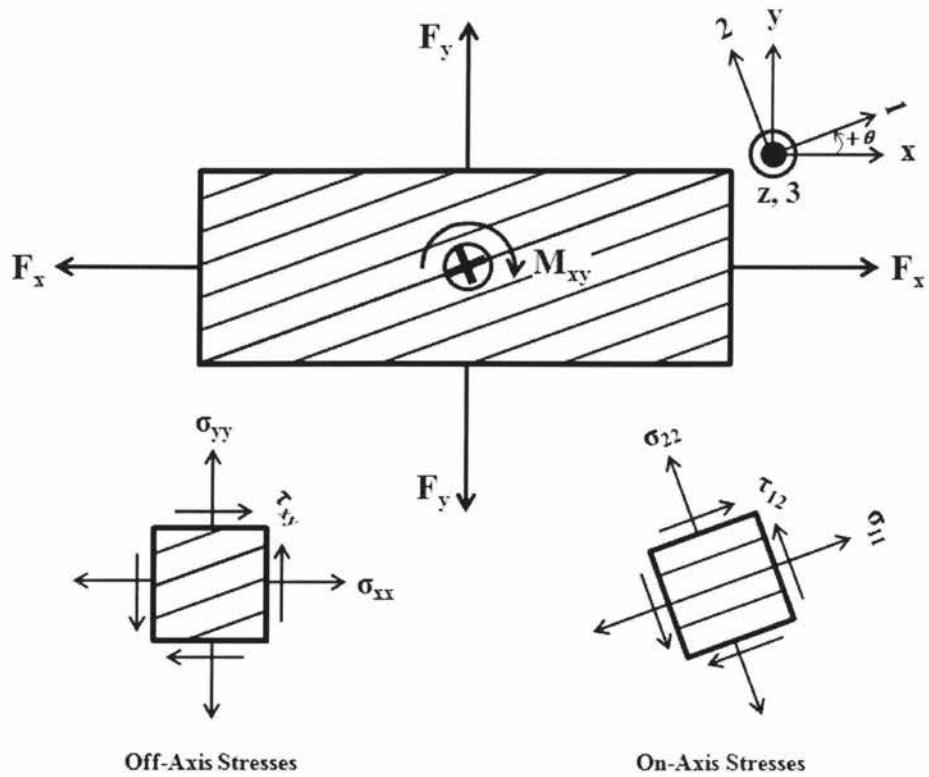


Figure 2.7: An off-axis UD specimen under plane stress condition.

The word “strengths” used in this section is referred to the elastic moduli and the ultimate tensile strength.

2.3.1 Young’s and Shear Moduli of Off-Axis Unidirectional FRP Composites

Based on the plane stress condition, the relationships between stresses and strains in the x-y and 1-2 coordinate systems are written as Equation (2.2) and (2.3), respectively.

$$\begin{bmatrix} \varepsilon_{xx} \\ \varepsilon_{yy} \\ \gamma_{xy} \end{bmatrix} = \begin{bmatrix} \bar{S}_{11} & \bar{S}_{12} & \bar{S}_{16} \\ \bar{S}_{12} & \bar{S}_{22} & \bar{S}_{26} \\ \bar{S}_{16} & \bar{S}_{26} & \bar{S}_{66} \end{bmatrix} \begin{bmatrix} \sigma_{xx} \\ \sigma_{yy} \\ \tau_{xy} \end{bmatrix} \quad (2.2)$$

$$\begin{bmatrix} \varepsilon_{11} \\ \varepsilon_{22} \\ \gamma_{12} \end{bmatrix} = \begin{bmatrix} S_{11} & S_{12} & 0 \\ S_{12} & S_{22} & 0 \\ 0 & 0 & S_{66} \end{bmatrix} \begin{bmatrix} \sigma_{11} \\ \sigma_{22} \\ \tau_{12} \end{bmatrix} \quad (2.3)$$

Due to the plane stress condition, the stiffness matrices in Equations (2.2) and (2.3) are 3 by 3 matrices. Recalled from elementary mechanics of materials, the transformation matrices for expressing stresses and strains in an x-y coordinate system in terms of stresses and strains in a 1-2 coordinate system can respectively be defined as Equations (2.4) and (2.5):

$$\begin{bmatrix} \sigma_{xx} \\ \sigma_{yy} \\ \tau_{xy} \end{bmatrix} = \begin{bmatrix} \cos^2\theta & \sin^2\theta & -2\sin\theta\cos\theta \\ \sin^2\theta & \cos^2\theta & 2\sin\theta\cos\theta \\ \sin\theta\cos\theta & -\sin\theta\cos\theta & \cos^2\theta - \sin^2\theta \end{bmatrix} \begin{bmatrix} \sigma_{11} \\ \sigma_{22} \\ \tau_{12} \end{bmatrix} \quad (2.4)$$

$$\begin{bmatrix} \varepsilon_{xx} \\ \varepsilon_{yy} \\ \gamma_{xy} \end{bmatrix} = \begin{bmatrix} \cos^2\theta & \sin^2\theta & -\sin\theta\cos\theta \\ \sin^2\theta & \cos^2\theta & \sin\theta\cos\theta \\ 2\sin\theta\cos\theta & -2\sin\theta\cos\theta & \cos^2\theta - \sin^2\theta \end{bmatrix} \begin{bmatrix} \varepsilon_{11} \\ \varepsilon_{22} \\ \gamma_{12} \end{bmatrix} \quad (2.5)$$

where θ is the angle between the x-axis to the 1-axis (see Figure 2.7). Using Equations (2.2)–(2.5), \bar{S}_{ij} in Equation (2.2) can be derived from the following Equations:

$$\bar{S}_{11} = S_{11}\cos^4\theta + (2S_{12} + S_{66})\sin^2\theta\cos^2\theta + S_{22}\sin^4\theta \quad (2.6)$$

$$\bar{S}_{12} = S_{12}(\sin^4\theta + \cos^4\theta) + (S_{11} + S_{22} - S_{66})\sin^2\theta\cos^2\theta \quad (2.7)$$

$$\bar{S}_{22} = S_{11}\sin^4\theta + (2S_{12} + S_{66})\sin^2\theta\cos^2\theta + S_{22}\cos^4\theta \quad (2.8)$$

$$\bar{S}_{16} = (2S_{11} - 2S_{12} - S_{66})\sin\theta\cos^3\theta - (2S_{22} - 2S_{12} - S_{66})\sin^3\theta\cos\theta \quad (2.9)$$

$$\bar{S}_{26} = (2S_{11} - 2S_{12} - S_{66})\sin^3\theta\cos\theta - (2S_{22} - 2S_{12} - S_{66})\sin\theta\cos^3\theta \quad (2.10)$$

$$\bar{S}_{66} = 2(2S_{11} + 2S_{22} - 4S_{12} - S_{66})\sin^2\theta\cos^2\theta + S_{66}(\sin^4\theta + \cos^4\theta) \quad (2.11)$$

In Equation (2.3), S_{11} , S_{12} , S_{22} , and S_{66} are equal to the following material properties:

$$S_{11} = \frac{1}{E_1} \quad S_{12} = -\frac{\nu_{12}}{E_1} = -\frac{\nu_{21}}{E_2} \quad S_{22} = \frac{1}{E_2} \quad S_{66} = \frac{1}{G_{12}} \quad (2.12)$$

where, ν_{12} is the Poisson's ratio defined as $-\varepsilon_{22}/\varepsilon_{11}$. So, the relations between the material properties in x-y and 1-2 coordinates can be calculated by Equations (2.13)–(2.16).

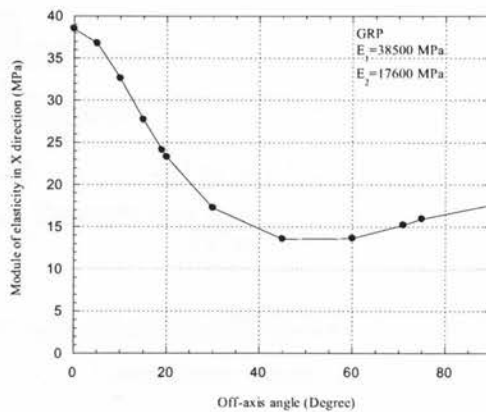
$$\frac{1}{E_x} = \frac{1}{E_1} \cos^4 \theta + \left(\frac{1}{G_{12}} - \frac{2\nu_{12}}{E_1} \right) \sin^2 \theta \cos^2 \theta + \frac{1}{E_2} \sin^4 \theta \quad (2.13)$$

$$\nu_{xy} = E_x \left[\frac{\nu_{12}}{E_1} (\sin^4 \theta + \cos^4 \theta) - \left(\frac{1}{E_1} + \frac{1}{E_2} - \frac{1}{G_{12}} \right) \sin^2 \theta \cos^2 \theta \right] \quad (2.14)$$

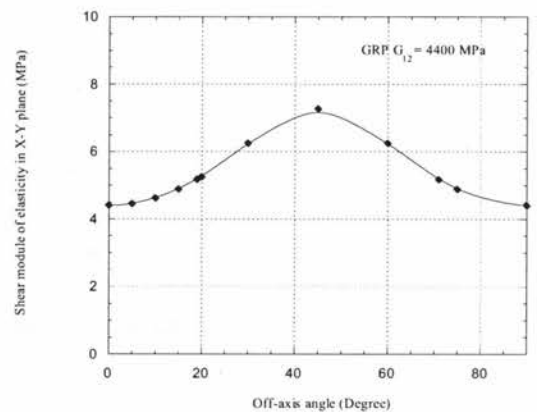
$$\frac{1}{E_y} = \frac{1}{E_1} \sin^4 \theta + \left(\frac{1}{G_{12}} - \frac{2\nu_{12}}{E_1} \right) \sin^2 \theta \cos^2 \theta + \frac{1}{E_2} \cos^4 \theta \quad (2.15)$$

$$\frac{1}{G_{xy}} = 2 \left(\frac{2}{E_1} + \frac{2}{E_2} + \frac{4\nu_{12}}{E_1} - \frac{1}{G_{12}} \right) \sin^2 \theta \cos^2 \theta + \frac{1}{G_{12}} (\sin^4 \theta + \cos^4 \theta) \quad (2.16)$$

In the following, using the above equations, the variations of the shear modulus and Young's modulus for an off-axis GRP and CFRP composite are calculated and shown as a function of the off-axis angle. As Figures 2.8 and 2.9 show, the modulus of elasticity initially possesses the highest value at 0° on-axis angle where the fibres are oriented along the loading axis. The magnitude of the Young's modulus decreases as the off-axis angle increases. Moreover, the figures represent an initial increase of the shear modulus as the off-axis angle increases from zero to a maximum value of 45°. Beyond an off-axis angle of 45°, the shear modulus keeps decreasing as the off-axis angle increases from 45° to 90°. At 90° off-axis angle, the shear modulus becomes as small as the shear modulus achieved at 0°.

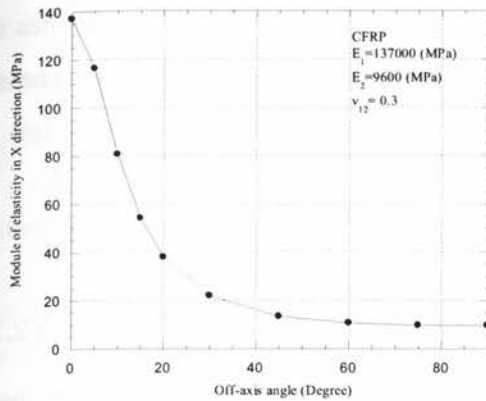


(a)

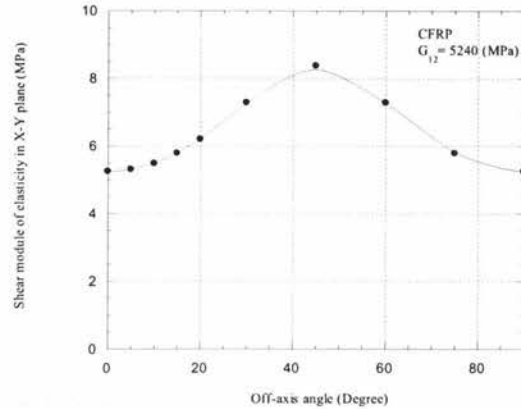


(b)

Figure 2.8: (a) The Young's modulus and (b) the shear modulus of GRP as off-axis angle changes [21].



(a)



(b)

Figure 2.9: (a) The Young's modulus and (b) the shear modulus of CFRP composite as off-axis angle changes [21].

2.3.2 Ultimate Tensile Strength of Off-Axis Unidirectional FRP Composites

Figure 2.10 represents the tensile strength for GRP and CFRP composites. It can be observed that the tensile strength is maximum for 0° plies and drops rapidly with increasing off-axis angles to 90° . The initial dominant failure is due to fiber failure, while the higher off-axis angles failure of the composites is mainly due to matrix cracking.

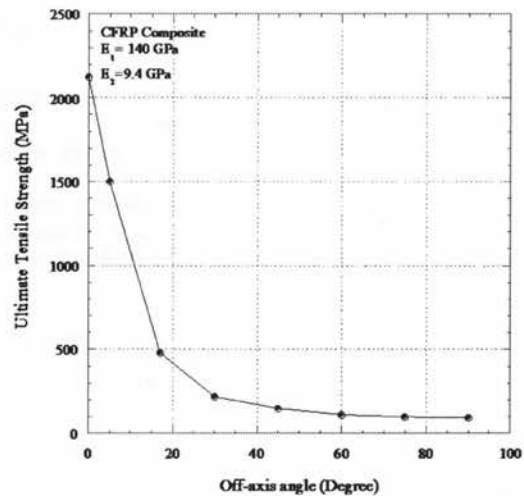
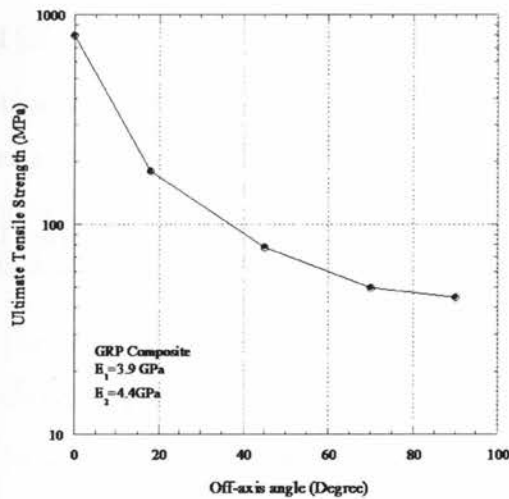


Figure 2.10: Variation of tensile strength versus off-axis angles for GRP and CFRP [21].

To model the ultimate tensile strength of unidirectional fibre-reinforced composites as a function of off-axis angle, many criteria have been proposed. One of the criteria is the so called Tsai-Hill static failure criterion [22,23]. Hill proposed a yield criterion for orthotropic materials [24]:

$$(G + H)\sigma_{11}^2 + (F + H)\sigma_{22}^2 + (F + G)\sigma_{33}^2 - 2H\sigma_{11}\sigma_{22} - 2G\sigma_{11}\sigma_{33} - 2F\sigma_{22}\sigma_{33} + 2L\tau_{23}^2 + 2M\tau_{13}^2 + 2N\tau_{12}^2 = 1 \quad (2.17)$$

Terms F , G , H , L , M , and N are regarded as failure strengths. If only σ_{11} acts on the body, then, because its maximum value is considered as the ultimate tensile strength in the fibre direction, X ,

$$(G + H) = \frac{1}{X^2} \quad (2.18)$$

Equation (2.19) is achieved when σ_{22} is applied:

$$(F + H) = \frac{1}{Y^2} \quad (2.19)$$

where Y is defined as the ultimate tensile strength transverse to the fibre direction. Similarly, if only σ_{33} acts and the strength in the 3-direction is denoted as Z , then

$$(F + G) = \frac{1}{Z^2} \quad (2.20)$$

When shear stress τ_{12} is dominantly applied on the body, Equation (2.21) is obtained:

$$2N = \frac{1}{S^2} \quad (2.21)$$

In Equation (2.21), S is defined as the shear strength acting in 1-2 coordinates. Strengths L and M are also determined using a similar equation to (2.21). The ultimate shear strengths in the 2-3 and 3-1 planes are called U and V , respectively. Using Equations (2.18), (2.19), and (2.20), the following relations between F , G , H and X , Y , and Z are determined:

$$2F = \frac{1}{Y^2} + \frac{1}{Z^2} - \frac{1}{X^2} \quad 2G = \frac{1}{X^2} + \frac{1}{Z^2} - \frac{1}{Y^2} \quad 2H = \frac{1}{X^2} + \frac{1}{Y^2} - \frac{1}{Z^2} \quad (2.22)$$

By considering a plane stress condition in the 1-2 plane of a unidirectional lamina with fibres in the 1-direction, the following relations are obtained:

$$\sigma_{33} = \tau_{23} = \tau_{31} = Z = U = V = 0 \quad (2.23)$$

and

$$\sigma_{11}, X \neq 0 \qquad \sigma_{22}, Y \neq 0 \qquad \tau_{12}, S \neq 0 \qquad (2.24)$$

Substituting Equations (2.18)–(2.22) into Equation (2.17) results in:

$$\frac{\sigma_{11}^2}{X^2} - \left(\frac{1}{X^2} + \frac{1}{Y^2} \right) \sigma_{11} \sigma_{22} + \frac{\sigma_{22}^2}{Y^2} + \frac{\tau_{12}^2}{S^2} = 1 \qquad (2.25)$$

Since Y^2 is much smaller than X^2 , Equation (2.25) can be rewritten as:

$$\frac{\sigma_{11}^2}{X^2} - \frac{\sigma_{11} \sigma_{22}}{X^2} + \frac{\sigma_{22}^2}{Y^2} + \frac{\tau_{12}^2}{S^2} = 1 \qquad (2.26)$$

Figure 2.11 presents an off-axis composite subjected to axial load in the x direction.

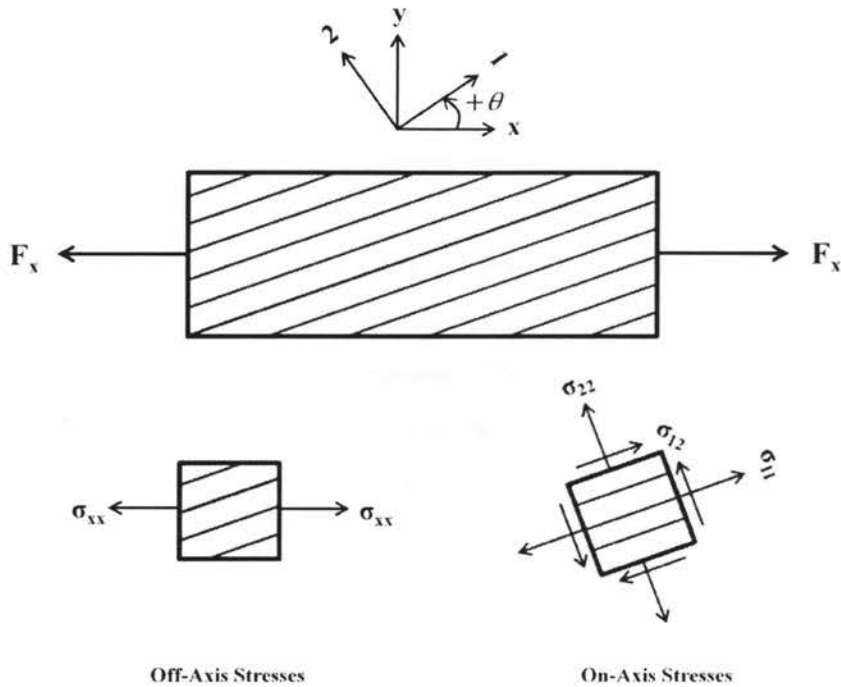


Figure 2.11: An off-axis UD specimen under uniaxial tension and plane stress condition.

The stress-transformation equations for the in-plane stresses in 1-2 and x-y coordinates are defined as:

$$\begin{aligned} \sigma_{11} &= \sigma_{xx} \cos^2 \theta \\ \sigma_{22} &= \sigma_{xx} \sin^2 \theta \\ \tau_{12} &= -\sigma_{xx} \cos \theta \sin \theta \end{aligned} \qquad (2.27)$$

By substituting the relations of Equation (2.27) into Equation (2.26), the Tsai-Hill failure criterion for uniaxial off-axis strength is obtained as:

$$\frac{\cos^4\theta}{X^2} + \left(\frac{1}{S^2} - \frac{1}{X^2}\right) \cos^2\theta \sin^2\theta + \frac{\sin^4\theta}{Y^2} = \frac{1}{\sigma_{xx}^2} \quad (2.28)$$

In Equation (2.28), σ_{xx} is the ultimate tensile strength of the UD composite with the off-axis angle θ [24]. The ultimate tensile strength at room temperature (RT), is also denoted as $\sigma_{ult}(\theta, \text{RT})$ for a given off-axis angle θ . In Chapter 4, the effect of temperature variations on the Tsai-Hill failure criterion will be discussed.

CHAPTER THREE

Fatigue Damage and Temperature Effect in FRP Composites

3.1 The Concept of Cumulative Fatigue Damage in FRP Composites

“Under cyclic tension-compression excursions, matrix cracks are formed as an initial stage of micro-damage process, which affects the residual strength and the life of a given laminate. Damage initiation in the form of microcracks is normally formed at a local micro-defect such as misaligned fibres, resin-rich regions or voids created during fabrication process. Once initiated, matrix cracks grow in a multiple mode and number within the matrix over the life cycles.” [9]

Damage accumulation continues as more cracks integrate until they encounter a fibre, leading to matrix-fibre phase. Damage progress at this stage may cause matrix-fibre debonding and more reduction in the stiffness of composite laminates. The later stage of damage development is typified by an increasing rate of progression of all damage modes resulting in catastrophic fibre failure. The progressive development of damage during fatigue life can be overviewed with the aid of Figure 3.1, which represents the development of damage during the fatigue life of unidirectional composite materials [9].

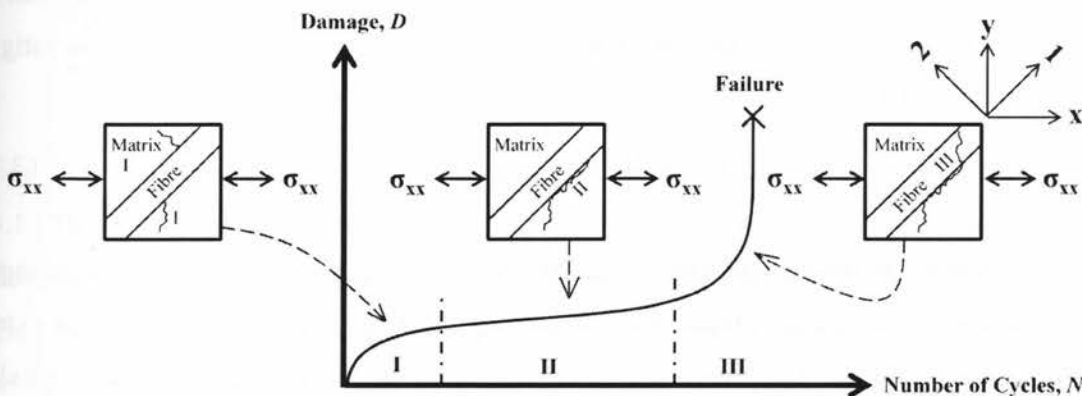


Figure 3.1: Three regions of cracking mechanism in unidirectional composites.

In region I, multiple crack initiations within the matrix are grouped together during the first 20% of the fatigue life. Region II commences as matrix cracks reach the vicinity of fibre. As the number of cycles increases, the crack grows along the fibre-matrix interface. This region is characterized with a larger life span and a lower slope of damage progress. In region III, with a shorter life span, fibre breakage occurs shortly after damage has been accumulated during regions I and II [9]. Generally, this mechanism is applicable for almost all kinds of laminated fibre-reinforced composites.

The long-term behaviour and damage mechanisms of fibre-reinforced polymer (FRP) composite materials have widely been researched by material engineers/scientists over the past thirty years. The fatigue behaviour of FRP composites is a complex process involving various changes in the microstructure of the material, before leading to different damage modes/types of failure. The damage process in FRP composites under fatigue loading is a combination of various damage modes, such as matrix cracking, fibre breakage, delaminations [18].

Any physically based damage model for a composite must use contributions from individual constituents as building blocks to determine the overall damage to the composite. The peculiarity of damage is that the three constituents of FRP composites (matrix, fibre-matrix interface, and fibre) do not fail simultaneously. This is explained by their differing mechanical properties [9]. Among different types of fatigue damage models, the concept of cumulative damage may be used as the most suitable approach to analyze and predict the fatigue behaviours of composite materials. It has been observed that the cumulative fatigue damage of composite materials can be measured in terms of stiffness reduction. Therefore, the quantitative evaluation of the fatigue damage can be shown as:

$$D = 1 - \frac{E_N}{E_0} \quad (3.1)$$

where D is cumulative fatigue damage, E_0 is the initial Young's modulus of the undamaged material, and E_N is the Young's modulus of the damaged material in cycle N . Thus, the extent of damage can be quantified by measuring the Young's modulus of the material. It is concluded from Equation (3.1) that D is between 0 and 1. When there is no damage, D equals 0, and when the material is fully damaged and divided into two parts, D becomes 1.

3.2 Fatigue Damage Models for FRP Composites

3.2.1 Ramakrishnan- Jayaraman Model

The mechanical behaviour of a composite material depends upon the response of its constituents, namely, the fibre, the matrix and their interface. Ramakrishnan and Jayaraman [8] have developed a stiffness-based damage model based on individual constituents as building blocks to determine the overall damage to the composite. In their model, a combination of logarithmic and linear decay functions of time (or cycles) was associated with the stiffness drops for the different damage processes. The total damage (D) as a function of the number of fatigue cycles (N) was described as:

$$D = \left\{ \frac{E_m V_m}{E_c} (1 - f^*) \frac{\ln(N+1)}{\ln(N_f)} \right\} + \left\{ \frac{E_m V_m}{E_c} f^* \left(\frac{N}{N_f} \right) \right\} + \left\{ \frac{E_f V_f}{E_c} \left(1 - \frac{\sigma_{appl}}{\sigma_{ult}} \right) \frac{\ln\left(1 - \frac{N}{N_f}\right)}{\ln\left(\frac{1}{N_f}\right)} \right\} \quad (3.2)$$

where N_f = fatigue life or number of cycles to failure,

E_m = Young's modulus of matrix,

E_f = Young's modulus of fibre,

V_m = volume fraction of matrix,

V_f = volume fraction of fibre,

E_c = Young's modulus of composite,

f^* = fibre/matrix interface strength parameter, ($0 \leq f^* \leq 1$),

σ_{appl} = applied tensile fatigue stress, and

σ_{ult} = ultimate tensile stress.

Equation (3.2) has three parts: a linear part between two logarithmic parts as shown in Figure 3.1. The first part is associated with the matrix degradation; the second part represents the fibre/matrix interface cracking; and, the third part is associated with the fibre failure/pull-out. This model has originally been developed for ceramic-matrix composites and is not applicable when composite specimens are subjected to loading with mean values. The Ramakrishnan-Jayaraman model is also used for on-axis loading conditions, restrictedly.

3.2.2 Varvani- Shirazi Model

The change of the fibres angle in respect to loading direction in a composite can change the strength of the composite. As the angle θ is increased from 0° to 90° , the stiffness of the composite is decreased. The effect of mean stress on fatigue damage is also crucially important. Varvani and Shirazi [9] have further developed the Ramakrishnan and Jayaraman fatigue damage model to include the effect of both fibre orientation and mean stress as:

$$D = \left\{ \left(1 - \frac{E_f V_f \cos \theta}{E_c} \right) (1 - f^*) \frac{\ln(N+1)}{\ln(nN_f)} \right\} + \left\{ \left(1 - \frac{E_f V_f \cos \theta}{E_c} \right) f^* \left(\frac{N}{nN_f} \right) \right\} + \left\{ \frac{E_f V_f \cos \theta}{E_c} \left(1 - \frac{\sigma_{max} (1-R)}{2\sigma_{ult}} \right) \frac{\ln \left(1 - \frac{N}{nN_f} \right)}{\ln \left(\frac{1}{nN_f} \right)} \right\} \quad (3.3)$$

where N_f = fatigue life or number of cycles to failure,

n = the assumed percentage of run-out or drop in stiffness,

θ = the angle between the fibre and the load direction,

E_m = Young's modulus of matrix,

E_f = Young's modulus of fibre,

V_m = volume fraction of matrix,

V_f = volume fraction of fibre,

E_c = Young's modulus of composite,

f^* = fibre/matrix interface strength parameter,

σ_{max} = maximum fatigue stress,

R = stress ratio ($\sigma_{min}/\sigma_{max}$),

σ_{ult} = ultimate tensile stress.

When the material under fatigue loading is fully damaged and divided into two parts, D becomes 1. It is always crucial to prevent failure due to fatigue cycles. Since damage in composites is characterized by three stages and a fast failure occurs in the last stage, researchers usually monitor cracking/damage to a certain percentage of drop in stiffness. Stiffness drop is a method

to control damage and prevent catastrophic failure. In Equation (3.3), the term n corresponds to the percentage of drop in stiffness recorded for a fatigue test. This mainly shows to what extent the stiffness drop versus fatigue cycles has been controlled/measured before final failure. For instance, by considering the degradation up to sixty percent of the real damage life (60%), term $n = (0.6)^{-1} = 1.67$. Then, the number of cycles considering term n is modified as nN_f .

3.3 Effect of Temperature on Fatigue Damage

Fatigue damage D in Equation (3.3) is developed as a function of the maximum applied stress σ_{max} , number of loading cycles N , load or stress ratio R , and material and structural properties, such as Young's modulus E , volume fraction V , and fibre orientation θ . Equation (3.3) can be further modified including the effect of temperature T , i.e.;

$$D = D(\sigma_{max}, N, R, E, V, \theta, T, \dots) \quad (3.4)$$

In Equation (3.3), three parameters including Young's modulus of the composite, E_c , composite ultimate tensile strength, σ_{ult} , and the fatigue life of composite, N_f , were found to be temperature-dependent. Substituting the temperature dependent parameters in Equation (3.3), the fatigue damage equation can be expressed as:

$$D = \left\{ \left(1 - \frac{E_f V_f \cos \theta}{E_c(T)} \right) (1 - f^*) \frac{\ln(N+1)}{\ln(nN_f(T))} \right\} + \left\{ \left(1 - \frac{E_f V_f \cos \theta}{E_c(T)} \right) f^* \left(\frac{N}{nN_f(T)} \right) \right\} + \left\{ \frac{E_f V_f \cos \theta}{E_c(T)} \left(1 - \frac{\sigma_{max}(1-R)}{2\sigma_{ult}(T)} \right) \frac{\ln\left(1 - \frac{N}{nN_f(T)}\right)}{\ln\left(\frac{1}{nN_f(T)}\right)} \right\} \quad (3.5)$$

To recognize the effect of temperature in Equation (3.5), the functions of $E_c(T)$, $\sigma_{ult}(T)$, and $N_f(T)$ are required to be expanded. The next chapter will discuss these functions in detail.

3.4 Effect of Temperature on Young's Modulus and Tensile Strength

Fibre-reinforced polymer composites fall into the class of viscoelastic materials. It means that

they respond to external forces in a manner intermediate between the behaviour of an elastic solid and a viscous liquid. An elastic solid has a definite shape and is strained by external forces instantaneously; once the forces are removed, it returns to its original state. By contrast, a viscous liquid has no definite shape and flows under the application of external forces irreversibly. The viscoelastic materials (e.g., FRP composites and polymers) can show both the properties of an elastic solid and a viscous liquid and all the intermediate properties depending on the temperature and strain rate. In the following sections, the effect of temperature on two of the materials properties, namely, the Young's modulus and tensile strength, will be discussed in detail.

3.4.1 Young's Modulus and Temperature

Generally, elastic moduli can be divided into: Young's modulus or moduli (E), shear moduli (G), and bulk moduli (B). The Young's moduli also include: tensile modulus (E_t), compressive modulus (E_c), and buckling modulus (E_b). The variation of temperature has a very significant effect on the elastic moduli and specially Young's moduli of fibre-reinforced polymer composites.

In composites, the polymeric matrix is profoundly influenced by temperature change. Figure 3.2 schematically illustrates the effect of temperature on the Young's modulus of a typical polymer. As it is seen, by increasing the temperature, the Young's modulus is decreased; however, the variation is not linear. Below a specific temperature called the glass transition temperature (T_g) of the polymer, the material is brittle or has a glassy state and shows an elastic behaviour. Above T_g , the polymer is ductile or has a rubbery state and behaves plastically. In the two cases, the variation of the Young's modulus with temperature is linear. However, between the two regions, there is a narrower region in which the material demonstrates a viscoelastic behaviour. Also, there is another narrow region above the rubbery state and around the melting point (T_m) of the polymer in which the material melts and flows as a liquid; in this case, the Young's modulus is the lowest and goes to zero. In both the flow and viscoelastic regions, the Young's modulus-temperature relation is not linear. Then, generally, the change of temperature divides the modulus-temperature diagram into the four regions of glassy, viscoelastic, rubbery, and flow. It

is also noteworthy that the same regions occur with the change of the time-scale or strain rate on the Young's modulus-time diagram, as discussed in Refs. 25 and 26. The effect of strain rate on the Young's modulus and other mechanical properties is not discussed in this research.

Figure 3.3 typically shows the effect of temperature on the Young's modulus of FRP composites with different lay-ups.

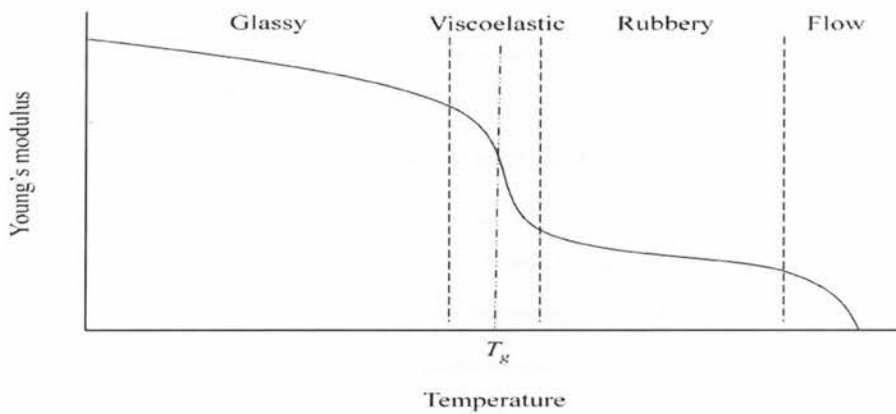


Figure 3.2: Temperature dependence of Young's modulus in a typical polymer.

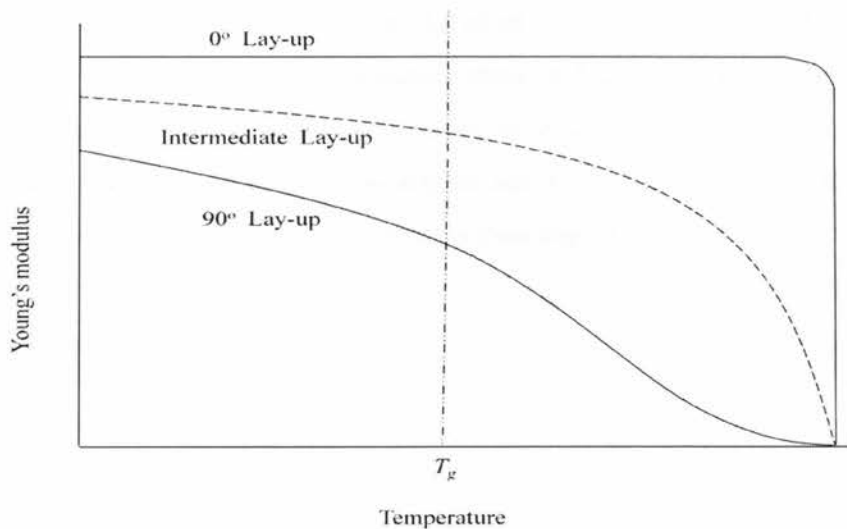


Figure 3.3: Temperature dependence of Young's modulus in typical laminated FRP composites.

As shown in Figure 3.3, due to the fibre dominance, the Young's modulus of the typical 0° lay-up remains unchanged with changing temperature by the matrix melting point. In other words, in an on-axis unidirectional laminated FRP composite, the great portion of the load is supported by the fibres. Since, the modulus of the fibres remains almost unchanged at temperatures below the melting point of the matrix, the modulus of the composite does not show considerable change. It is obvious that around the melting point, the matrix starts melting down. Therefore, the Young's modulus dramatically reduces. The 90° lay-up is matrix dominant at which the polymeric matrix severely degrades as the operating temperature increases. Any composite lay-up between 0 and 90 shows an intermediate response of modulus versus temperature change.

3.4.2 Ultimate Tensile Strength and Temperature

Riley *et al.* [27] defined the ultimate tensile strength (σ_{ult}) of a material as the maximum tensile stress (based on the original area) developed in the material before rupture. The definition, by replacing “tensile stress” with “compressive stress” or “shearing stress”, can also be used for the ultimate compressive strength or ultimate shear strength of the material, respectively. One of the main parameters which affects the ultimate strengths of FRP composites is temperature.

As Shen and Springer [28,29] declared, the effect of temperature on the ultimate tensile strength of laminated FRP composites is very similar to that on Young's modulus. It means that in Figure 3.3, by replacing “Young's modulus” with “Ultimate tensile strength” in the vertical axis, the same interpretations and conclusions can be rewritten for the ultimate tensile strength of the materials. In the next chapter, the formulations of the ultimate tensile strength and Young's modulus of the composites at different temperatures are presented.

CHAPTER FOUR

Temperature Dependent Fatigue Damage Model and its Parameters for FRP Composites

4.1 Mechanical Properties and Temperature Effect

The effect of temperature on the static and fatigue strengths of FRP composites and polymers has been studied by several researchers [25,26,30-32]. In these studies, either the Williams-Landel-Ferry (WLF) equation or an Arrhenius equation was employed to introduce a shift factor. The shift factor includes the effect of temperature on mechanical properties of polymers.

Based on the WLF equation, the shift factor $a(T)$ is expressed as:

$$\log a(T) = \frac{-C_1(T - T_0)}{C_2 + T + T_0} \quad (4.1)$$

where, T is temperature, T_0 is the reference temperature which has typically been supposed as T_g , and the constants C_1 and C_2 , originally thought to be universal constants, have been shown to vary rather slightly from polymer to polymer. A list of C_1 and C_2 for some polymers has been presented in Ref. 31. These constants have experimentally been measured at $T_0 = T_g$. The WLF equation is usually suitable for the temperature range of $T_g < T < T_g + 100$ K [32]. Therefore, it is normally used to predict the effect of temperature on the mechanical properties of the bulk polymers in the viscolastic and rubbery regions only (see Figure 3.2).

For polymers at temperatures above $T_g + 100$ K, the Arrhenius equation is used:

$$\log a(T) = \frac{\Delta H}{2.303G_C} \left(\frac{1}{T} - \frac{1}{T_0} \right) \quad (4.2)$$

where, G_C is the gas constant, 8.314 [J/K.mol], ΔH [J/mol] is the viscoelastic activation energy of the polymer, and T_0 is the reference temperature where $T_0 \neq T_g$. The Arrhenius equation is

usually applicable for rubber-like and liquid polymers.

The disadvantages of both WLF and Arrhenius equations are that: first, they are usually suitable for bulk polymers not composites; second, they are normally applicable in temperatures above the glass transition temperature of the polymer; and third, to obtain the constants in either equations, many experimental measurements are required. Therefore, to predict the mechanical properties of FRP laminates at various temperatures, it is essential to develop a model which is applicable to the composites, valid to a wider range of temperatures, and requires less experimental measurements.

4.2 The Proposed Temperature Dependant Relations for Monotonic Properties

In viscoelastic polymers, the shift factor, $a(T)$, is usually employed to predict the behaviour of the tensile viscosity $\eta(T)$ of a polymer at different temperatures as:

$$\eta(T) = a(T)\eta(T_0) \quad (4.3)$$

where, $\eta(T_0)$ is the tensile viscosity at the reference temperature, and $a(T)$ is the shift factor obtained by Equations (4.1) or (4.2). It is obvious that a relation such as Equation (4.3) can be written for any mechanical property of a material. Therefore, by rewriting Equation (4.3) for the ultimate tensile strength and the Young's modulus of laminated FRP composites, we have:

$$\sigma_{ult}(T) = a(T)\sigma_{ult}(T_0) \quad (4.4)$$

and

$$E(T) = a(T)E(T_0) \quad (4.5)$$

In the above two equations, $\sigma_{ult}(T)$ and $E(T)$ are, respectively, the ultimate tensile strength and the Young's modulus at an arbitrary temperature; $\sigma_{ult}(T_0)$ and $E(T_0)$ are the values of the physical parameters at the reference temperature.

Equations (4.3)–(4.5) are employed to identify material properties at any arbitrary temperature. These equations require both the reference temperature and the shift factor as known parameters. To formulate $\sigma_{ult}(T)$ and $E(T)$ in laminated FRP composites, a new relation for the shift factor,

$a(T)$, is proposed as:

$$a(T) = \left[1 - \frac{C}{\ln\left(1 - \frac{T_0}{T_m}\right)} \ln\left(\frac{\left(1 - \frac{T}{T_m}\right)}{\left(1 - \frac{T_0}{T_m}\right)}\right) \right] \quad (4.6)$$

where, T is temperature, T_0 denotes the reference temperature, and T_m is the polymer melting temperature of the composites, all in Kelvin. Constant C in Equation (4.6) is defined based on the mechanical property as:

$$C = \left(\frac{\sigma_{ult}(0)}{\sigma_{ult}(T_0)} - 1 \right) \quad (4.7)$$

and

$$C = \left(\frac{E(0)}{E(T_0)} - 1 \right) \quad (4.8)$$

In these equations, $\sigma_{ult}(0)$ and $E(0)$ are the ultimate tensile strength and the Young's modulus at absolute zero temperature ($0 \text{ K} = -273^\circ\text{C}$), respectively. Terms $\sigma_{ult}(T_0)$ and $E(T_0)$ correspond to values of the physical parameters at the reference temperature.

Based on Equations (4.6)–(4.8), Equations (4.4) and (4.5) can be rewritten as follows:

$$\sigma_{ult}(T) = \sigma_{ult}(T_0) \left[1 - \frac{\left(\frac{\sigma_{ult}(0)}{\sigma_{ult}(T_0)} - 1\right)}{\ln\left(1 - \frac{T_0}{T_m}\right)} \ln\left(\frac{\left(1 - \frac{T}{T_m}\right)}{\left(1 - \frac{T_0}{T_m}\right)}\right) \right] \quad (4.9)$$

and

$$E(T) = E(T_0) \left[1 - \frac{\left(\frac{E(0)}{E(T_0)} - 1\right)}{\ln\left(1 - \frac{T_0}{T_m}\right)} \ln\left(\frac{\left(1 - \frac{T}{T_m}\right)}{\left(1 - \frac{T_0}{T_m}\right)}\right) \right] \quad (4.10)$$

Equations (4.9) and (4.10) are the models which predict the amount of the ultimate tensile strength and the Young's modulus of laminated FRP composites at different temperatures.

4.3 The Elements of Proposed Temperature Dependent Relations

4.3.1 Temperature Variables

Before the evaluation, mentioning some points about the properties of Equations (4.9) and (4.10) is necessary. In the equations, temperature T is an arbitrary temperature. As T changes, the tensile strength and the Young's modulus change. Note that 0 K is theoretically the coldest temperature, and T_m is the polymer melting point of the composite. This addresses the temperature range of composites from the glassy state to the flow.

In Equations (4.9) and (4.10), the reference temperature T_0 has been taken as room temperature (RT = 20-27°C or 293-300 K). Therefore, in the evaluation of the model in the next chapter, T_0 is taken as RT. The values of σ_{ult} (RT) and E (RT) are readily obtained from rather less expensive tensile tests of composite materials. Taking T_0 below or above RT to measure $\sigma_{ult}(T_0)$ and $E(T_0)$ is also possible; however, it involves more costly and complicated tensile tests.

4.3.2 $E(T_0)$ and $\sigma_{ult}(T_0)$ and Temperature Effect on Tsai-Hill Relationship

The parameters of $E(T_0)$ and $\sigma_{ult}(T_0)$ are influenced by composite laminate lay-ups. For unidirectional laminates, the Tsai-Hill static failure criterion [22,23] can be employed to calculate $\sigma_{ult}(T_0)$ at $T_0 = \text{RT}$ as an alternative for measuring the parameter. The ultimate tensile strength predicted by this criterion for a unidirectional (off-axis) composite laminate at RT and plane stress condition is expressed as:

$$\sigma_{ult}(\theta, RT) = \frac{1}{\sqrt{\frac{\cos^4(\theta)}{X^2} - \frac{\cos^2(\theta)\sin^2(\theta)}{X^2} + \frac{\sin^4(\theta)}{Y^2} + \frac{\sin^2(\theta)\cos^2(\theta)}{S^2}}} \quad (4.11)$$

where, X and Y represent the ultimate tensile strength of the composite laminate along the fibre and transverse to the fibre directions, respectively, and S denotes the ultimate shear strength. The angle between the fibre and load direction is denoted as θ . The values of axial and transverse tensile strengths and shear strength of an on-axis ($\theta = 0^\circ$) laminate are determined and used as inputs of Equation (4.11) to calculate the ultimate tensile strength of off-axis (θ°) laminates.

Equation (4.11) can be substituted into Equation (4.9) to represent a general form of Tsai-Hill static failure criterion in which the effect of temperature has been considered.

4.3.3 Constant C in Shift Factor Relation

The constant C in Equation (4.6) corresponds to the sensitivity of material or mechanical property to temperature variation. The constant defined in Equations (4.7) and (4.8) is a function of $\sigma_{ult}(0)$ and $\sigma_{ult}(T_0)$ or $E(0)$ and $E(T_0)$. In both cases, by knowing the amount of the mechanical properties at 0 K and T_0 (T_0 is normally assumed as room temperature), the corresponding constant is achieved.

The measurement of $\sigma_{ult}(0)$ or $E(0)$ at absolute zero (the coldest temperature) is theoretically possible. The temperatures of liquid oxygen, nitrogen, hydrogen, and helium are about 90 K, 77 K, 22 K, and 4 K, respectively. Using advanced cryogenic equipment, temperatures as low as 4 K (using liquid helium) are achieved to obtain $\sigma_{ult}(4)$ and $E(4)$, which are close enough to values of $\sigma_{ult}(0)$ and $E(0)$.

In Equations (4.7) and (4.8), where $\sigma_{ult}(0) \geq \sigma_{ult}(RT)$ and $E(0) \geq E(RT)$, the constant C varies between 0 and 1 for almost all laminated FRP composites. In these cases, Equations (4.9) and (4.10) are plotted as the diagram presented in Figure 4.1. This diagram shows a decreasing trend with increasing temperature. When $\sigma_{ult}(0) = \sigma_{ult}(RT)$ or $E(0) = E(RT)$, C becomes 0. This case represents a very strong 0° lay-up. For other composite lay-ups and laminates, as matrix dominance increases from 0° lay-up to 90° lay-up, $\sigma_{ult}(0)$ is greater than $\sigma_{ult}(RT)$ and $E(0)$ is greater than $E(RT)$. When $\sigma_{ult}(0) = 2\sigma_{ult}(RT)$ or $E(0) = 2E(RT)$, C becomes 1.

From Figures 5.1–5.13, it has also been concluded that, for most of the situations, the amount of C for the ultimate tensile strength is normally between 0.2 and 0.4, and the constant C for the Young's modulus is usually between 0.1 and 0.2. Therefore, on average, C can be considered 0.3 and 0.15 for σ_{ult} and E , respectively. Based on these figures, Equations (4.9) and (4.10) will be evaluated in Chapter 5.

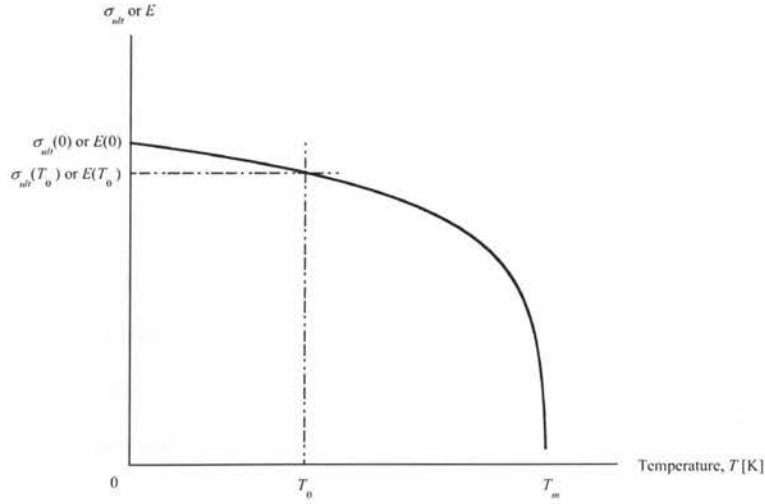


Figure 4.1: A typical curve of $\sigma_{ult} - T$ or $E - T$ plotted with Equations (4.9) or (4.10) in the defined cases.

4.4 Fatigue Strength and Temperature

When a composite material is subjected to cyclic stresses, fatigue damage is cumulated over fatigue cycles, and when the damage becomes 100%, fatigue failure takes place. The relation between the cyclic stress, σ , and the number of cycles to failure, N_f , is mathematically defined as:

$$\sigma = A(N_f)^m \quad (4.12)$$

Equation (4.12) is known as the power-law stress-life relation, and the $\sigma - N_f$ curve based on the equation is generally the so-called S-N curve. By plotting σ versus the logarithm of N_f , a curve very similar to a line is obtained in which coefficient A is the y-intercept at $N = 1$ cycle, and exponent m , which has a negative value, represents the slope of the curve. The σ is normally considered as one of the following stresses : maximum stress, σ_{max} , minimum stress, σ_{min} , mean stress, $\sigma_{mean} = (\sigma_{max} + \sigma_{min})/2$, stress range, $\Delta\sigma = \sigma_{max} - \sigma_{min}$, or stress amplitude, $\sigma_a = \Delta\sigma/2$. In this study, it is considered as the maximum stress. Hence, Equation (4.12) is rewritten as:

$$\sigma_{max} = A(N_f)^m \quad (4.13)$$

In this thesis, the load history is in sinusoidal form. If a sinusoidal load is applied to a specimen, and the specimen fails in a quarter of a cycle, it means that the amount of stress has been equal to

the ultimate strength. In the case of tension-tension or tension-compression loading, constant A equals the ultimate tensile strength. Equation (4.13) then is rewritten as:

$$\sigma_{max} = \sigma_{ult} (4N_f)^m \quad (4.14)$$

Equation (4.13) can also be expressed as:

$$\sigma_{max} = \sigma_{ult} (2N_f)^m \quad (4.15)$$

In fact, Equation (4.15) specifies that if the specimen failed in half a cycle or in a *reversal*, the maximum applied stress would be equal to the ultimate tensile strength.

However, between the two equations, (4.14) and (4.15), using Equation (4.14) is recommended because it is more precise. This equation expresses the way fatigue properties of the material can be related to its static property. Using the equation, by knowing the intercept A and the slope m of a S-log N curve for a material, the ultimate tensile strength, σ_{ult} , of the material will be calculated.

4.4.1 Temperature Effect on Intercept (A)

By comparing Equation (4.13) with Equation (4.14), it is concluded that the intercept A can be expressed as:

$$A = \sigma_{ult} (4^m) \quad (4.16)$$

In the previous part, the effect of temperature on the ultimate tensile strength of laminated FRP composites was studied. According to Equation (4.16), A is a function of σ_{ult} . It means that the variation of A in regards to temperature is similar to that of σ_{ult} . Therefore, the effect of temperature on A can be characterized in the same way as σ_{ult} . Analogous to Equation (4.9), the effect of temperature on A can be formulated as:

$$A(T) = A(T_0) \left[1 - \frac{\left(\frac{A(0)}{A(T_0)} - 1\right)}{\ln\left(1 - \frac{T_0}{T_m}\right)} \ln\left(\frac{\left(1 - \frac{T}{T_m}\right)}{\left(1 - \frac{T_0}{T_m}\right)}\right) \right] \quad (4.17)$$

where $A(T)$ is the intercept at an arbitrary temperature, $A(T_0)$ is the amount of intercept at the reference temperature normally at room temperature, and $A(0)$ represents the amount of intercept at 0 K. Using Equation (4.17), the intercept is achieved at any arbitrary temperature. Figure (4.2) presents the response of intercept A as the operating temperature increases.

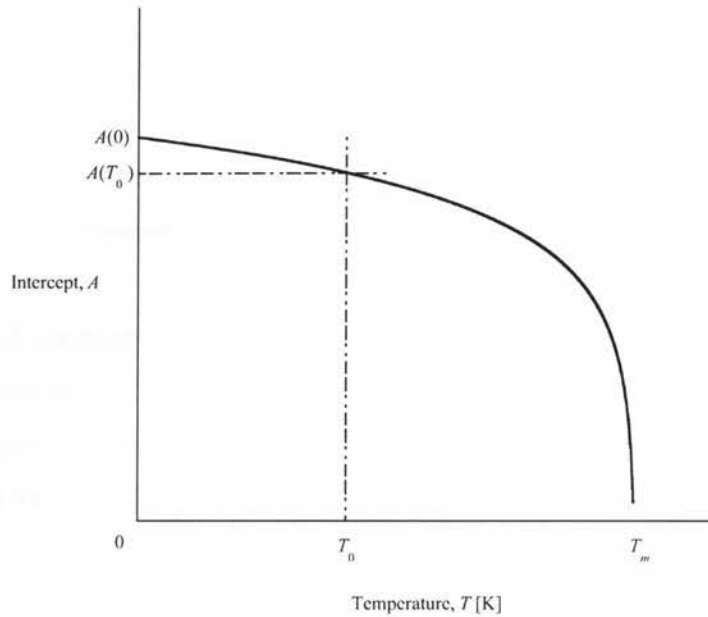


Figure 4.2: Illustration of intercept-temperature curve generated using Equation (4.17).

4.4.2 Temperature Effect on Slope (m)

The exponent m in Equation (4.13) corresponds to the slope of the S-log N curve. Since by increasing and decreasing stress, the life is respectively decreased and increased, m has a negative value. Therefore, the bigger the absolute value of m , the more the fatigue strength and vice versa. In contrast with intercept A , which has a static nature, m has a fatigue nature and is obtained by doing at least three fatigue tests. It is worthy to note that to increase the precision of m , the number of fatigue tests should be increased to an even 30, containing a full range of fatigue lives, from 1 cycle to 10^6 or 10^7 cycles. Normally, the absolute value of the m achieved by the 30 tests is less than that of the 3-test m . This is mainly due to the high scatter and statistical nature of fatigue tests. Therefore, the higher number of fatigue tests done on a specimen, the more optimum slope is obtained for its S-log N curve.

The response of intercept A with temperature on laminated FRP composites shows a decreasing trend almost the same as what was presented in Figure 4.2, based on Equation (4.17). However, the variation of m with temperature is more complex. Exponent m shows variations with stress ratio and the range of operating temperature. To formulate m as a function of temperature, several sets of experimental S-N fatigue data (listed in Appendix B) at various operating temperatures were studied, and Equation (4.18) resulted:

$$m(T) = m(T_0) \left[\frac{\ln \left(1 - \frac{T}{T_m} \right)}{\ln \left(1 - \frac{T_0}{T_m} \right)} \right] \quad (4.18)$$

In Equation (4.18), $m(T)$ represents slope (m) as a function of temperature (T), and $m(T_0)$ denotes the amount of slope at reference temperature T_0 ($= RT$). In this equation, the whole term in the square brackets represents the shifting factor for the slope m . It is noteworthy to specify that the fundamentals of Equation (4.18) are analogous to Equations (4.17), (4.10), and (4.9). Figure 4.3 depicts the response of m versus temperature.

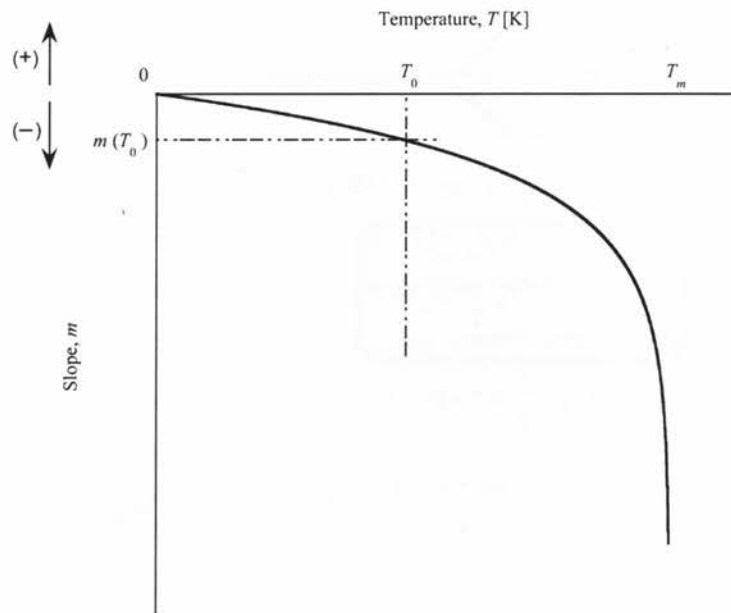


Figure 4.3: Typical illustration of slope-temperature curve plotted using Equation (4.18).

Similar to Figure 4.2, Figure 4.3 has been plotted in the temperature range of 0 K to around T_m . As it is seen from Figure 4.3, the absolute value of slope m is increased by increasing temperature. This increasing trend, which is almost similar to the decreasing trend of intercept with temperature, signifies the fact that by increasing temperature the fatigue strength decreases.

As it was discussed earlier, the S-N relation is defined as Equation (4.13). Inserting the temperature dependent parameters of A and m in this equation results in:

$$\sigma_{max} = A(T)(N_f(T))^{m(T)} \quad (4.19)$$

Substituting Equations (4.17) and (4.18) into Equation (4.19), the full description of the temperature dependent S-N relation is expressed as:

$$\sigma_{max} = A(T_0) \left[1 - \frac{\left(\frac{A(0)}{A(T_0)} - 1\right)}{\ln\left(1 - \frac{T_0}{T_m}\right)} \ln\left(\frac{\left(1 - \frac{T}{T_m}\right)}{\left(1 - \frac{T_0}{T_m}\right)}\right) \right] (N_f(T))^{m(T_0) \left[\frac{\ln\left(1 - \frac{T}{T_m}\right)}{\ln\left(1 - \frac{T_0}{T_m}\right)} \right]} \quad (4.20)$$

4.5 Inclusion of Temperature Dependent Parameters in Fatigue Damage Model

To implement the effect of temperature in fatigue damage Equation (3.5), the temperature dependant parameters of $\sigma_{ult}(T)$ and $E(T)$ or $E_c(T)$ have been formulated. The proposed relationships for the parameters have been developed in Equations (4.9) and (4.10). Fatigue life data N_f obtained at temperature T was used as an input of the damage equation. Therefore, considering the parameters, fatigue damage Equation (3.5) is given as:

$$D = \left\{ \left(1 - \frac{F}{E_c(T)} \right) (1 - f^*) \frac{\ln(N+1)}{\ln(nN_f)} \right\} + \left\{ \left(1 - \frac{F}{E_c(T)} \right) f^* \left(\frac{N}{nN_f} \right) \right\} + \left\{ \frac{F}{E_c(T)} \left(1 - \frac{\sigma_{max}(1-R)}{2\sigma_{ult}(T)} \right) \frac{\ln\left(1 - \frac{N}{nN_f}\right)}{\ln\left(\frac{1}{nN_f}\right)} \right\} \quad (4.21)$$

Term F in Equation (4.21) varies based on composite laminate lay-up. For unidirectional

composites, term F extracted from the rule of mixtures becomes $E_f V_f \cos(\theta)$. For orthogonal woven composites, the rule of mixtures results in $F = K_f E_f V_f$. Note that $V_f^* = K_f V_f$ corresponds to the volume fraction of fibres which are aligned in the loading direction.

4.5.1 Algorithm/Flowchart of Fatigue Damage Analysis for FRP Composites

Figure 4.4 represents the procedure of fatigue damage analysis of the described woven composites based on the proposed damage method in this study.

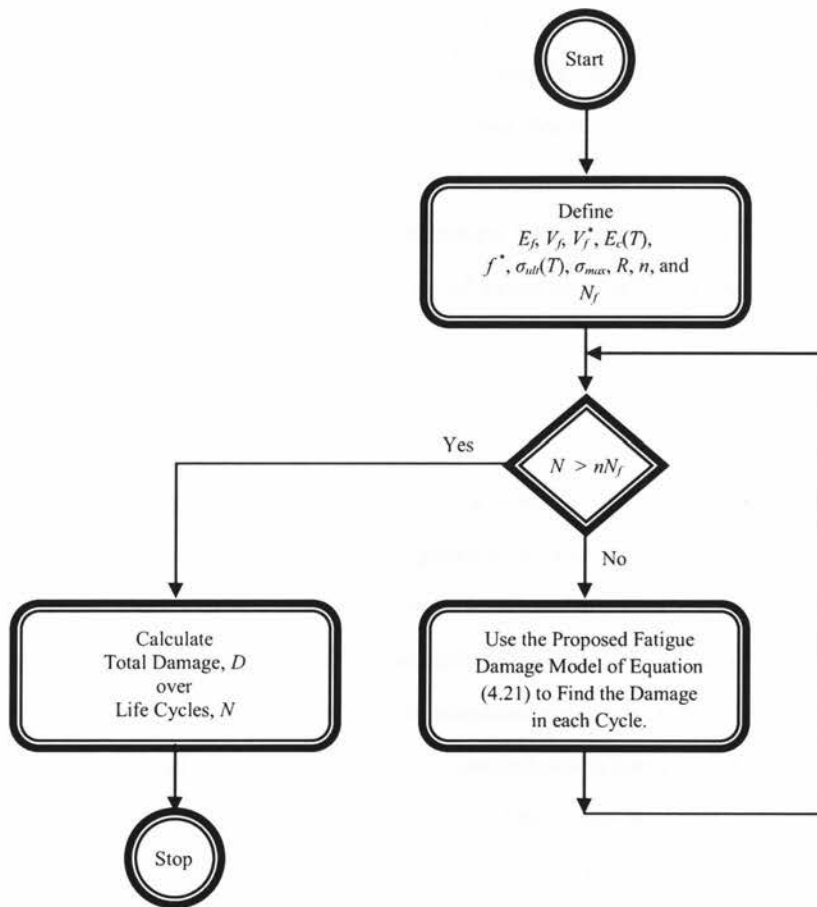


Figure 4.4: Flowchart of generalized material property degradation technique

The developed fatigue damage analysis method includes damage in three regions of the matrix, matrix-fibre interface and fibre, and reflects the cracking mechanism within the three regions from early region of growth to final failure. This flowchart illustrates the procedure of damage

analysis in the following steps:

- i. Define input parameters of E_f , V_f , V_f^* , $E_c(T)$, f^* , $\sigma_{ult}(T)$, σ_{max} , R , n , and N_f .
- ii. For cycles smaller than fatigue life, calculate the values of damage cycle-by-cycle.
- iii. Calculate the total damage over fatigue life cycles.

CHAPTER FIVE

Evaluation of the Temperature Dependent Analysis and Results

5.1 Evaluation of the Temperature Dependent Monotonic Properties Model

Experimental data extracted from the literature [28,29,33,34] have been used to evaluate the formulations proposed for the ultimate tensile strength and Young's modulus. The tested materials, the type of plies and laminates, the reported fibre volume fraction of some specimens, and also the amount of the mechanical properties at room temperature have been listed in Tables A-1 and A-3. The extracted data from the literature have been tabulated in Appendix B. The following section presents two extensive sources of experimental data used in this thesis.

5.1.1 Jen *et al.* Data

Jen *et al.* [34] tensile tested samples made of graphite/PEEK (AS-4/PEEK) prepregs with different lay-ups of cross-ply $[0/90]_{4S}$ and quasi-isotropic $[0/+45/90/-45]_{2S}$ laminates. After curing, the laminates were cooled down at room temperature (RT) and taken out from the hot press. A cutting machine with diamond blade and water cooling was used to cut the laminates into $L = 240$ mm, $W = 25.4$ mm, and $t = 2$ mm coupons, according to ASTM D3039-93. Copper plate was considered as end tabs by NP-50 two-component adhesive. The fibre volume fraction of the specimens was reported to be about 61%. The tension tests on the specimens were performed at RT (25°C), 50°C, 75°C, 100°C, 125°C, 150°C, and 175°C.

5.1.2 Shen and Springer Data

Shen and Springer [28,29] have measured ultimate tensile strength and buckling modulus of a special kind of graphit/epoxy specimens called Thornal 300/Fiberite 1034 at different temperatures. The size of the specimens in the tension test was reported as $L = 101$ mm, $W =$

12.7 mm, and $t = 0.9$ mm, and the size in the buckling tests was reported as $L = 36$ -318 mm, $W = 4.76$ mm, and $t = 0.9$ mm. Shen and Springer have also evaluated the ultimate tensile strength and Young's modulus variations with temperature using different sets of data available in the literature. The summary of the test data is discussed as follows: Thornel 300/Narmco 5208 was tensile tested at a temperature range between 300-450 K, reported by Hofer *et al.* [35] and Husman [39]. Hertz [36] performed monotonic tests on HT-S/(8183/137-NDA-BF₃:MEA) at various temperatures of 200-450 K. The experimental measurements of Browning *et al.* [37] on the influence of temperature on σ_{ult} for Hercules AS-5/3501 were ranged from 300 K to 425 K. Further experiments were conducted to obtain the effect of temperature on σ_{ult} for boron/Narmco 5505 by Kaminski [38]. In addition to σ_{ult} experiments, Hofer *et al.* [35] conducted a new sets of tensile tests to evaluate E with temperature change between 300 K to 450 K.

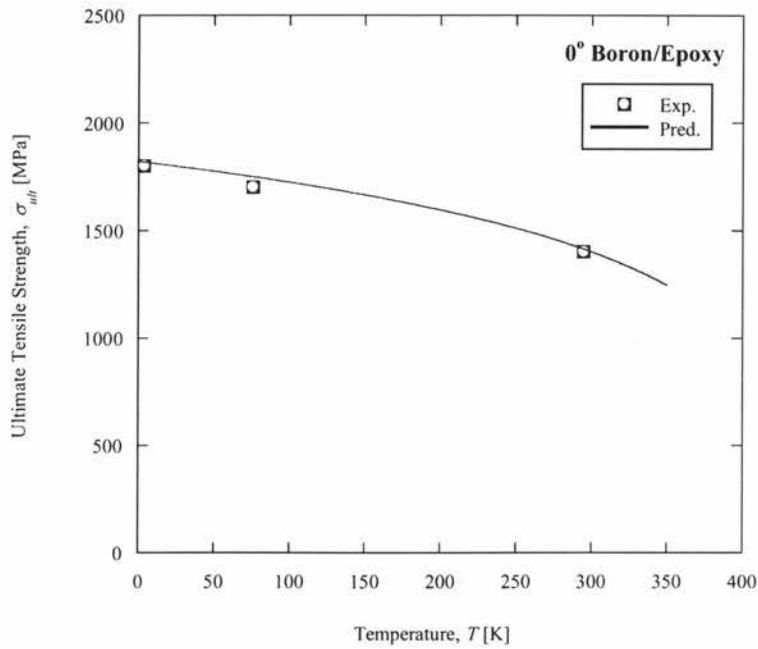
5.1.3 Calculated $\sigma_{ult}(T)$ and $E(T)$ Results

To calculate $\sigma_{ult}(T)$ and $E(T)$ using Equations (4.9) and (4.10) the following parameters are required:

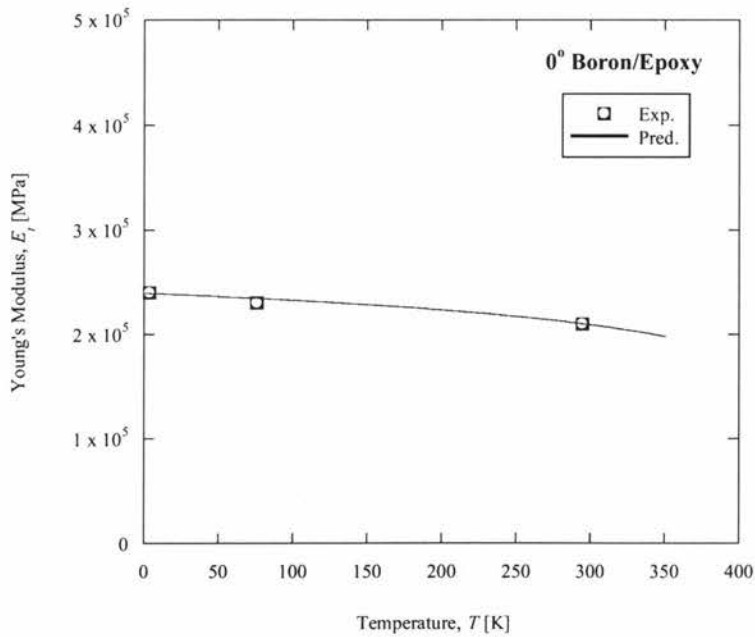
- i. The amount of σ_{ult} and E at room temperature, $\sigma_{ult}(T_0 = RT)$ and $E(T_0 = RT)$.
- ii. The amount of σ_{ult} and E at 0 K, $\sigma_{ult}(0)$ and $E(0)$.
- iii. Room temperature, RT, and the polymer melting point of the tested FRP laminate, T_m .

To evaluate Equations (4.9) and (4.10), over ten different composite materials [28,29,33,34] were examined. All the parameters required to calculate the proposed relations were taken from the literature and listed in Tables A-1–A-4. The calculated mechanical properties at various operating temperatures were compared with the experimental values in Figures 5.1–5.13. The figures show a good correlation between the experimental data and the predicted values.

In Figures 5.1–5.12, the ultimate tensile strength shows a steeper decay than Young's modulus as operating temperature increases. These figures verify that the Young's modulus of on-axis composites is less sensitive to temperature change. For composites with the lay-up of 90°, the degradation of the Young's modulus becomes more pronounced as the temperature increases (see Figures 5.8 to 5.10 and 5.13).

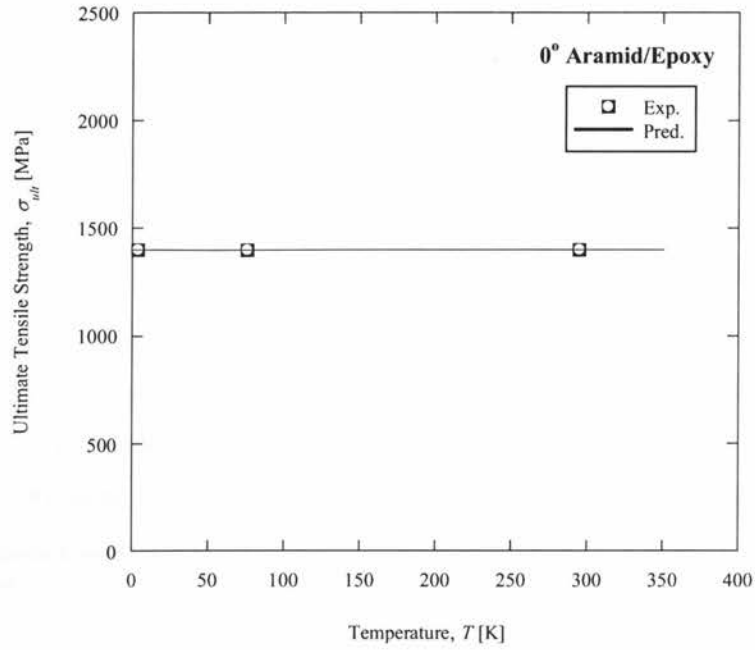


(a)

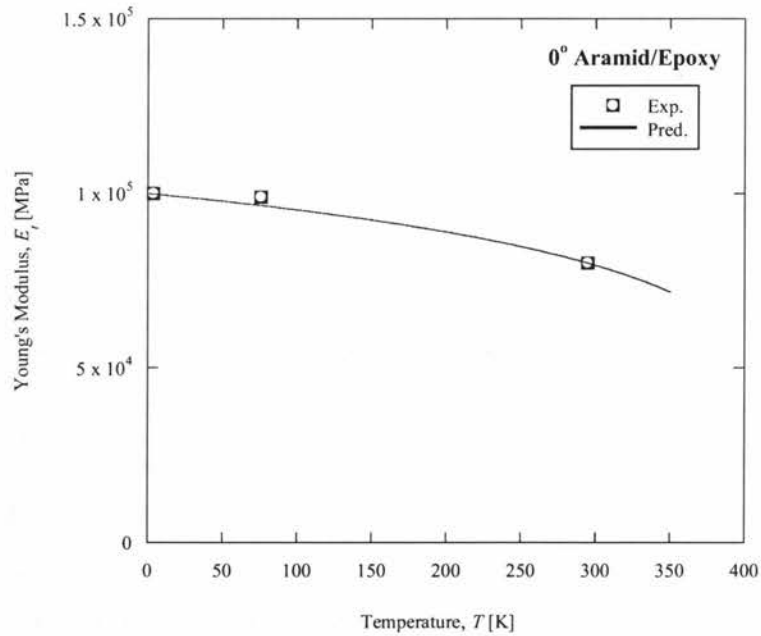


(b)

Figure 5.1: (a) Ultimate tensile strength and (b) tensile modulus of 0° boron/epoxy as a function of temperature. Data of Ref. 33 modeled by Equations (4.9) and (4.10), respectively.

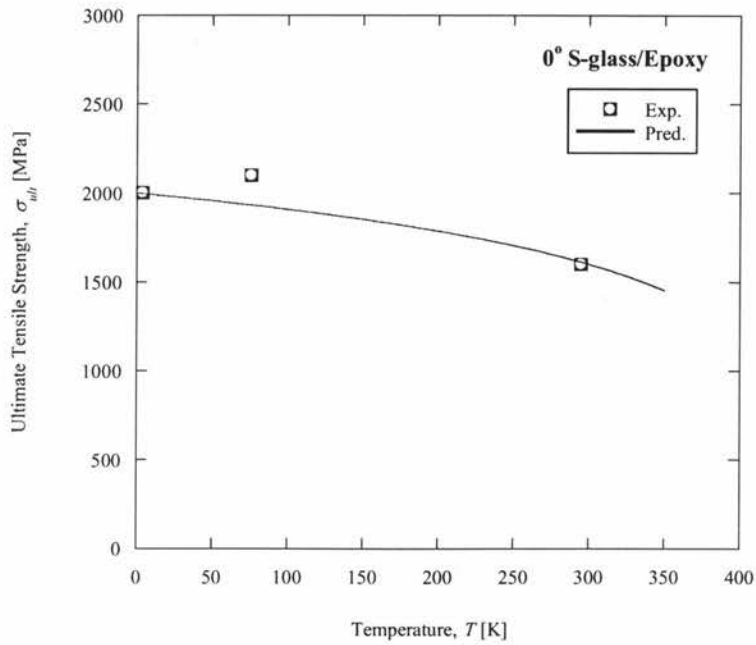


(a)

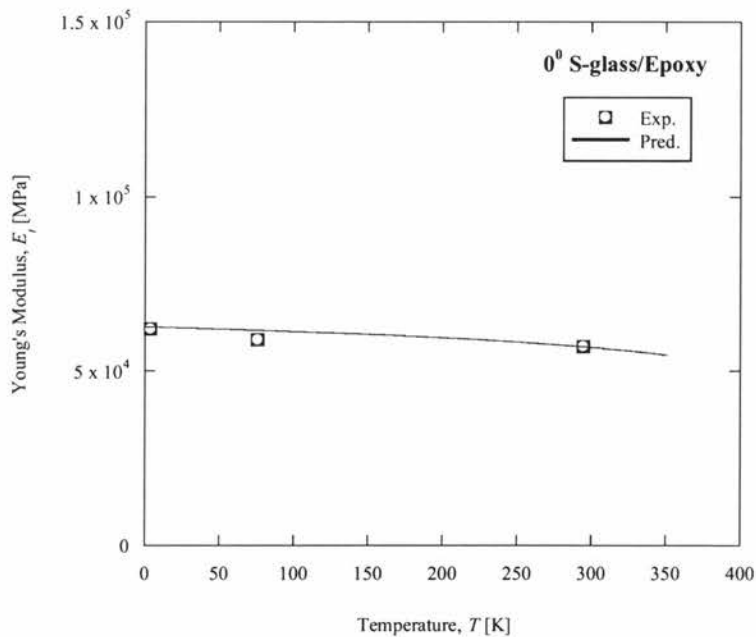


(b)

Figure 5.2: (a) Ultimate tensile strength and (b) tensile modulus of 0° aramid/epoxy as a function of temperature. Data of Ref. 33 modeled by Equations (4.9) and (4.10), respectively.

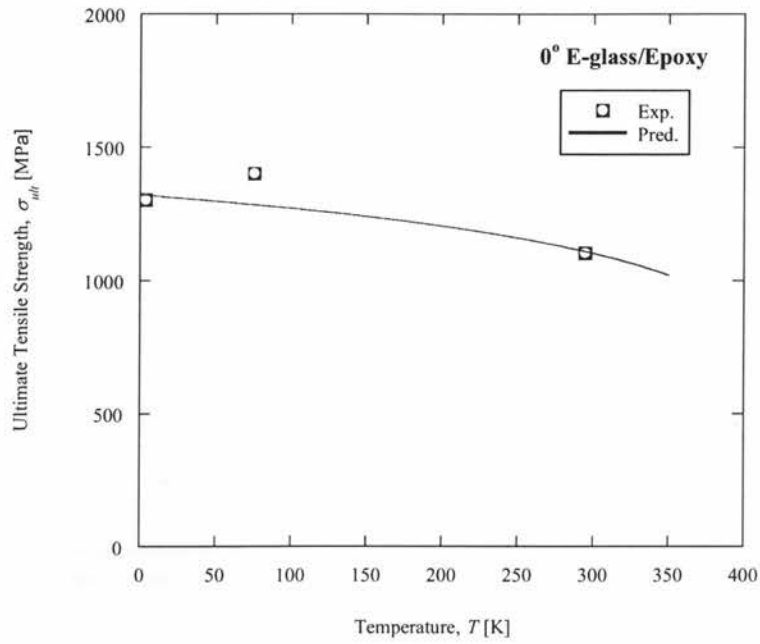


(a)

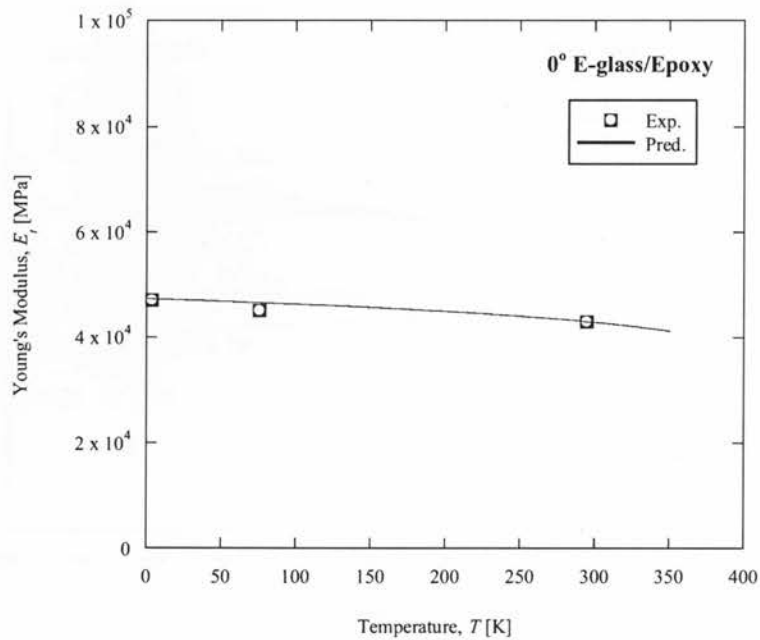


(b)

Figure 5.3: (a) Ultimate tensile strength and (b) tensile modulus of 0° S-glass/epoxy as a function of temperature. Data of Ref. 33 modeled by Equations (4.9) and (4.10), respectively.



(a)



(b)

Figure 5.4: (a) Ultimate tensile strength and (b) tensile modulus of 0° E-glass/epoxy as a function of temperature. Data of Ref. 33 modeled by Equations (4.9) and (4.10), respectively.

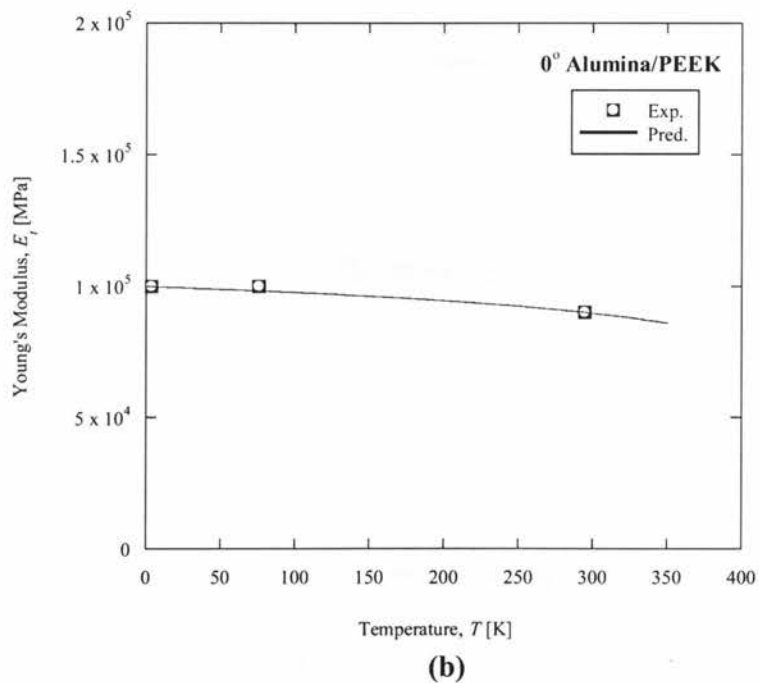
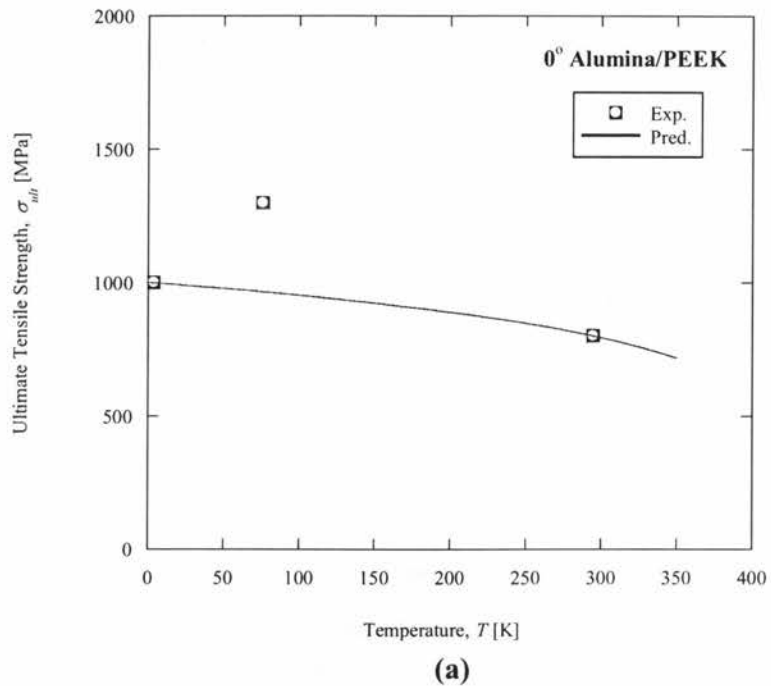


Figure 5.5: (a) Ultimate tensile strength and (b) tensile modulus of 0° alumina/PEEK as a function of temperature. Data of Ref. 33 modeled by Equations (4.9) and (4.10), respectively.

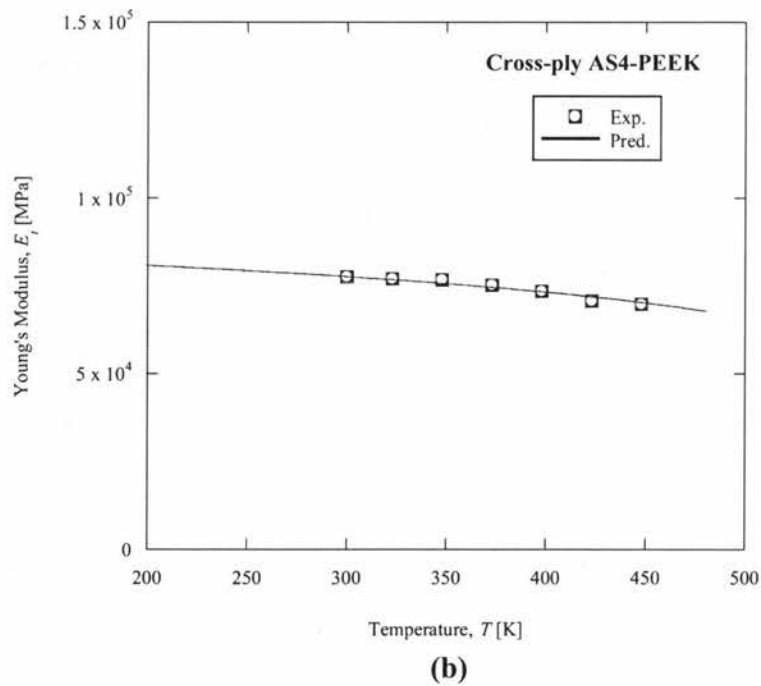
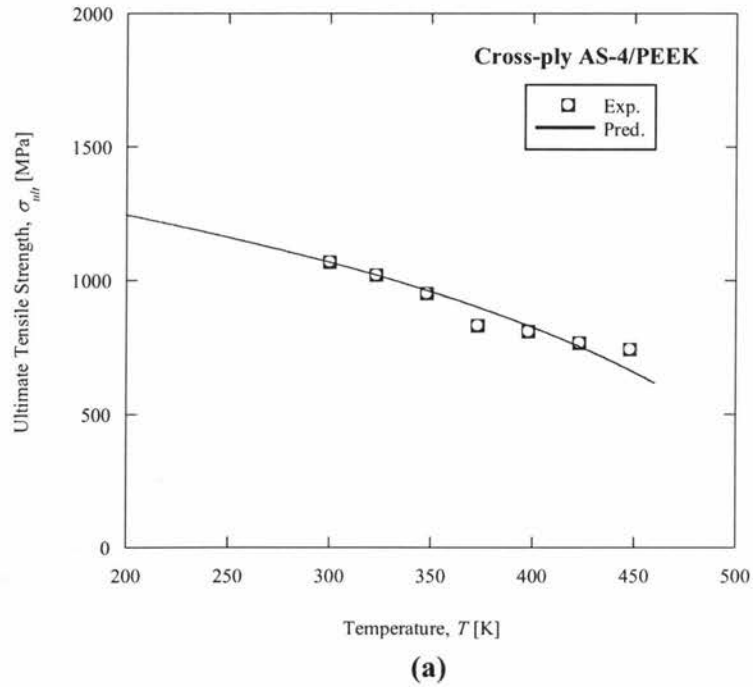
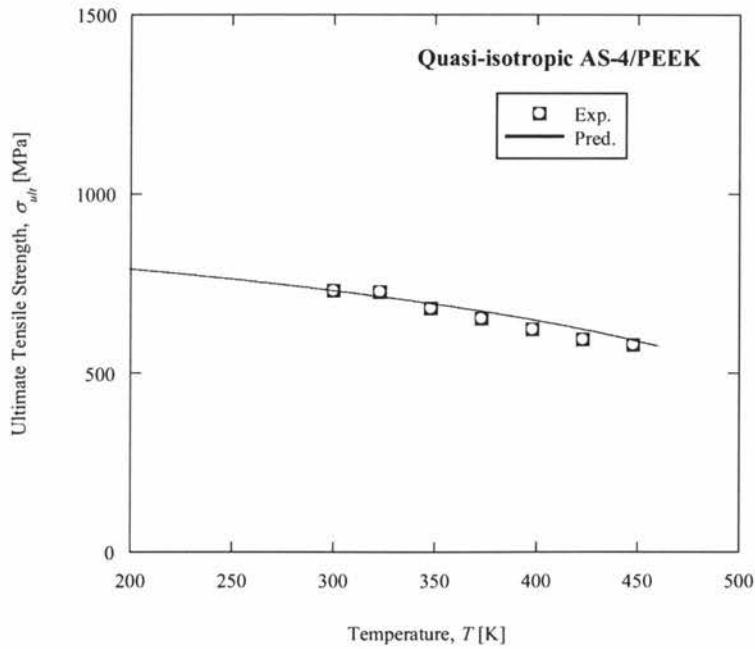
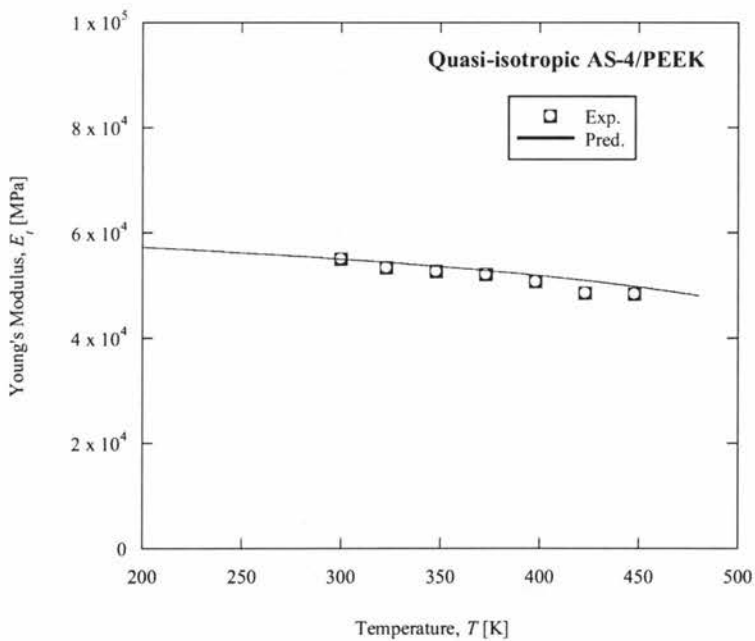


Figure 5.6: (a) Ultimate tensile strength and (b) tensile modulus of $[0/90]_{4S}$ AS-4/PEEK as a function of temperature. Data of Ref. 34 modeled by Equations (4.9) and (4.10), respectively.



(a)



(b)

Figure 5.7: (a) Ultimate tensile strength and (b) tensile modulus of $[0/+45/90/-45]_{2S}$ AS-4/PEEK as a function of temperature. Data of Ref. 34 modeled by Equations (4.9) and (4.10), respectively.

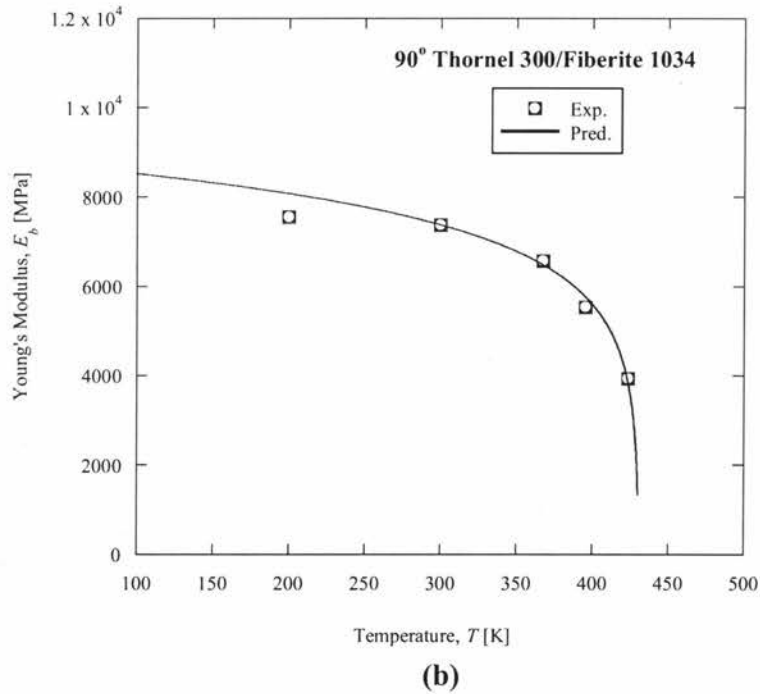
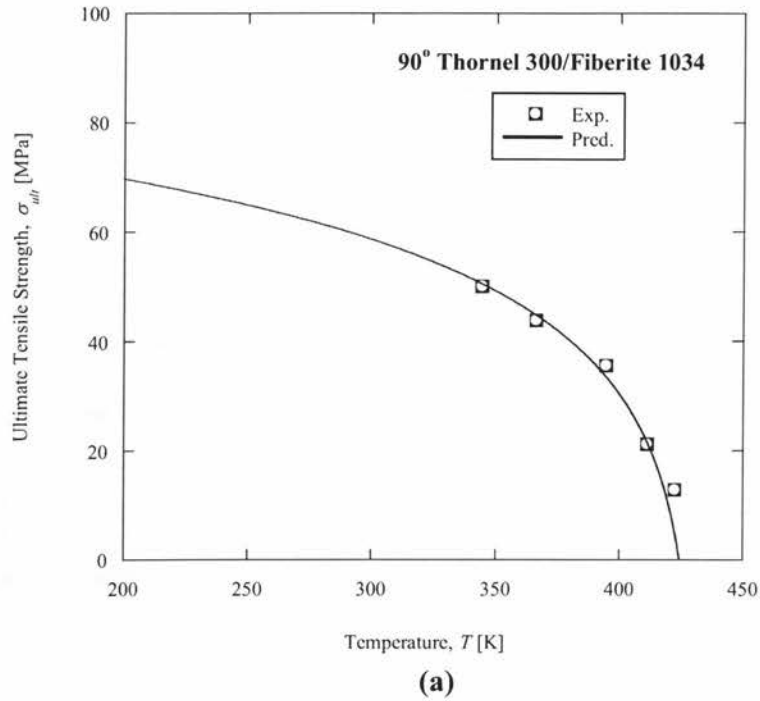


Figure 5.8: (a) Ultimate tensile strength and (b) buckling modulus of 90° Thornel 300/Fiberite 1034 as a function of temperature. Data of Refs. 28 and 29 modeled by Equations (4.9) and (4.10), respectively.

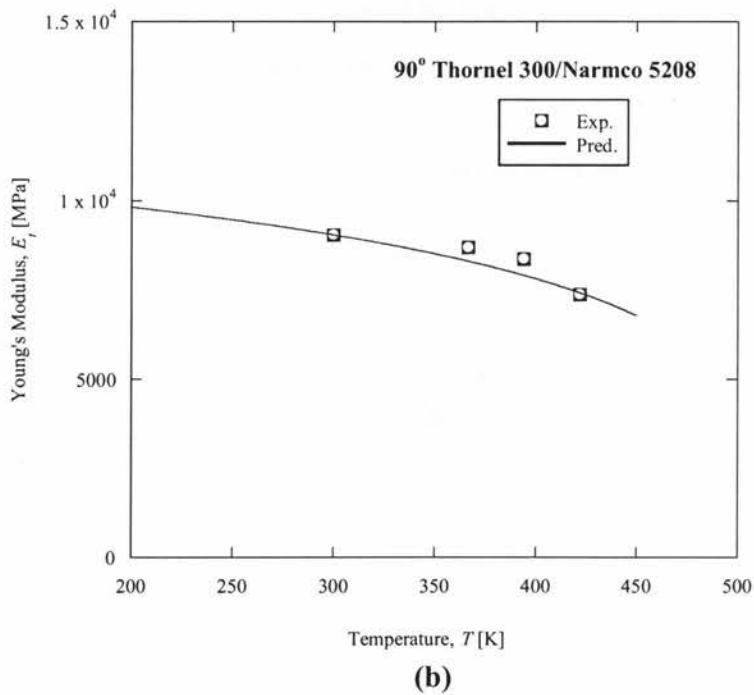
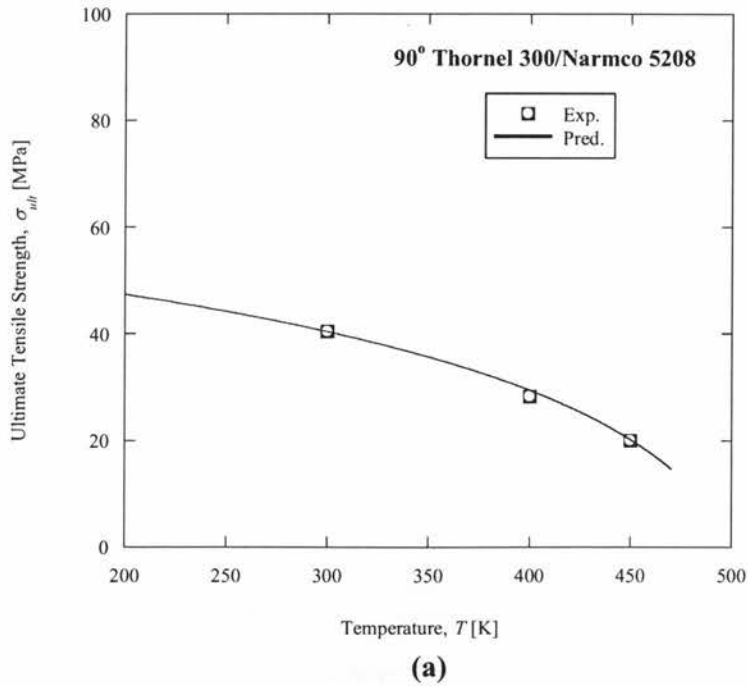
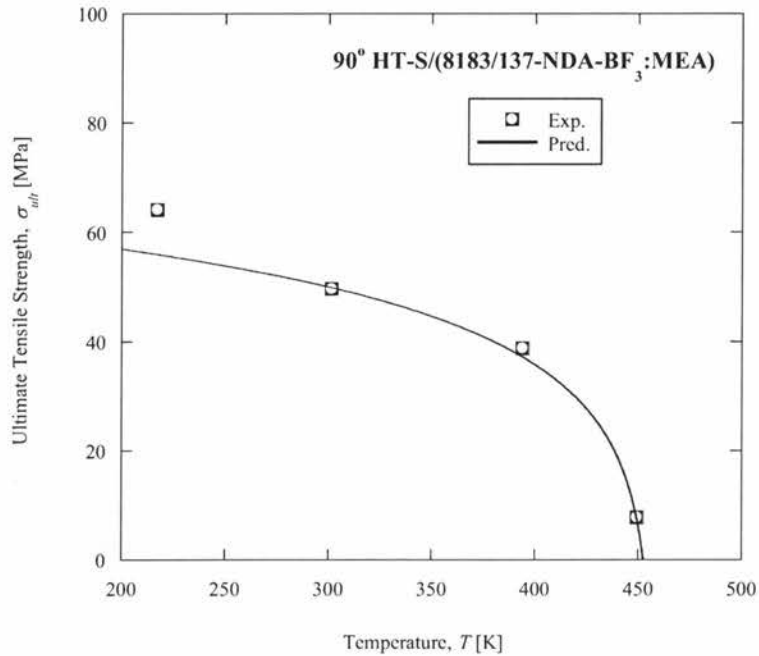
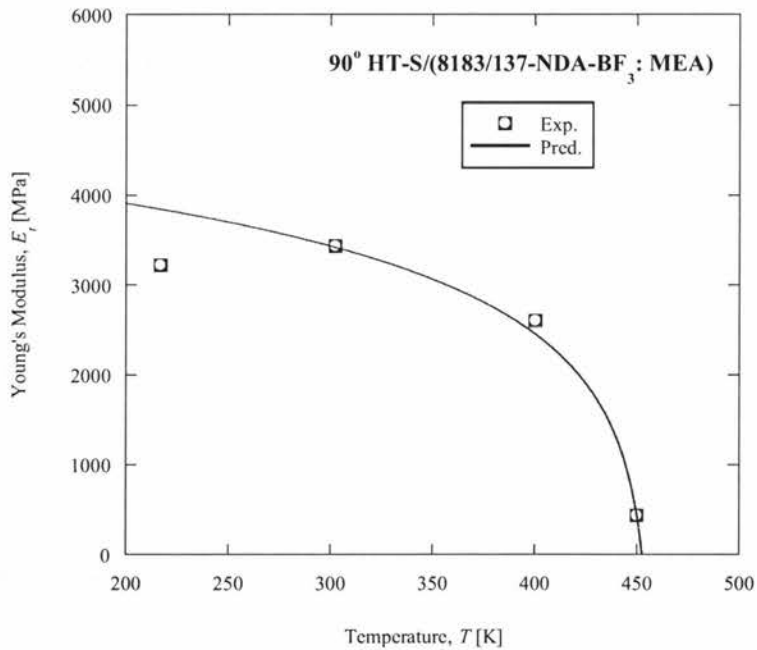


Figure 5.9: (a) Ultimate tensile strength and (b) tensile modulus of 90° Thornel 300/Narmco 5208 as a function of temperature. Data of Refs. 28 and 29 modeled by Equations (4.9) and (4.10), respectively.



(a)



(b)

Figure 5.10: (a) Ultimate tensile strength and (b) tensile modulus of 90° HT-S/(8183/137-NDA-BF₃:MEA) as a function of temperature. Data of Refs. 28 and 29 modeled by Equations (4.9) and (4.10), respectively.

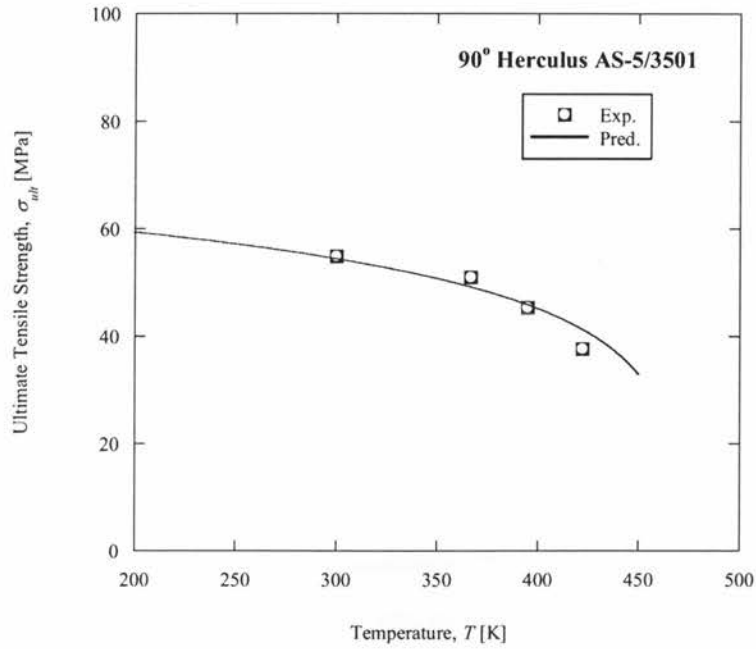


Figure 5.11: (a) Ultimate tensile strength of 90° Hercules AS-5/3501 as a function of temperature. Data of Ref. 28 modeled by Equation (4.9).

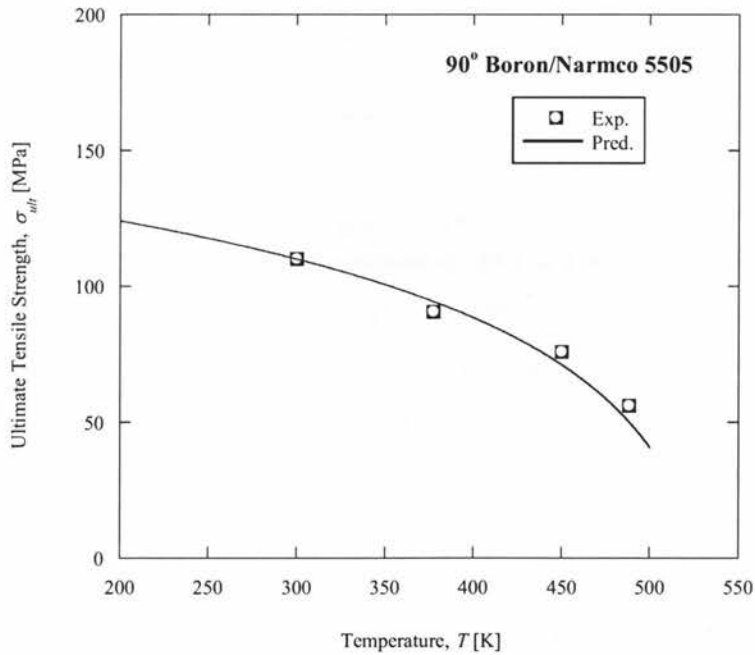


Figure 5.12: (a) Ultimate tensile strength of 90° boron/Narmco 5505 as a function of temperature. Data of Ref. 28 modeled by Equation (4.9).

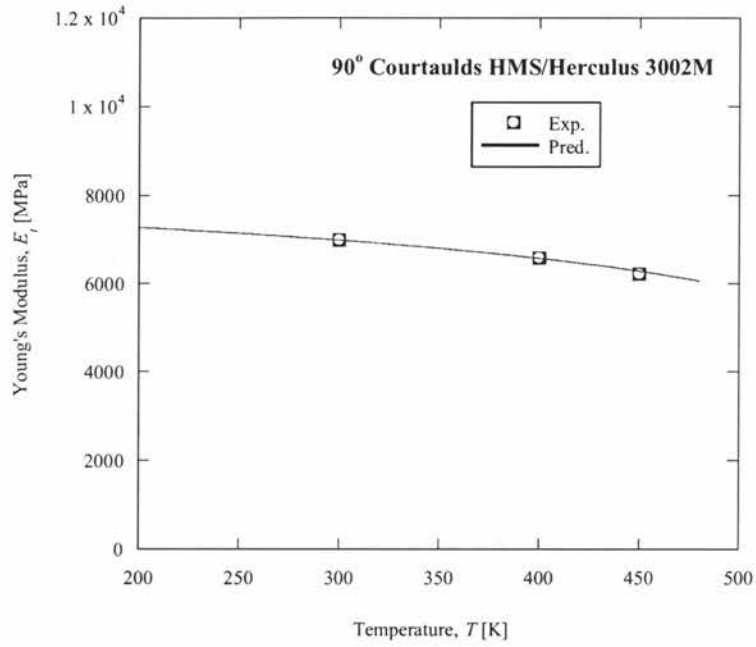


Figure 5.13: (a) Tensile modulus of 90° Courtaulds HMS/Herculus 3002M as a function of temperature. Data of Ref. 29 modeled by Equation (4.10).

5.2. Evaluation of the Fatigue S-N Relation

Experimental data extracted from the literature [34,40] have been used to evaluate fatigue S-N relation (4.20). The tested materials, the type of plies and laminates, the reported fibre volume fraction of some specimens, and also the amount of the experimentally obtained intercept A at room temperature have been listed in Table A-5. The extracted data from the literature have been tabulated in Appendix B. The following section describes the fatigue testing condition and data taken from the literature.

5.2.1 Jen *et al.* Data

Jen *et al.* [34] conducted tension-tension fatigue tests using MTS 810 testing machine in load control condition with a stress ratio of $R = 0.1$ and sinusoidal waveform at a frequency of 5 Hz on graphite/PEEK prepregs. The prepregs were used to make AS-4/PEEK cross-ply $[0/90]_{4S}$ and quasi-isotropic $[0/+45/90/-45]_{2S}$ laminate samples. The specimen size and fibre volume fraction were given as $L = 240$ mm, $W = 25.4$ mm, and $t = 2$ mm and 61%. The T_g of PEEK was reported to be 416 K. The fatigue tests were performed at RT (25°C), 75°C, 100°C, 125°C, and 150°C. The specimens were fatigue tested for up to 10^6 cycles.

5.2.2 Kawai and Taniguchi Data

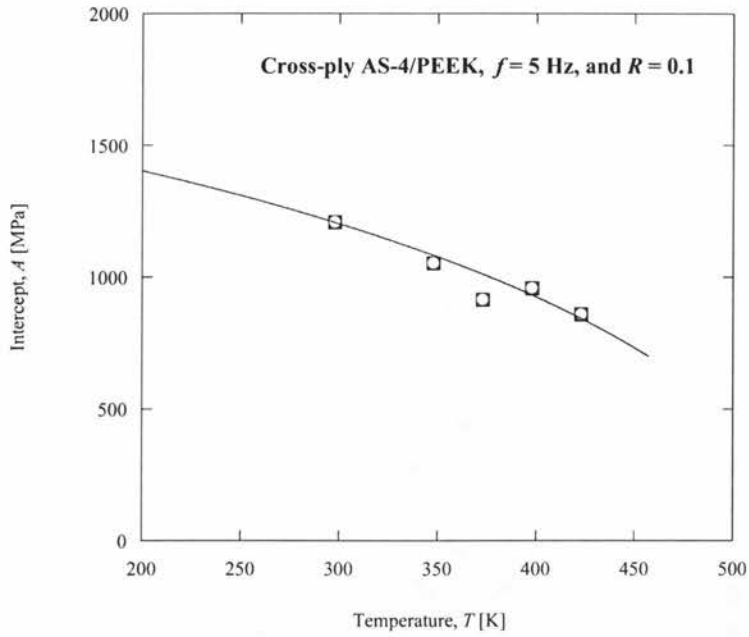
Kawai and Taniguchi [40] fatigue tested composite laminate samples of carbon/epoxy with woven fabric lay-ups. The prepreg tape F6343B-05 (TORAY) made of carbon fibre T300 and thermosetting epoxy resin # 2500 ($T_g = 403$ K). Five kinds of plain coupon specimens with different fibre orientations ($\theta = 0, 15, 30, 45,$ and 90°) were cut from 400 mm by 400 mm laminate panels. The off-axis angle θ has been defined as the angle between the loading direction and the warp direction of the specimens. The dimensions of the specimens were reported as $L = 200$ mm, $W = 20$ mm, and $t = 3$ mm. Tension-tension fatigue tests were performed on the specimens at room temperature (25°C) and the temperature of 100°C under load control condition. The fatigue load was applied in a sinusoidal waveform with a frequency of 10 Hz and stress ratio $R = 0.1$. The specimens were fatigue tested for up to 10^6 cycles.

5.2.3 Calculated Fatigue S-N Results

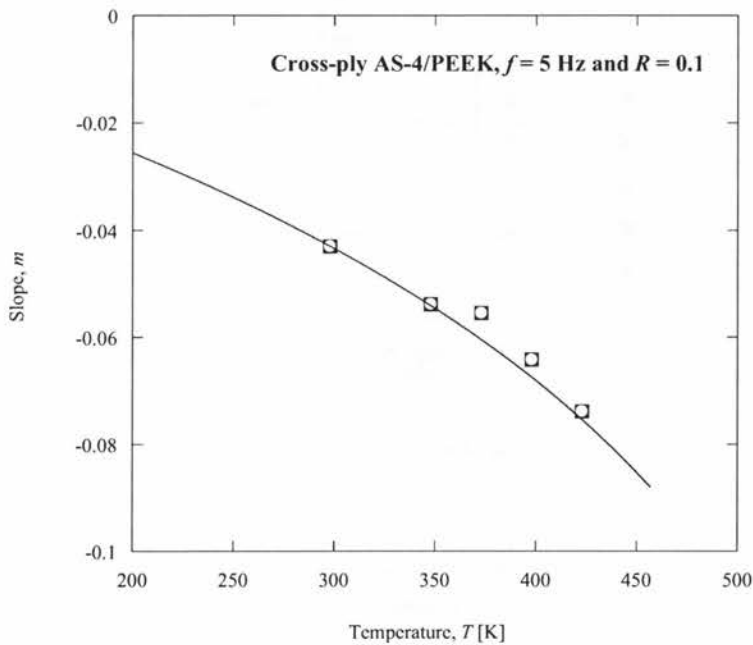
To calculate the fatigue S-N relation using Equation (4.20), the following parameters are required:

- i. The amount of A and m at room temperature, $A(T_0 = \text{RT})$ and $m(T_0 = \text{RT})$.
- ii. The amount of A at 0 K, $A(0)$.
- iii. Room temperature, RT, and the polymer melting point of the tested laminated FRP composite, T_m .

To evaluate Equation (4.20), sixteen different fatigue S-N data sets obtained at various temperatures [34,40] were examined. All the parameters required to calculate the fatigue S-N relation were taken from the literature and listed in Tables A-5 and A-6. Temperature dependent exponent m and coefficient A were first calculated (see Figures 5.14, 5.17, 5.20, 5.23, and 5.26). Equation (4.20) has been used to assess fatigue life for cross-ply and quasi-isotropic graphite/epoxy laminates and various woven graphite/epoxy composites with off-axis angles of 15°, 30°, and 45°; Figures 5.15, 5.18, 5.21, 5.24, and 5.27 present the predictions. Predicted fatigue lives of composite samples were compared with the experimental S-N data and presented in Figures 5.16, 5.19, 5.22, 5.25, and 5.28. The figures show that the fatigue data outside of plotted dashed lines (± 3 factor bands) correspond to experimentally obtained S-N data [34,40] at operating temperatures near the glass transition temperature T_g , at which the polymer is changed to a viscous state.



(a)



(b)

Figure 5.14: The relationships of (a) intercept and (b) slope with temperature for $[0/90]_{4S}$ AS-4/PEEK respectively modeled by Equations (4.17) and (4.18) and correlated with the experimentally obtained intercepts and slopes.

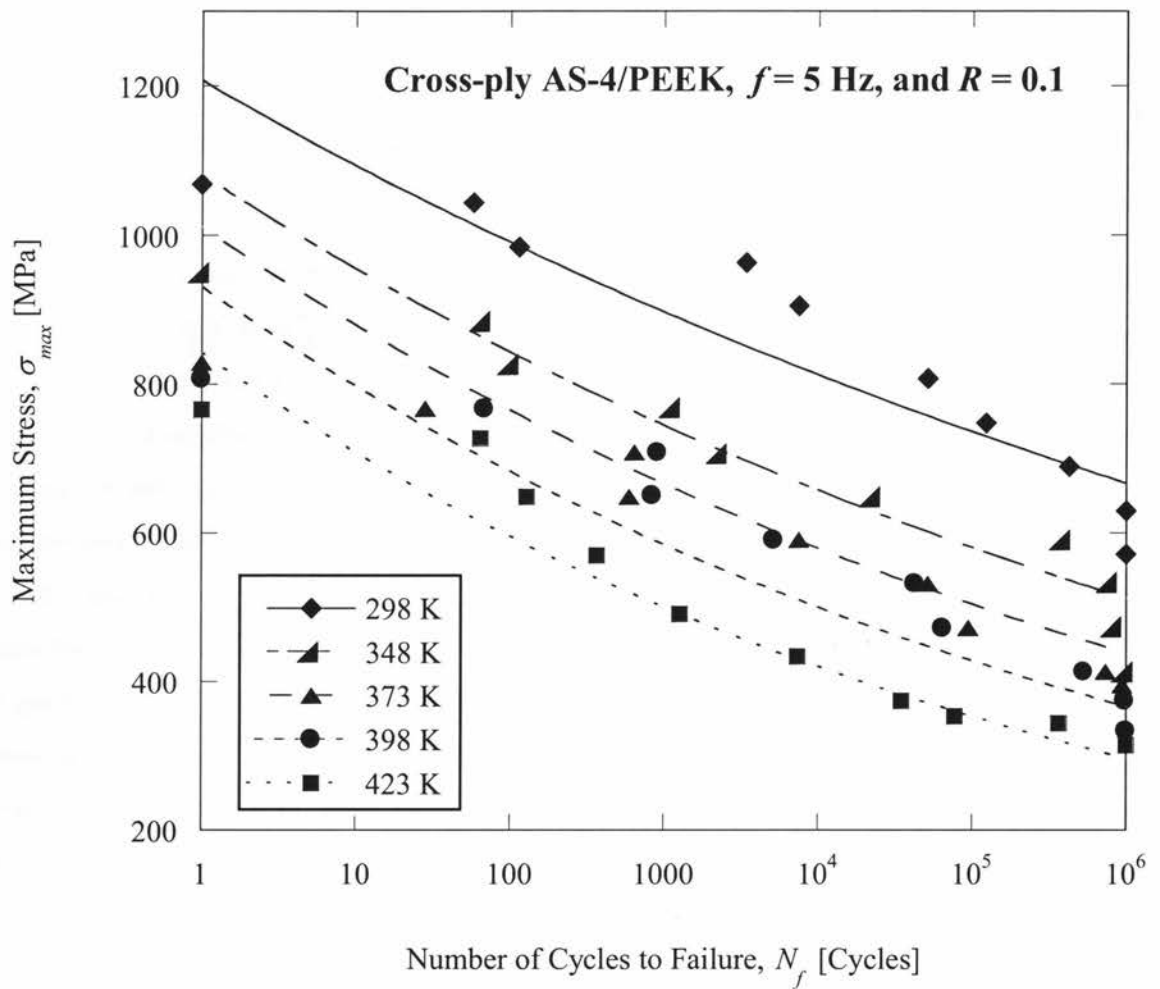


Figure 5.15: S-N equations of $[0/90]_{4S}$ AS-4/PEEK at different temperatures. Data extracted from Ref. 34 modeled by Equation (4.20).

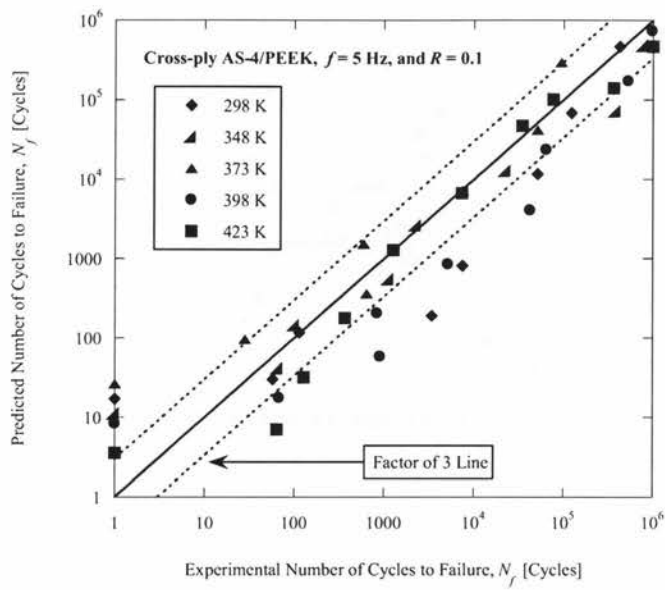
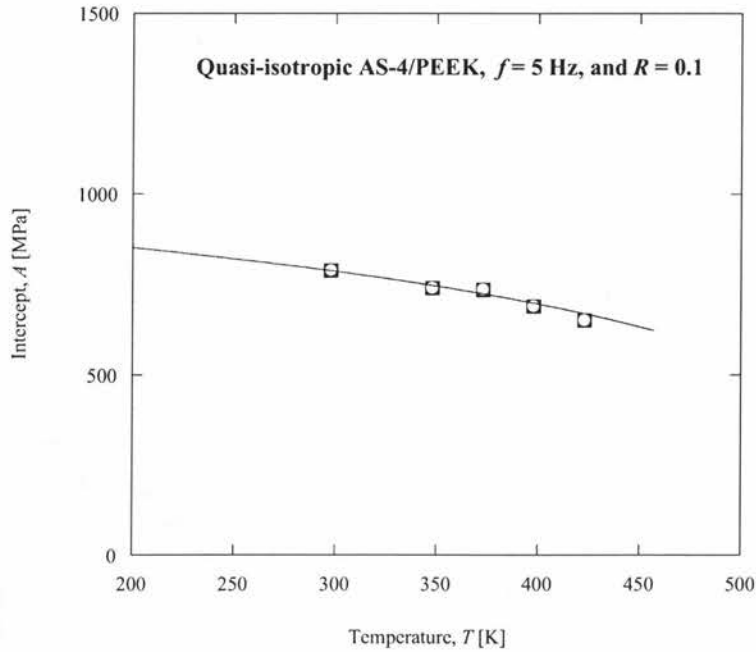
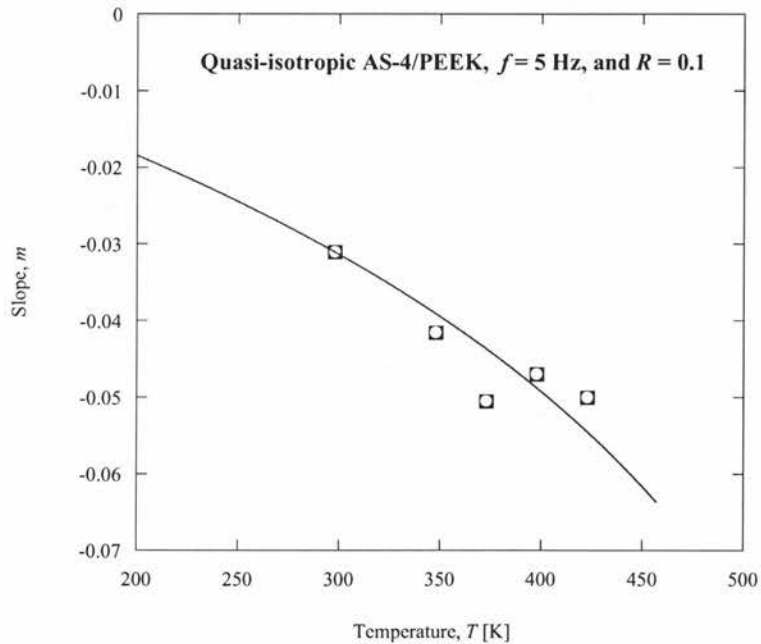


Figure 5.16: Comparison of experimental fatigue lives extracted from Ref. 34 with the fatigue lives predicted with Equation (4.20) for $[0/90]_{4S}$ AS-4/PEEK at different temperatures.



(a)



(b)

Figure 5.17: The relationships of (a) intercept and (b) slope with temperature for $[0/+45/90/-45]_{2S}$ AS-4/PEEK respectively modeled by Equations (4.17) and (4.18) and correlated with the experimentally obtained intercepts and slopes.

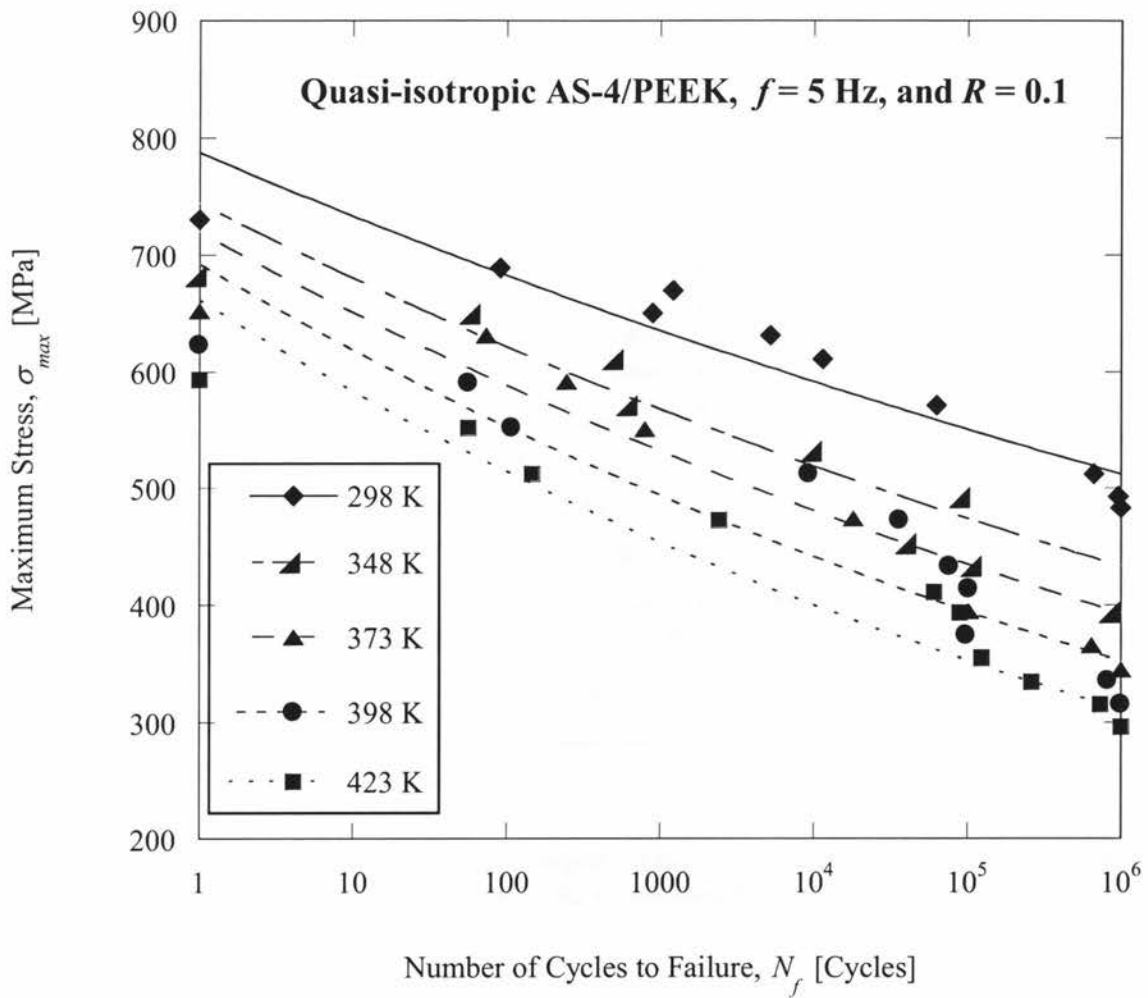


Figure 5.18: S-N equations of $[0/+45/90/-45]_{2S}$ AS-4/PEEK at different temperatures. Data extracted from Ref. 34 modeled by Equation (4.20).

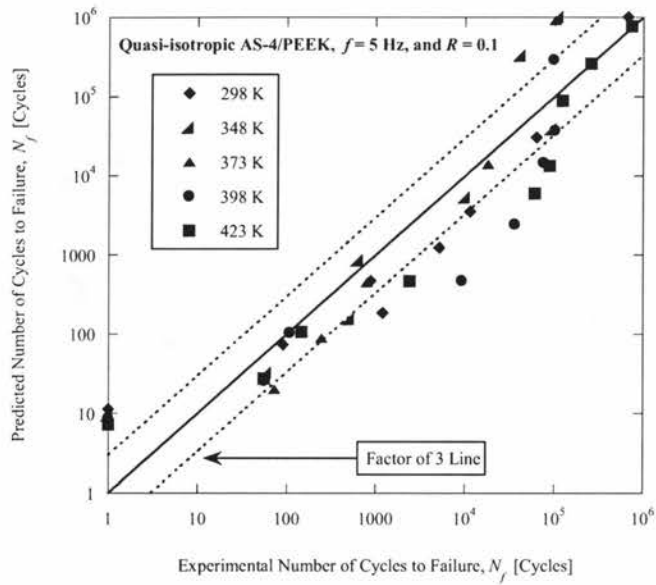
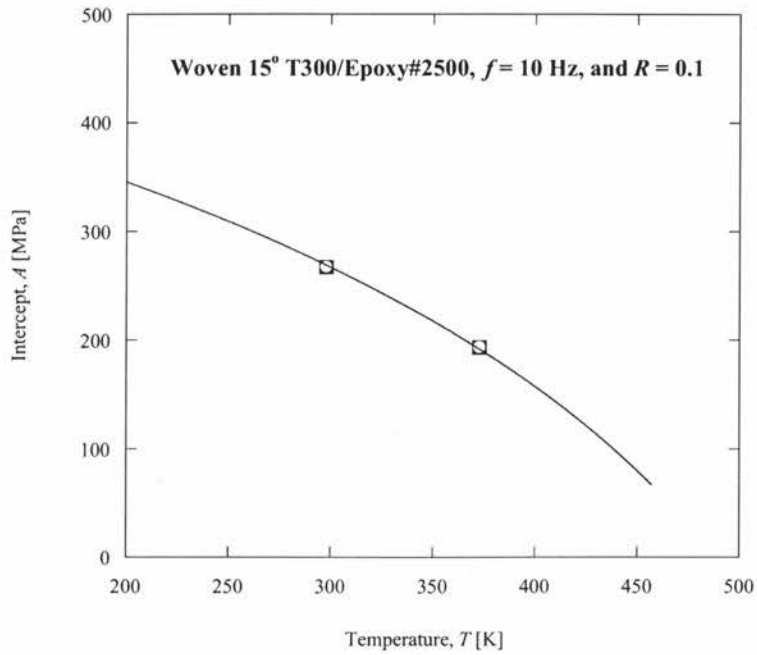
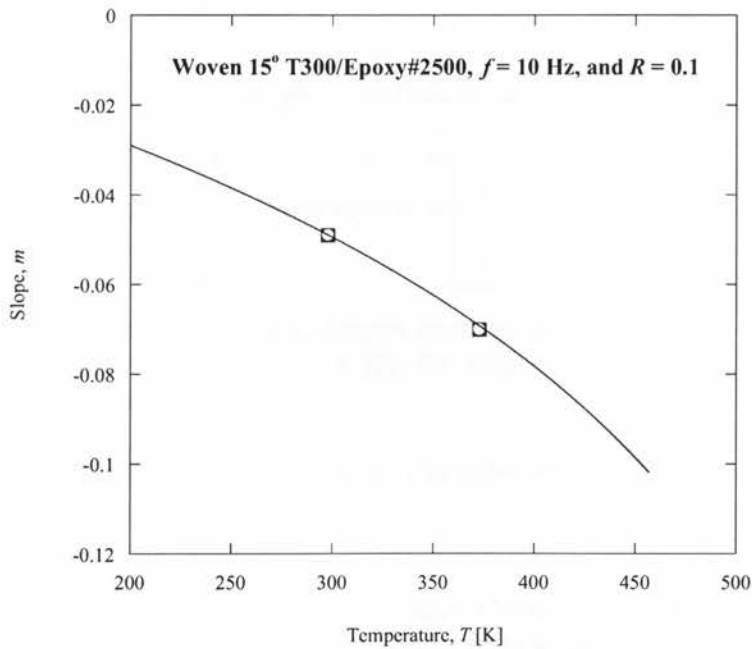


Figure 5.19: Comparison of experimental fatigue lives extracted from Ref. 34 with the fatigue lives predicted with Equation (4.20) for $[0/+45/90/-45]_{2S}$ AS-4/PEEK at different temperatures.



(a)



(b)

Figure 5.20: The relationships of (a) intercept and (b) slope with temperature for plain-woven (15°) T300/Epoxy#2500 respectively modeled by Equations (4.17) and (4.18) and correlated with the experimentally obtained intercepts and slopes.

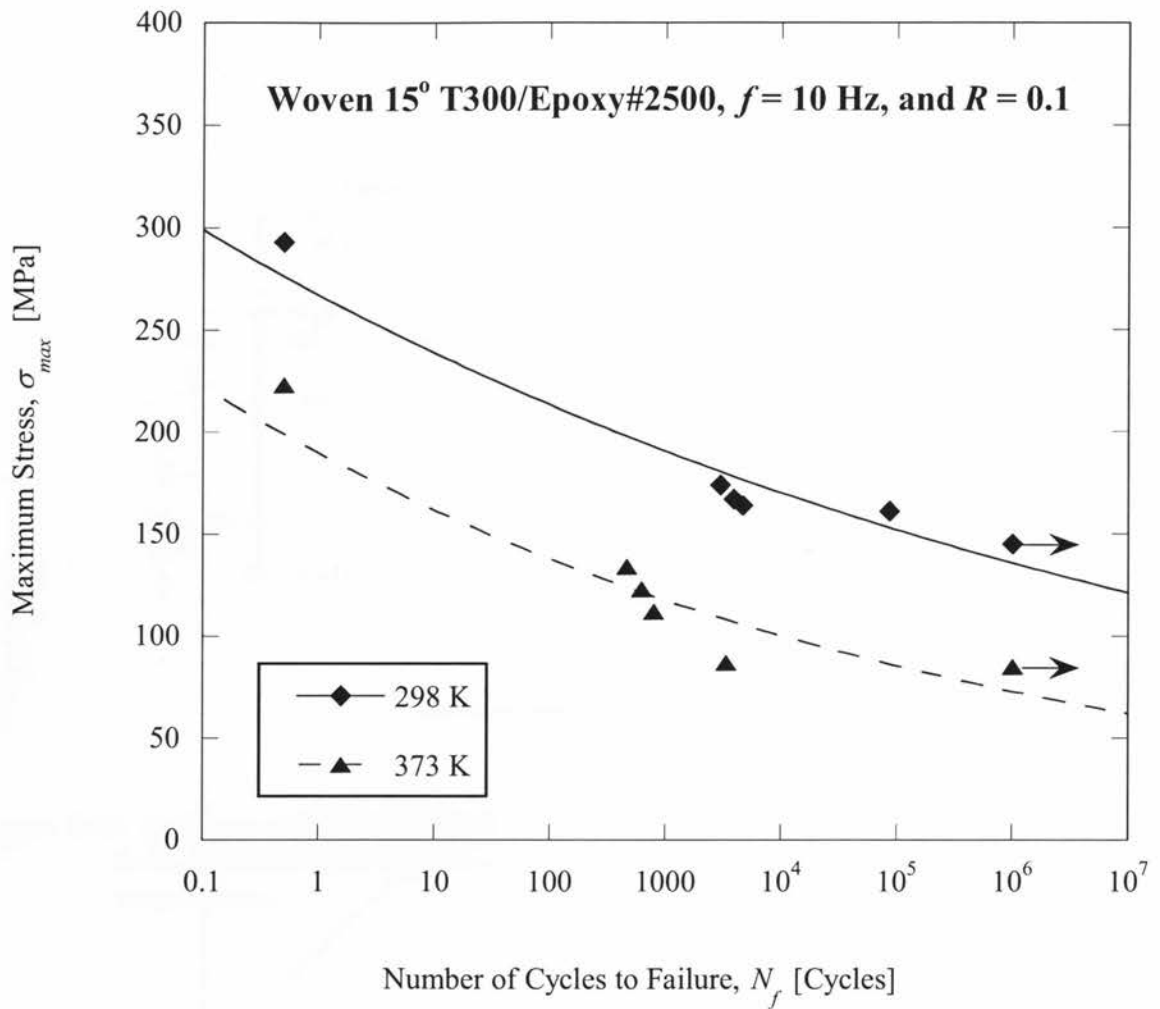


Figure 5.21: S-N equations of plain-woven (15°) T300/Epoxy#2500 at different temperatures. Data extracted from Ref. 40 modeled by Equation (4.20).

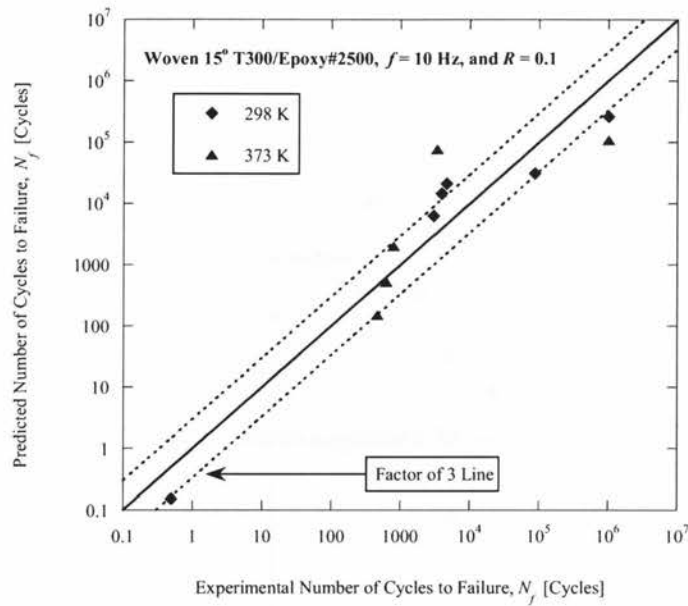
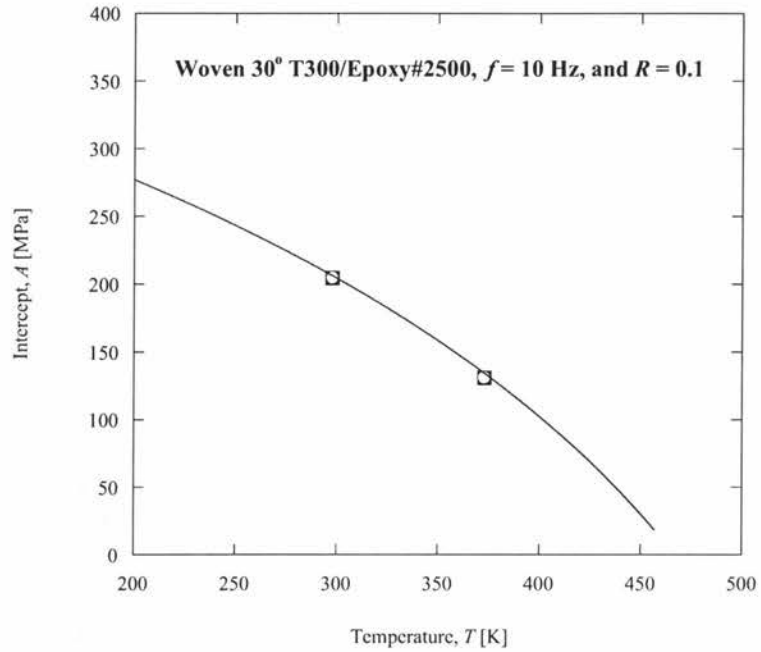
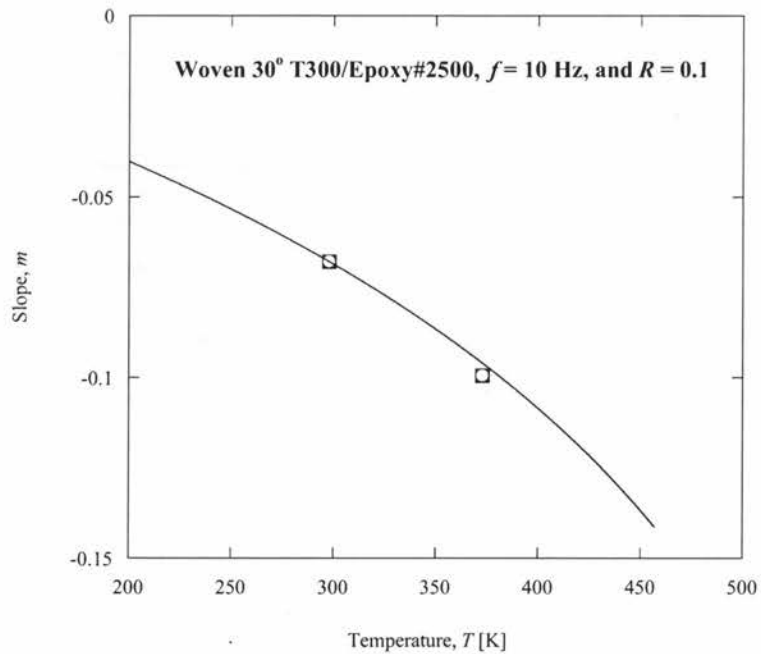


Figure 5.22: Comparison of experimental fatigue lives extracted from Ref. 40 with the fatigue lives predicted with Equation (4.20) for plain-woven (15°) T300/Epoxy#2500 at different temperatures.



(a)



(b)

Figure 5.23: The relationships of (a) intercept and (b) slope with temperature for plain-woven (30°) T300/Epoxy#2500 respectively modeled by Equations (4.17) and (4.18) and correlated with the experimentally obtained intercepts and slopes.

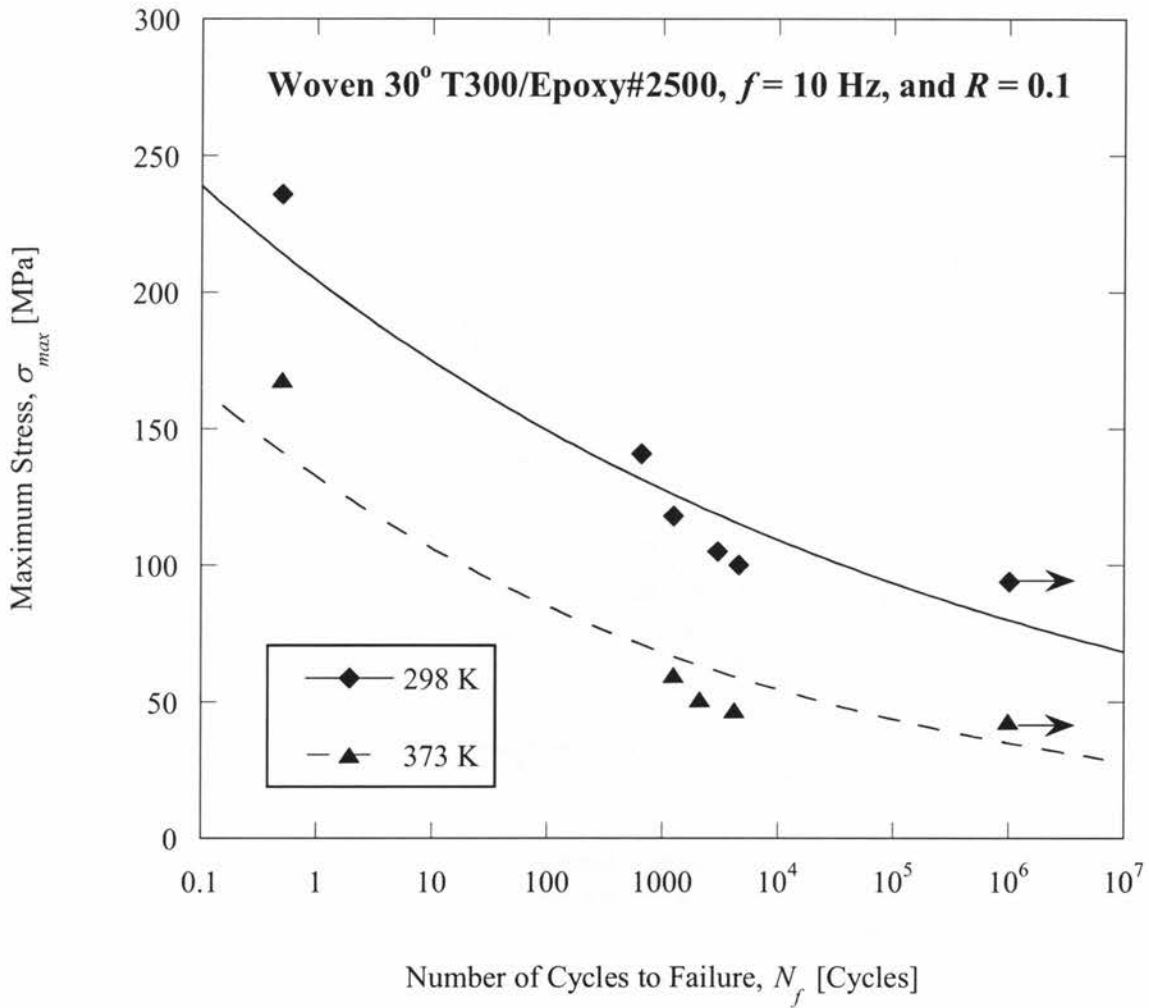


Figure 5.24: S-N equations of plain-woven (30°) T300/Epoxy#2500 at different temperatures. Data extracted from Ref. 40 modeled by Equation (4.20).

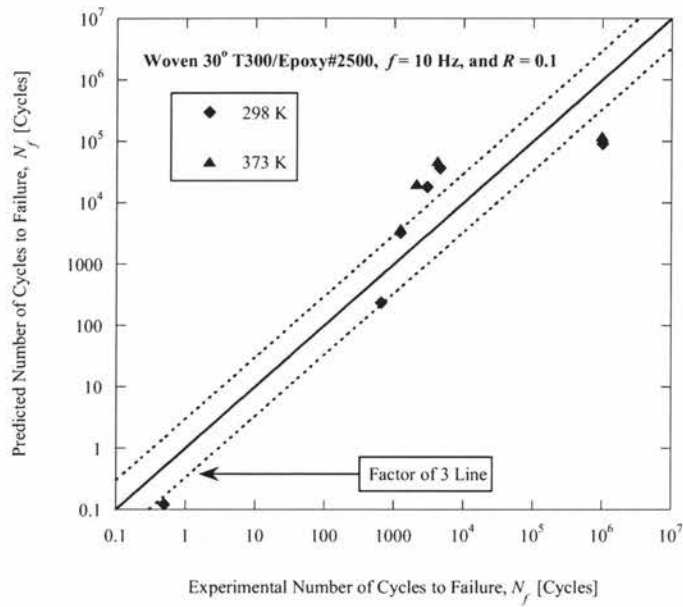
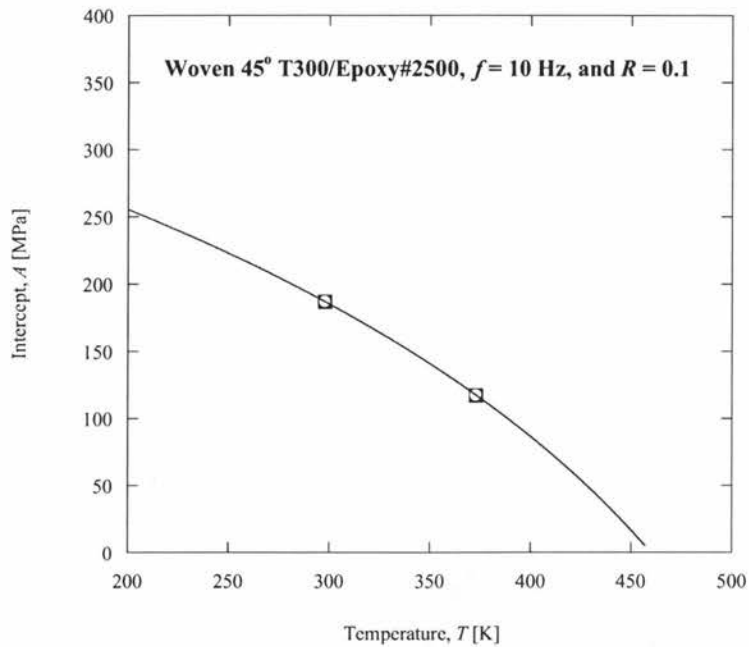
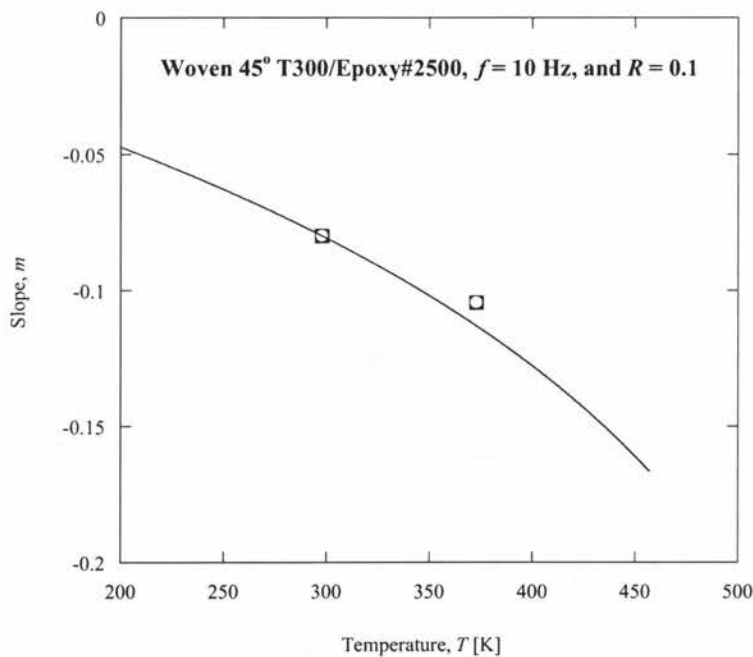


Figure 5.25: Comparison of experimental fatigue lives extracted from Ref. 40 with the fatigue lives predicted Equation (4.20) for plain-woven (30°) T300/Epoxy#2500 at different temperatures.



(a)



(b)

Figure 5.26: The relationships of (a) intercept and (b) slope with temperature for plain-woven (45°) T300/Epoxy#2500 respectively modeled by Equations (4.17) and (4.18) and correlated with the experimentally obtained intercepts and slopes.

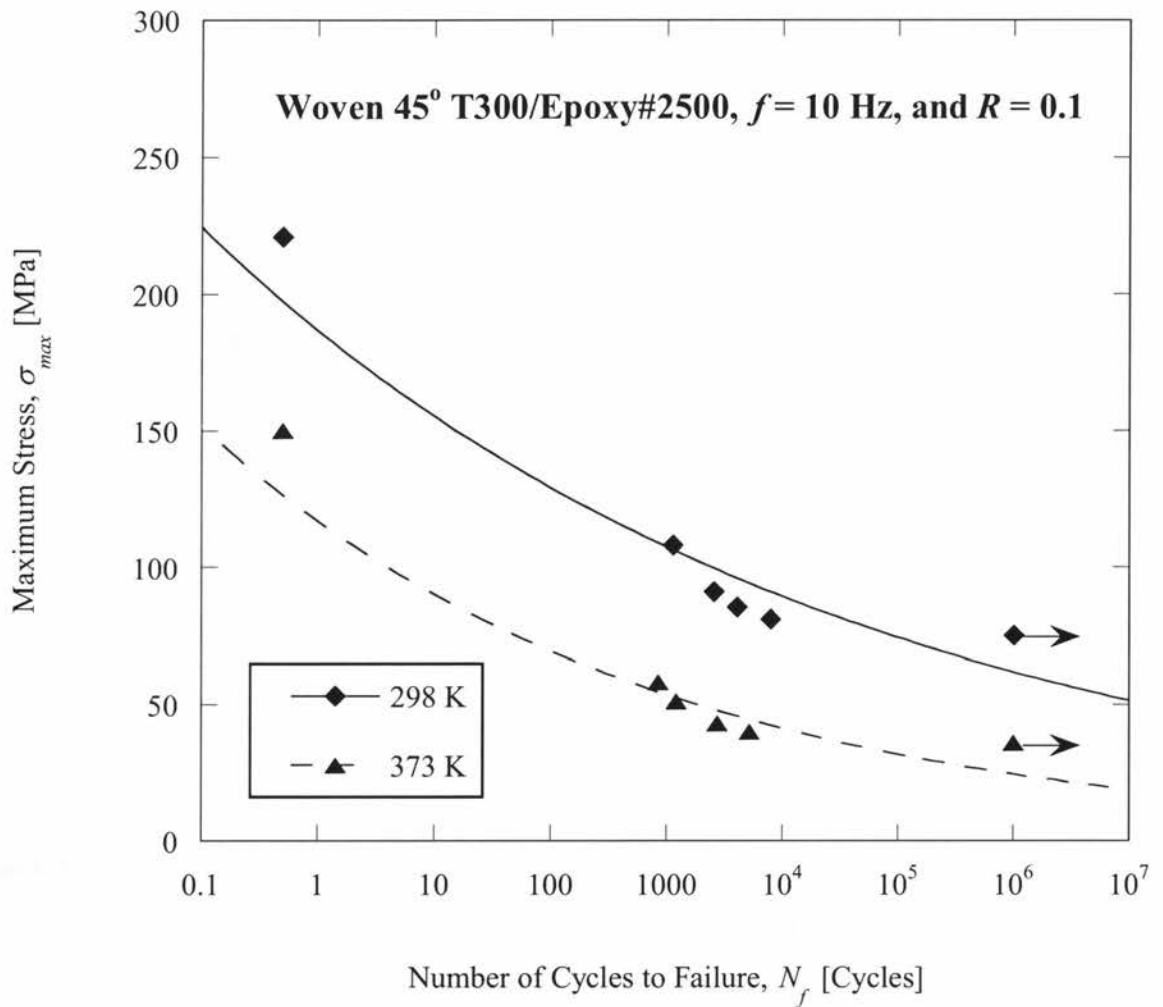


Figure 5.27: S-N equations of plain-woven (45°) T300/Epoxy#2500 at different temperatures. Data extracted from Ref. 40 modeled by Equation (4.20).

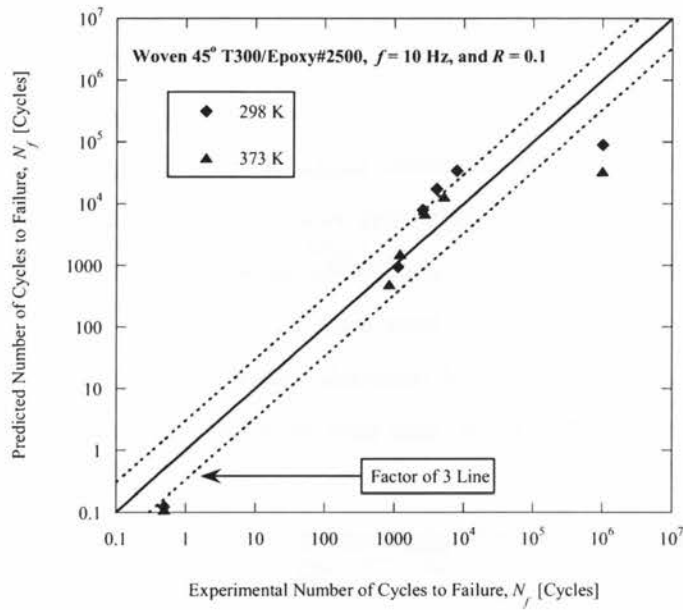


Figure 5.28: Comparison of experimental fatigue lives extracted from Ref. 40 with the fatigue lives predicted with Equation (4.20) for plain-woven (45°) T300/Epoxy#2500 at different temperatures.

5.3 Evaluation of the Fatigue Damage Model

Hiwa *et al.* [41] tested composite samples of plain-woven glass cloth (WF 350) and glass mat (MC 300S) as the reinforced fibres embedded within the matrix of polyvinyl ester resin. The FRP composite samples made by the materials have been laminated by the hand lay-up method. The number of plies in the polyvinyl ester/glass cloth and polyvinyl ester/glass mat were 5 and 3, respectively. Also, the volume fraction of the glass fibres in the cloth and mat were 48% and 35%, respectively. To measure the modulus ratio or fatigue damage of the composite versus number of cycles at different temperatures, different fatigue tests with the loading frequency of 16.7 Hz and the stress ratio of 0 were performed on the specimens. The composites with glass cloth fibres were tested with the maximum stress of 130 MPa at RT (25°C), 50°C, and 70°C. However, the glass mat-reinforced polyvinyl ester composites were tested with the maximum stress of 90 MPa at RT (25°C), 100°C, and 150°C. In this thesis, to evaluate the proposed fatigue damage model, six sets of D-N data have been extracted from the described fatigue damage experiments. A summary of the tested materials and some conditions of the fatigue tests have been listed in Table A-7. The extracted data have been tabulated in Appendix B.

5.3.1 Calculated Fatigue Damage Model Results

To calculate the fatigue D-N relation using Equation (4.21), the following parameters are required:

- i. The material properties of E_f , V_f , V_f^* or K_f , and f^* .
- ii. The amounts of $E_c(T)$ and $\sigma_{ult}(T)$ using Equations (4.9) and (4.10) with knowing RT, T_m , $E_c(\text{RT})$, $\sigma_{ult}(\text{RT})$, and the corresponding constant C .
- iii. The load conditions of σ_{max} , R , n , and N_f .

In this study, to evaluate the proposed fatigue damage model of Equation (4.21), the parameters have been extracted from Ref. 43 and listed in Table A-7. The calculation of the total damage over life cycles is done based on the algorithm described in Section 4.5.1. Figures 5.29–5.34 show the comparison between the calculated and the experimental fatigue damage parameters. As it is seen, there is a good correlation between the predictions and the experimental data.

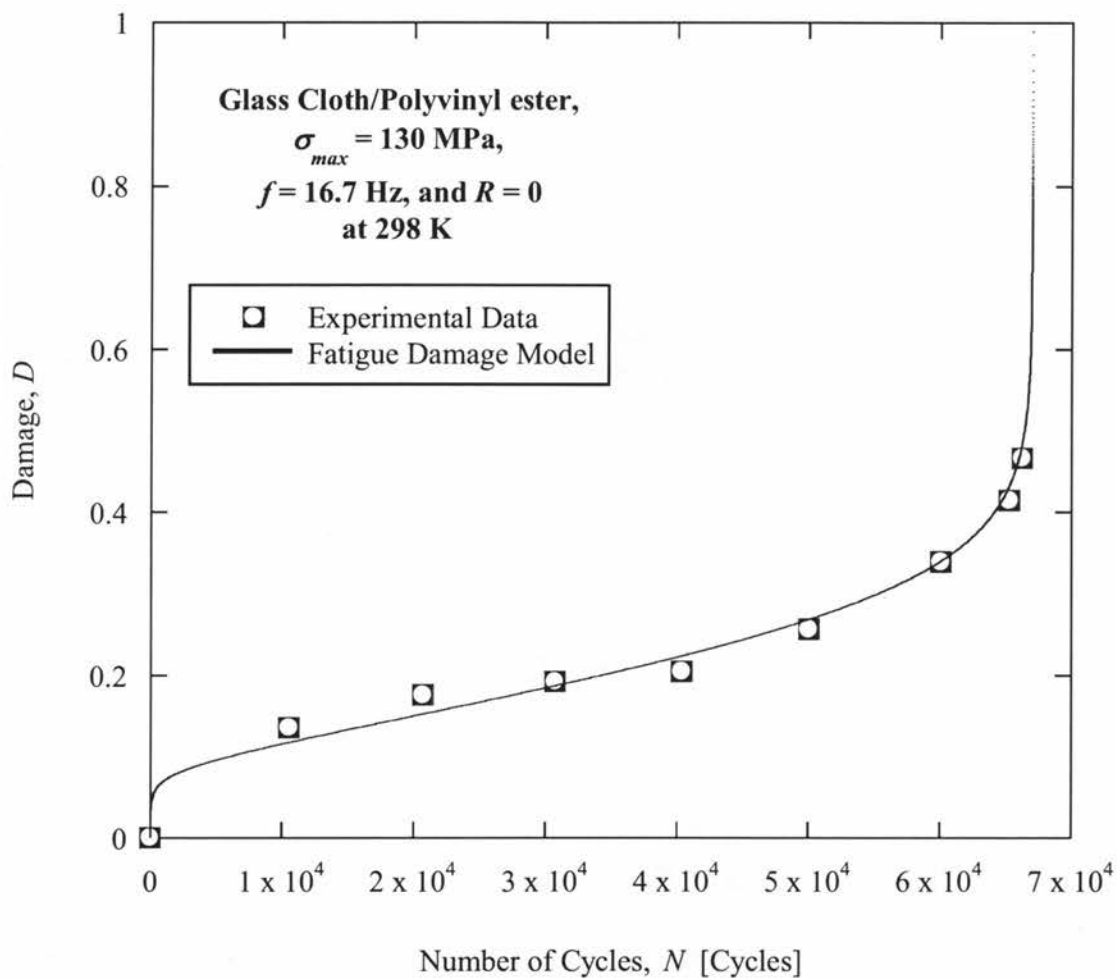


Figure 5.29: Fatigue damage of glass cloth/polyvinyl ester versus number of cycles under $\sigma_{max} = 130 \text{ MPa}$, $f = 16.7 \text{ Hz}$, and $R = 0$ at 298 K. Data of Ref. 41 modeled by Equation (4.21).

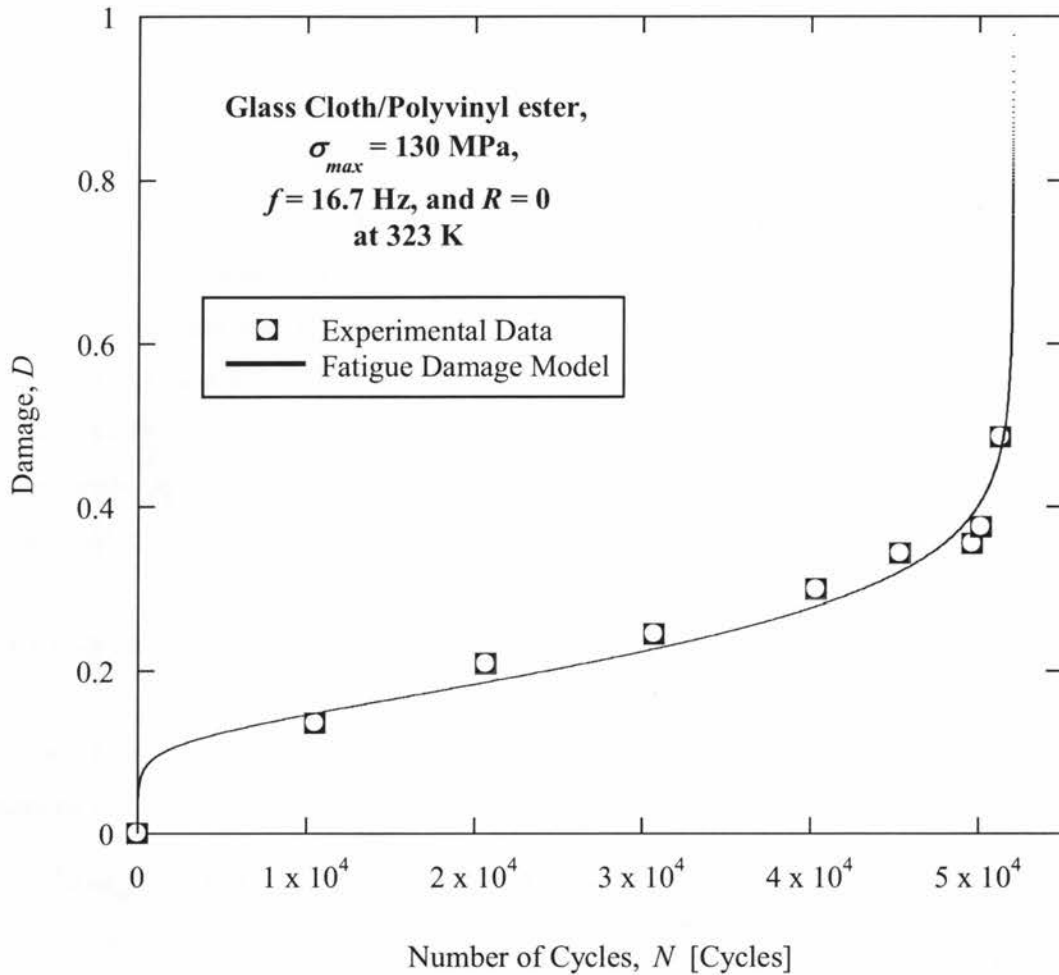


Figure 5.30: Fatigue damage of glass cloth/polyvinyl ester versus number of cycles under $\sigma_{max} = 130 \text{ MPa}$, $f = 16.7 \text{ Hz}$, and $R = 0$ at 323 K. Data of Ref. 41 modeled by Equation (4.21).

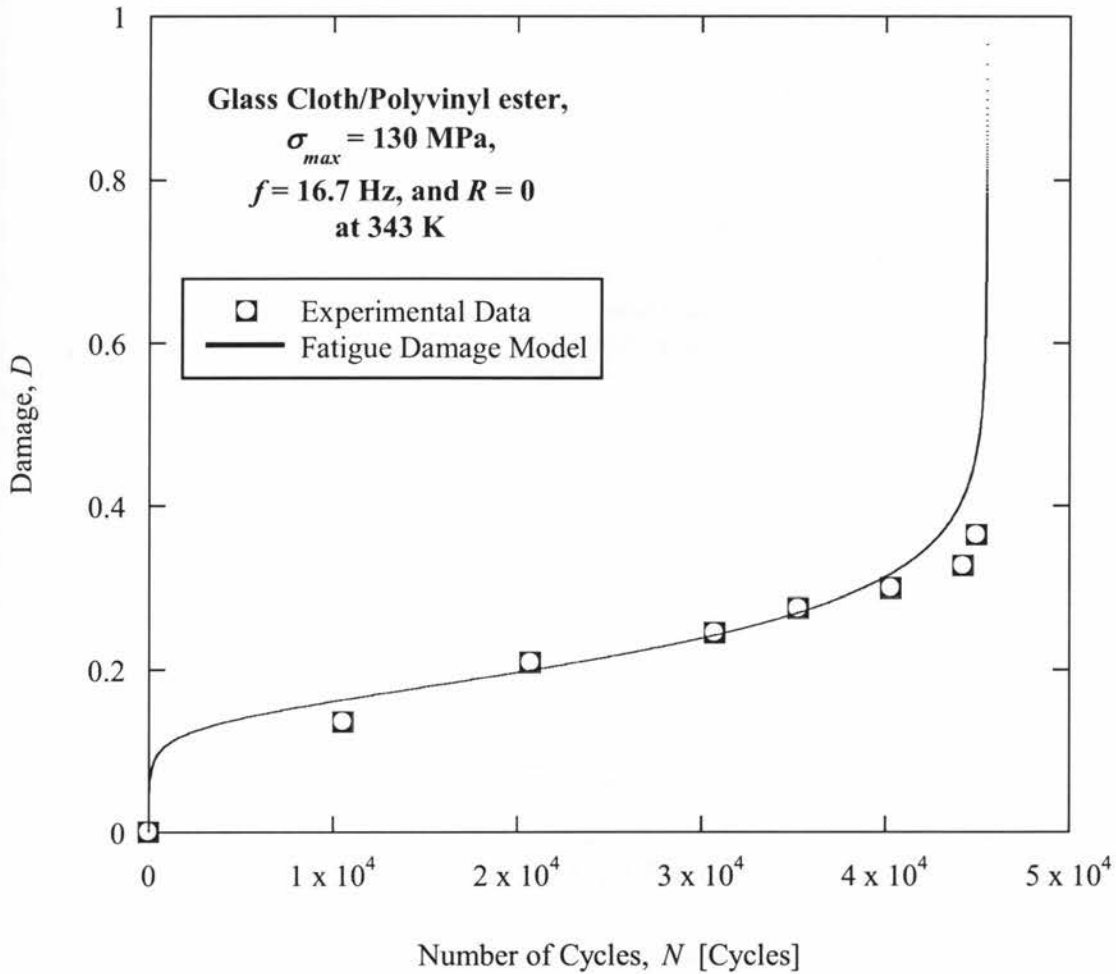


Figure 5.31: Fatigue damage of glass cloth/polyvinyl ester versus number of cycles under $\sigma_{max} = 130 \text{ MPa}$, $f = 16.7 \text{ Hz}$, and $R = 0$ at 343 K. Data of Ref. 41 modeled by Equation (4.21).

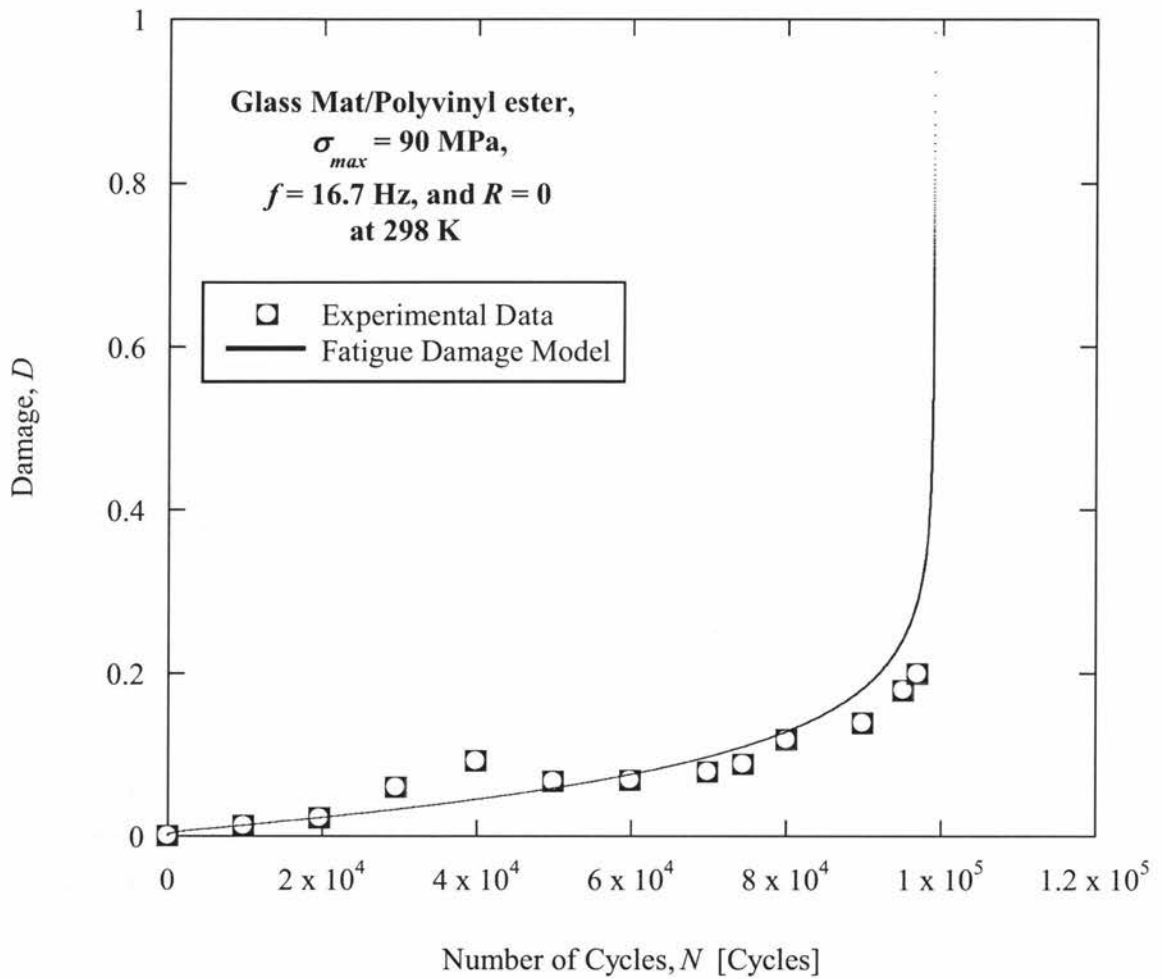


Figure 5.32: Fatigue damage of glass mat/polyvinyl ester versus number of cycles under $\sigma_{max} = 90 \text{ MPa}$, $f = 16.7 \text{ Hz}$, and $R = 0$ at 298 K. Data of Ref. 41 modeled by Equation (4.21).

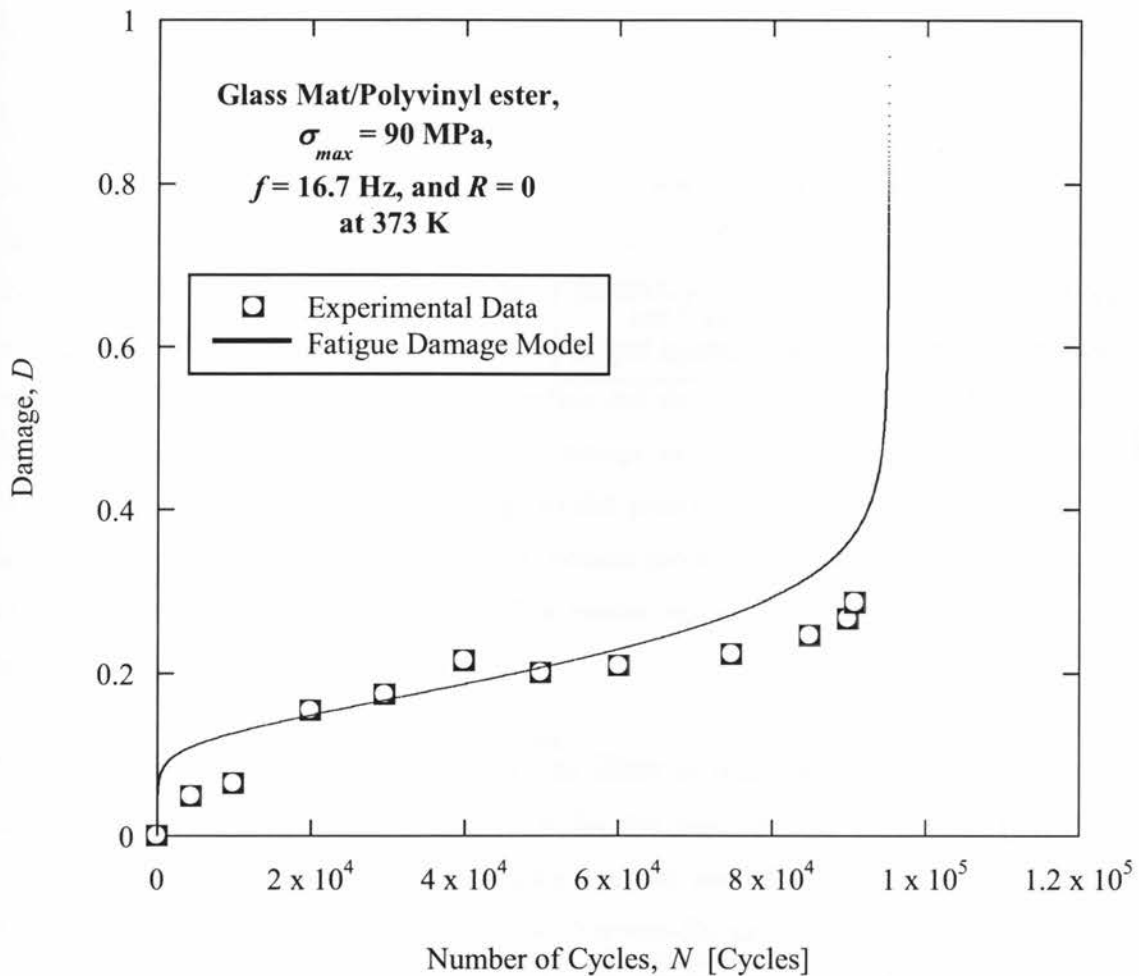


Figure 5.33: Fatigue damage of glass mat/polyvinyl ester versus number of cycles under $\sigma_{max} = 90 \text{ MPa}$, $f = 16.7 \text{ Hz}$, and $R = 0$ at 373 K . Data of Ref. 41 modeled by Equation (4.21).

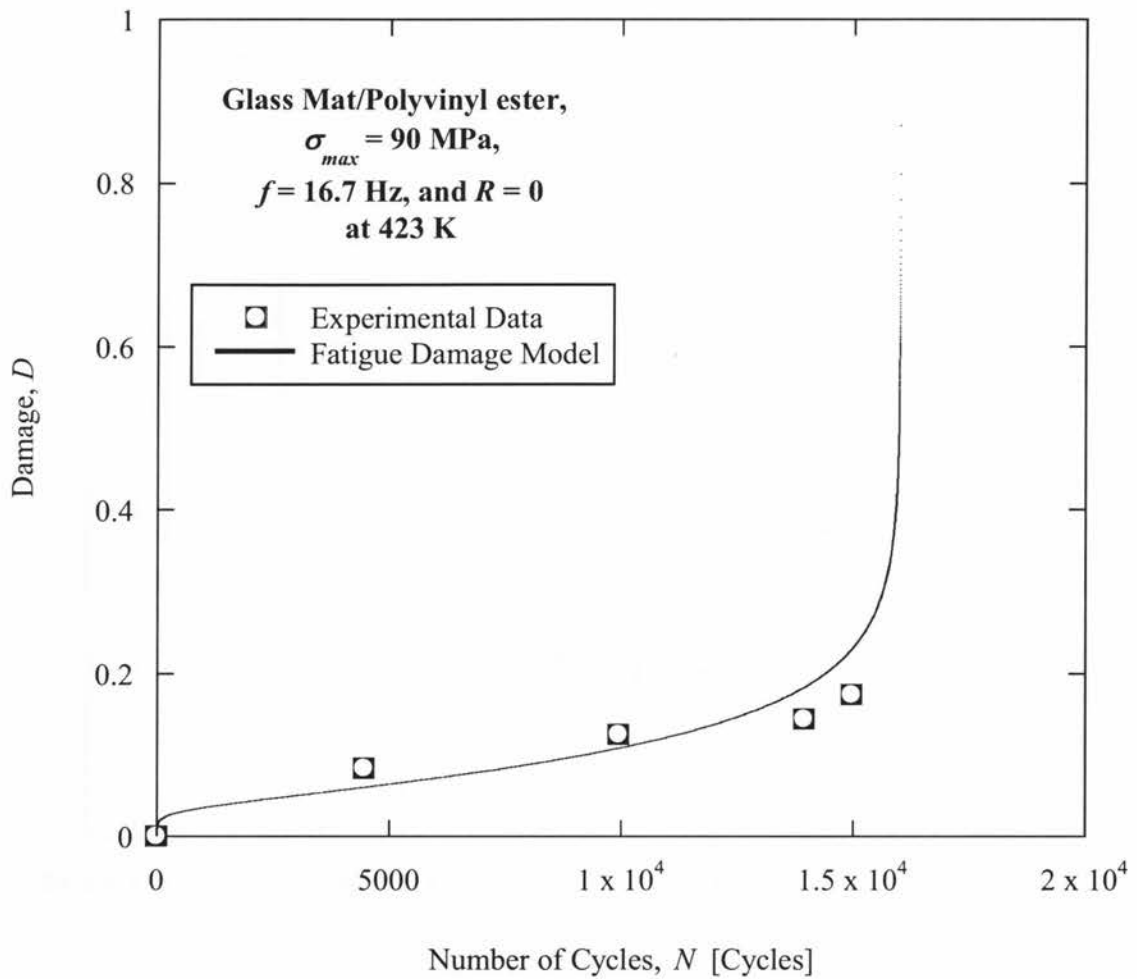


Figure 5.34: Fatigue damage of glass mat/polyvinyl ester versus number of cycles under $\sigma_{max} = 90 \text{ MPa}$, $f = 16.7 \text{ Hz}$, and $R = 0$ at 423 K. Data of Ref. 41 modeled by Equation (4.21).

CHAPTER SIX

Discussion of Results

6.1 General Outlook

As it was discussed, to predict the fatigue damage of composite structures under cyclic loading, a cumulative damage model is a necessity. Researchers have done some work on cumulative damage models, both experimentally and analytically [7,8,9]. The proposed damage models in Refs. 8 and 9 are based on residual stiffness phenomenological damage analysis and take into account the three regions of the damage development based on the physics and the mechanism of cracking in the matrix, the matrix-fibre interface and the fibre. The model proposed in Ref. 8 by Remakrishnan and Jayaraman is capable of damage assessment in on-axis unidirectional fibre-reinforced ceramics. However, the damage model proposed in Ref. 9 by Varvani and Shirazi is not only non-restricted to specific loading directions (on-axis and off-axis), but also considers the effect of mean stress or stress ratio, R . The model has also been shown to be applicable for unidirectional GRP and CFRP composites.

The present study has aimed to investigate the effect of temperature on the cumulative fatigue damage of laminated FRP composites. To fulfill this goal, the Varvani-Shirazi fatigue damage model has been chosen as the backbone of the analysis, and then the temperature dependency of its parameters has been formulated. In the Varvani-Shirazi model, it was found that three parameters including Young's modulus, ultimate tensile strength, and the fatigue life of the composites are temperature-dependent. Therefore, as the first step, the temperature dependency of the parameters was modeled, and then the relations of $E-T$ and $\sigma_{ult}-T$ were implemented in the model to provide the general form of the proposed temperature dependent fatigue damage analysis. The proposed relations were given in Chapter 4, and the evaluation of them was conducted in Chapter 5.

In this chapter, the results obtained from the evaluation of the proposed fatigue damage model

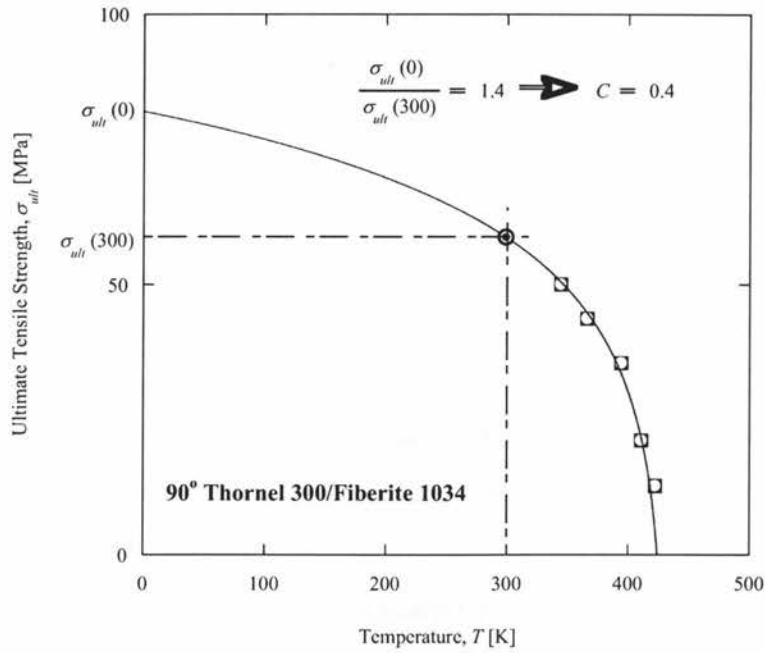
and other temperature dependent relations are discussed. As it was mentioned and shown in the evaluation part, there are different numbers of graphs for the temperature dependent relations. By dividing the discussion into the three parts of monotonic properties, fatigue strength and fatigue damage, the concluded results of each part are analyzed in detail.

6.2 Temperature and the Monotonic Properties

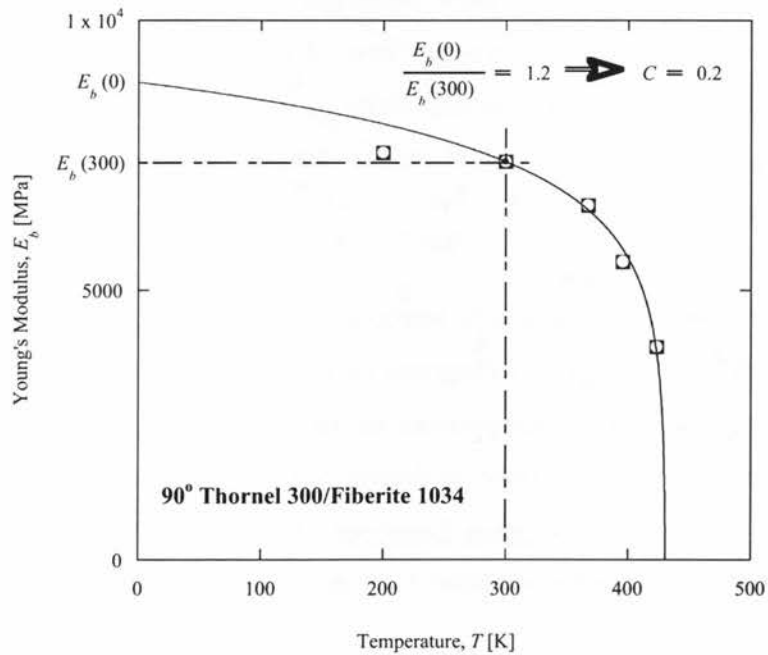
As illustrated in Figures 5.1–5.13, the curves generated using the proposed $\sigma_{ult} - T$ and $E - T$ relations show a good correlation with experimental data. To more clearly illustrate the deviation of the experimental data from the models, the diagrams have not been shown from 0 to T_m . It is obvious that the models can predict the behaviour of the mechanical properties in the entire temperature range.

To formulate and calibrate the temperature dependency of the monotonic properties, various sets of experimental data were extracted from four different references [28,29,33,34]. The type of plies and laminates used in these references included 0° , $[0/90]_{4S}$, $[0/+45/90/-45]_{2S}$, and 90° . The types of materials used as the specimen also included boron/epoxy, aramid/epoxy, S-glass/epoxy, E-glass/epoxy, alumina/PEEK, graphite/PEEK, and different types of graphite/epoxy composites. One of the advantages and strong points of the proposed $\sigma_{ult} - T$ and $E - T$ relations is that they can successfully be applied to all the specimens with a variety of types and laminate structures.

Based on the calculated results presented in Figures 5.1–5.13, the effect of temperature on 0° plies is less than $[0/90]_{4S}$, $[0/+45/90/-45]_{2S}$, and 90° , while 90° lay-ups have the highest sensitivity to temperature changes. The sensitivity to temperature is also different between the ultimate tensile strength and Young's modulus of a composite material. With the exception of Figure 5.2, Figures 5.1–5.13 illustrate the fact that the effect of temperature on the ultimate tensile strength is more pronounced than that on Young's modulus. In the proposed temperature dependent formulation, the sensitivity of the mechanical properties to temperature is evaluated based on the constant C . The bigger C corresponds to a higher temperature sensitivity and vice versa. As an example, the modified graphs of Figure 5.8 are shown in Figure 6.1.



(a)



(b)

Figure 6.1: (a) Ultimate tensile strength and (b) buckling modulus of 90° Thornel 300/Fiberite 1034 as a function of temperature. Data of Refs. 28 and 29 modeled by Equations (4.9) and (4.10), respectively.

The graphs of Figure 6.1 present the variation of ultimate tensile strength and buckling modulus with temperature for 90° Thornel 300/Fiberite 1034 composites. The data have been extracted from Refs. 28 and 29 and have been modeled by Equations (4.9) and (4.10), respectively. As it is seen, the curves based on the equations have been shown in the domain of 0 K to around the polymer melting point. Since, the specimen in the test is a 90° graphite/epoxy composite, the monotonic properties show a relatively high sensitivity to temperature change. However, the amount of the sensitivity is higher for the ultimate tensile strength. This is confirmed by the higher value of C for the ultimate tensile strength. The successful use of the proposed model for the buckling modulus proves the fact that the temperature dependency of two different Young's moduli (the tensile modulus and the buckling modulus) shows a similar trend. This fact has also been reported in Ref. 29.

6.3 Temperature and Fatigue Strength

To formulate and calibrate the temperature dependency of fatigue strength, experimental data of various temperatures have been extracted from different references [34,40]. The type of laminates used in these references include $[0/90]_{4S}$, $[0/+45/90/-45]_{2S}$, and plain-woven (15°), (30°) and (45°). The materials tested under fatigue loading were graphite/epoxy and graphite/PEEK composites.

Figures 5.14–5.28 show the fatigue S-N relations for various operating temperatures for these materials. Formulation of fatigue S-N diagrams for composite samples requires determining both intercept A and exponent m as the temperature increases. Figures 5.14, 5.17, 5.20, 5.23, and 5.26 compare the intercept A and the slope m determined from the experimental S-N curves with diagrams of $A-T$ and $m-T$ plotted using Equations (4.17) and (4.18). The calculated intercepts and slopes were used to obtain the predicted S-N curves at different temperatures.

Figures 5.15, 5.18, 5.21, 5.24, and 5.27 show the predicted fatigue S-N curves. The general behaviour or rule concluded from the figures is that by increasing temperature, the fatigue strength of laminated FRP composites is decreased. In the curves, the “decrease” of fatigue strength is associated with the reduction of intercept A and/or the increase of slope m . The

experimentally obtained S-N curves also follow the general rule; however, exceptions exist. As two examples, the experimentally obtained S-N curves for $[0/90]_{4S}$ and $[0/+45/90/-45]_{2S}$ AS-4/PEEK specimens at different temperatures are presented in Figures 6.2 and 6.3.

Generally, in both Figures 6.2 and 6.3, the experimental S-N curves shift to lower fatigue strength as the magnitude of operating temperature increases. The highest fatigue strength in these figures belongs to test data at 298 K, while the lowest fatigue S-N data results from tests conducted at 423 K. The highest fatigue strength is associated with the highest intercept A and the lowest slope m , while the lowest fatigue strength is related to the lowest A and the highest m .

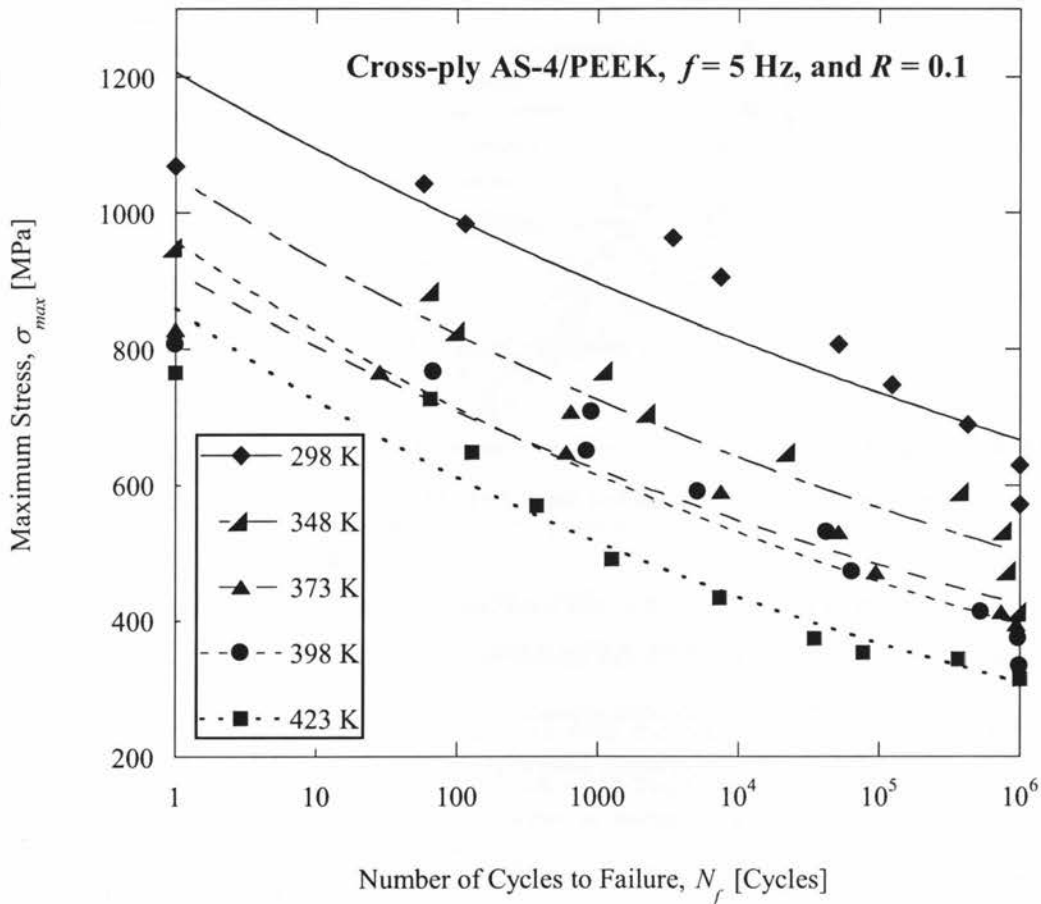


Figure 6.2: Experimentally obtained S-N curves for $[0/90]_{4S}$ AS-4/PEEK at different temperatures. Data extracted from Ref. 34.

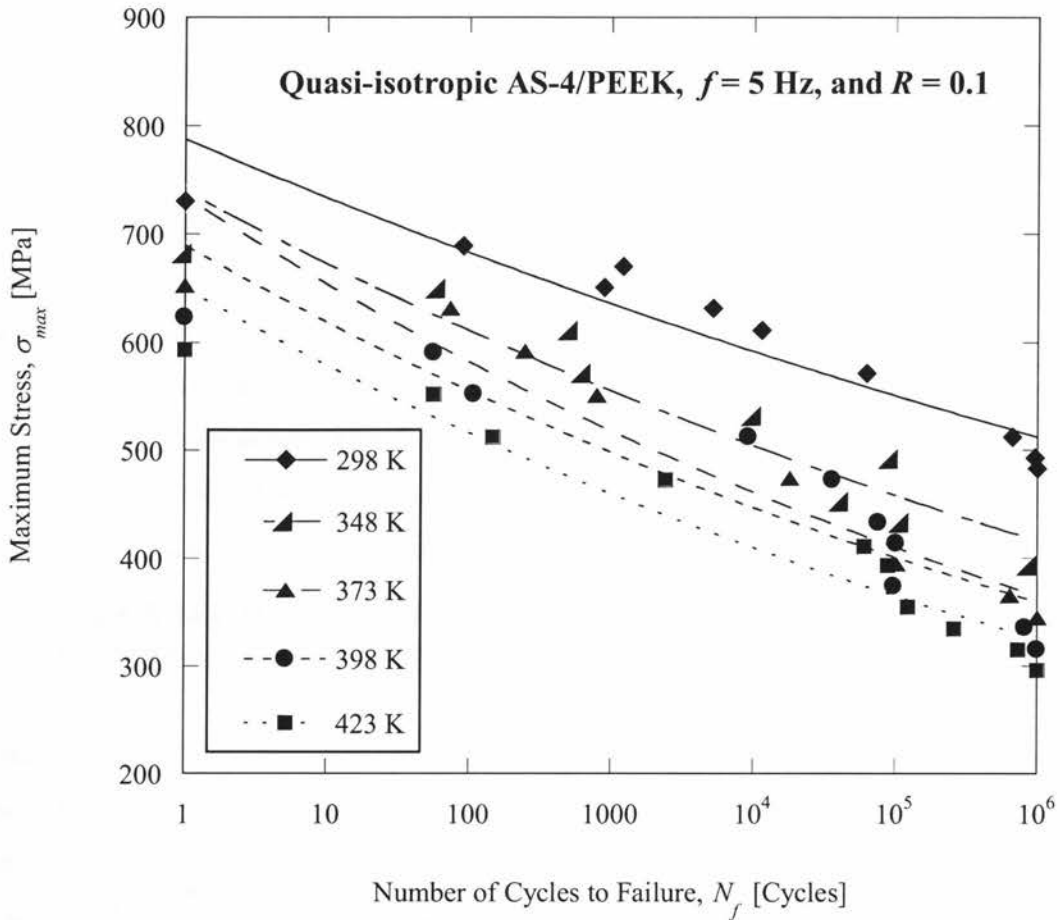


Figure 6.3: Experimentally obtained S-N curves for $[0/+45/90/-45]_{2S}$ AS-4/PEEK at different temperatures. Data extracted from Ref. 34.

In Figure 6.2, as temperature increases, the intercepts of the S-N curves decrease. However, this trend stops at around 398 K, at which the intercept is suddenly increased. For temperatures above 398 K or above the glass transition temperature of PEEK ($T_g = 416$ K), the intercepts are reduced again. It is noteworthy that by increasing temperature, the slopes of the curves show a continuous increasing trend. If there is a situation in which, by increasing temperature, the intercepts are continuously decreased but the slopes do not show the expected increasing trend, the decreasing trend of fatigue strength will also be deranged. This phenomenon has been observed for the fatigue S-N data of quasi-isotropic graphite/PEEK specimen. Figure 6.3 clearly presents the situation. In both the figures, the deviations from the normal trends occurred at around 398 K which is very close to the T_g . These behaviours may be attributed to the change of the composite

matrix state around the glass transition temperature where matrix shows viscoelastic response.

A comparison between the experimentally obtained fatigue lives and the predicted lives based on S-N relation (4.20) was presented in Figures 5.16, 5.19, 5.22, 5.25, and 5.28. These figures include five different materials and lay-ups fatigue tested at various temperatures. Figure 6.4 compares sixteen different sets of the experimental life data with the predicted fatigue lives. This figure, with over 130 fatigue life data tested at various temperatures, successfully collapses 80% of fatigue life data between the upper and the lower bands shown by dashed lines. The 20% of the data which deviated from the ± 3 bands were attributed to temperatures near the glass transition temperature T_g , at which the matrix shows a change in status.

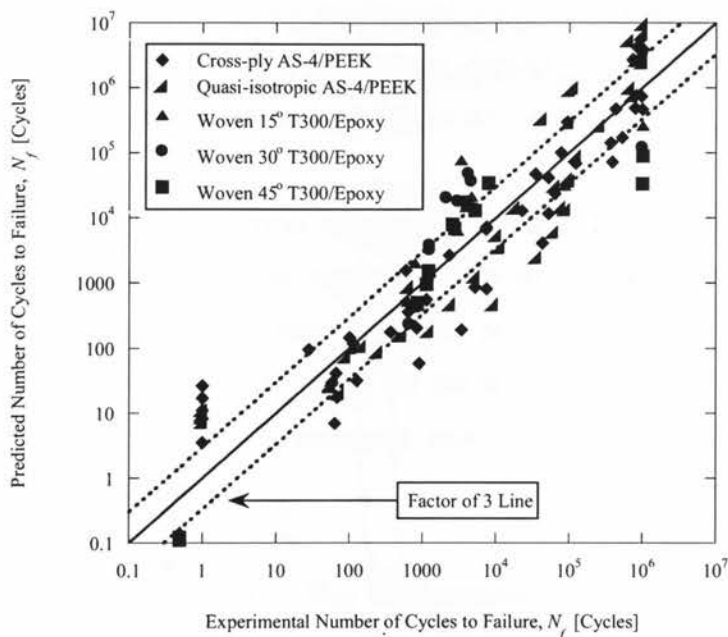


Figure 6.4: Comparison of experimental life data with the predicted fatigue lives of Equation (4.20) for sixteen different sets of data extracted from Refs. 34 and 40.

6.4 Temperature and Fatigue Damage

To evaluate fatigue damage Equation (4.21) as the proposed fatigue damage model, six sets of D-N data were extracted from the literature. The data had been obtained by fatigue tests with the

loading frequency of 16.7 Hz and the stress ratio of 0. The tests were performed on glass cloth/polyvinyl ester with the maximum stress of 130 MPa at RT (298 K), 323 K, and 343 K and the glass mat/polyvinyl ester with the maximum stress of 90 MPa at RT (298 K), 373 K, and 423 K. The D-N data modeled with Equation (4.21) have been illustrated in Figures 5.29 to 5.34. In all the graphs, the experimental data show a good correlation with the model.

The main point concluded from the D-N graphs is that, with increasing temperature, the cumulative fatigue damage is increased. The damage increase is due to the damage growth in each of the three regions of I (matrix cracking), II (fibre/matrix interface cracking), and III (fibre breakage). To understand the point more clearly, as an example, all the three D-N curves for the glass cloth/polyvinyl ester at 298, 323, and 343 K are shown together in Figure 6.5. In this figure, as temperature increases, fatigue life decreases, and fatigue damage in each of the three regions of I, II, and III increases. Therefore, the overall cumulative fatigue damage increases.

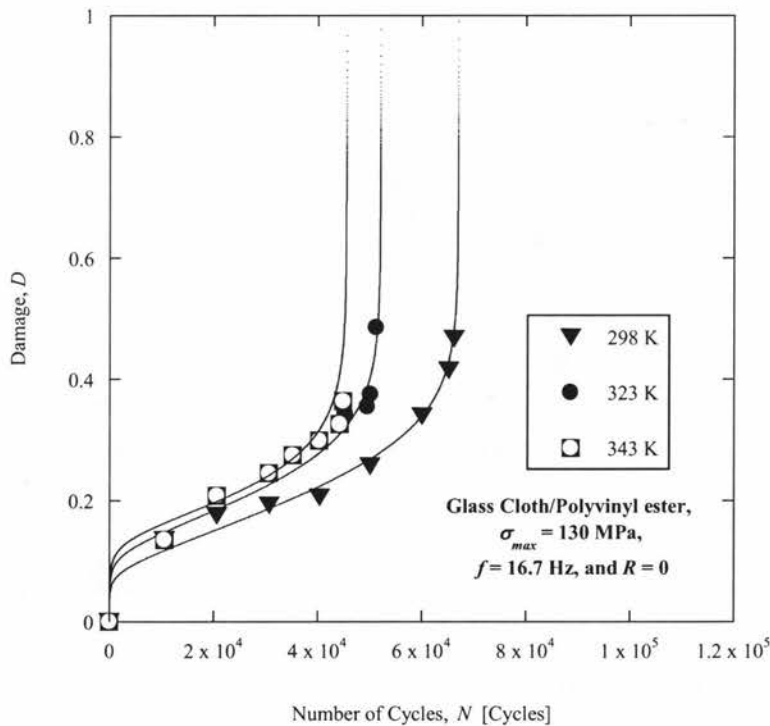


Figure 6.5: Fatigue damage of glass cloth/polyvinyle ester versus number of cycles under σ_{max} =130 MPa, f = 16.7 Hz, and R = 0 at 298 K, 323 K and 343 K. Data of Ref. 41 modeled by Equation (4.21).

CHAPTER SEVEN

Conclusion and Recommendation

7.1 Conclusion

The static and fatigue behaviours of laminated FRP composites as inhomogeneous and anisotropic materials are influenced by different parameters such as: fibre/matrix lay-up, laminate stacking sequence, loading conditions, and environmental conditions. Since FRP composites are viscoelastic materials, their mechanical properties are temperature dependent. In this study, the effect of temperature on the fatigue damage of laminated FRP composites, ultimate tensile strength, Young's modulus, and fatigue strength of the materials was formulated.

As a comparison between bulk polymers as isotropic materials and laminated FRP composites, it was pointed out that the variations of the ultimate tensile strength and Young's modulus with temperature are different in the two materials. The presence of continuous fibres in the composites was introduced as the main reason for the difference. It was also mentioned that when fibre dominance becomes less pronounced and/or fibre volume fraction reduces, the strengths of the FRP laminates reduce.

It was discussed that among the different plies and laminates of FRP composites, 0° plies have the highest ultimate tensile strength and Young's modulus, and 90° plies have the lowest. The variation of σ_{ult} and E in 0° lay-ups with temperature is usually very small, and the parameters remain almost unchanged by increasing temperature to around the polymer melting point of the composite. At temperatures very close to the melting point, the mechanical properties dramatically decrease and finally go to zero. However, σ_{ult} and E in 90° lay-ups usually have the highest variation with temperature when compared to other plies and laminates. The high sensitivity to temperature was described as the matrix dominance of the lay-ups. Off-axis unidirectional, angle-ply, cross-ply, and woven laminates mostly show behaviours intermediate

between the two lay-ups. To characterize the temperature dependent parameters, a shifting factor concept was introduced, which is able to predict the mechanical properties of 0° , 90° , and the intermediate composite lay-ups.

The proposed shift factor equation is advantageous over the WLF and the Arrhenius equations. These two equations are merely suitable for bulk polymers, and they are applicable at temperatures above the glass transition temperature of the polymer. However, the proposed shift factor equation is applicable for laminated FRP composites at operating temperatures between 0 K to the polymer melting point (T_m).

Using the proposed shift factor, monotonic mechanical properties of laminated FRP composites including E and σ_{ult} were formulated as a function of temperature. Based on the power-law S-N relation, both the coefficient A and the exponent m of the relation were found to be temperature-dependent. The coefficient of the S-log N diagram graphically intercepts the curve with the cyclic stress axis at $N = 1$ cycle, while the exponent presents the slope of this curve. It was described that the temperature dependency of the intercept can be modeled very similarly to the ultimate tensile strength. The temperature dependency of the slope m was also calibrated using several sets of experimental data available in the literature. Sixteen sets of S-N data taken from the literature were used to evaluate the S-N relation (4.20). The predicted fatigue lives were found to be in a very close agreement with the experimental life data obtained from five different composite materials.

The cumulative fatigue damage model of Varvani-Shirazi was further developed based on temperature dependent parameters. The fatigue damage equation was evaluated using six sets of damage data extracted from the literature. Comparison of the D-N curve predicted using Equation (4.21) and the experimental values of damage versus fatigue cycles were found to be in good agreement.

7.2 Recommendation

The fatigue damage of FRP composites is a function of various parameters. Some of these

parameters include loading frequency, moisture, and ultra violet radiation. It is recommended to further investigate the effect of loading frequency/strain rate on the fatigue damage model. The effect of moisture and environment on the degradation of composite laminates requires extensive research. Other parameters including composite laminate lay-up, loading spectrum, and fibre-matrix interface strength are crucial parameters influencing the integrity and durability of composite components in-service loading. To achieve a comprehensive model, such parameters should be examined precisely.

REFERENCES

- [1] Mallick, P. K., *Composites Engineering Handbook*, Marcel Dekker, Inc., (1997).
- [2] Shokrieh, M. M., *Progressive Fatigue Damage Modeling of Composite Materials*, PHD Thesis, Department of Mechanical Engineering, McGill University, (1996).
- [3] Hibbeler, R. C., *Mechanics of Materials*, Sixth Edition, Pearson Prentice Hall, (2005).
- [4] Dew-Hughes, D. and Way, J. L., *Fatigue of Fiber-Reinforced Plastics: A Review*, *Composites*, (1973), Volume 4, Issue 4, pp. 167-173.
- [5] Wohler, A., *Wohler's Experiments on the Strength of the Materials*, Engineering, (1867).
- [6] Konur, O. and Matthews F. L., *Effects of the Properties of the Constituents on the Fatigue Performance of Composites: A Review*, *Composites*, (1989), Volume 20, Number 4, pp. 317-328.
- [7] Degrieck, J. and Paepegem, W. V., *Fatigue Damage Modelling of Fibre-Reinforced Composites Materials: Review*, *Applied Mechanics Reviews*, (2001), Volume 54, Number 4, pp. 279-300.
- [8] Ramakrishnan, V. and Jayaraman, N., *Mechanistically Based Fatigue-Damage Evolution Model for Brittle Matrix Fibre-Reinforced Composites*, *Journal of Materials Science*, (1993), Volume 28, pp. 5592-5602.
- [9] Varvani-Farahani, A. and Shirazi, A., *A Fatigue Damage Model for (0/90) FRP Composites Based on Stiffness Degradation of 0° and 90° Composite Plies*, *Journal of Reinforced Plastics and Composites*, (2007), Volume 26, Number 13, pp. 1319-1336.

- [10] Epaarachchi, J. A. and Clausen, P. D., *A New Approach to a Fatigue Damage Model for Glass-Fibre Reinforced Plastic Composites*, Proceeding of the Seventh International Conference on Composite Engineering (ICCE/7), D. Hui, Ed., Denver, Colorado, (2000), pp. 211-212.
- [11] Ellyin, F. and El-Kadi, H., *A Fatigue Failure Criterion for Fibre Reinforced Composite Laminae*, Composite Structures, (1990), Volume 15, Number 1, pp. 61-74.
- [12] Hashin, Z. and Rotem, A., *A Fatigue Criterion for Fibre Reinforced Composite Materials*, Journal of Composite Materials, (1973), Volume 7, Number 4, pp. 448-464.
- [13] Hwang, W., and Han, K. S., *Cumulative Damage Modulus and Multi-Stress Fatigue Life Prediction*, Journal of Composite Materials, (1986), Volume 20, Number 2, pp. 125-153.
- [14] Whitworth, H. A., *Evaluation of the Residual Strength Degradation in Composite Laminates under Fatigue Loading*, Composite Structures, (2000), Volume 48, Number 4, pp. 261-264.
- [15] Schön, J., *A Model of Fatigue Delamination in Composites*, Composites Science and Technology, (2000), Volume 60, Issue 4, pp. 553-558.
- [16] Biner, S. B. and Yuhas, V. C., *Growth of Short Fatigue Cracks at Notches in Woven Fibre Glass Reinforced Polymeric Composites*, Journal of Engineering Materials and Technology, (1989), Volume 111, Number 4, pp. 363-367.
- [17] Reifsnider, K. L., *The Critical Element Model: A Modeling Philosophy*, Engineering Fracture Mechanics, (1986), Volume 25, Issue 5-6, pp. 739-749.
- [18] Shirazi, A. *Fatigue Damage Modelling Based on Cracking Progress in Unidirectional and Cross-Ply FRP Composites*, MSc. Thesis, Department of Mechanical Engineering, Ryerson University, (2006).

- [19] Brondsted, P., Lilholt, H., and Lystrup, A., *Composite Materials for Wind Power Turbine Blades*, Annual Review of Materials Research, (2005), Volume 35, Issue 1, pp. 505-538.
- [20] Callister, W. D., *Material Science and Engineering An Introduction*, Sixth Edition, John Wiley & Sons, Inc., (2003).
- [21] Panbechi, M., *Fatigue Damage Assessment of Unidirectional GRP and CFRP Composites*, MAsc. Thesis, Department of Mechanical and Industrial Engineering, Ryerson University, (2005).
- [22] Azzi, V. D. and Tsai, S. W., *Anisotropic Strength of Composites*, Experimental Mechanics, (1965), Volume 5, Number 9, pp. 283-288.
- [23] Kawai, M., *A Phenomenological Model for Off-Axis Fatigue Behavior of Unidirectional Polymer Matrix Composites Under Different Stress Ratios*, Composites: Part A, (2004), Volume 35, Issue 7-8, pp. 955-963.
- [24] Jones, R. M., *Mechanics of Composite Materials*, Second Edition, Philadelphia, PA: Taylor & Francis, (1999).
- [25] Nielsen, L. E., *Mechanical Properties of Polymers and Composites*, Volume 1, Marcel Dekker, Inc., New York, (1974).
- [26] Ward, I. M. and Sweeney, J., *An Introduction to The Mechanical Properties of Solid Polymers*, Second Edition, John Wiley & Sons, Inc., (2004).
- [27] Riley, W. F., Sturges, L. D., and Morris, D. H., *Mechanics of Materials*, Sixth Edition, John Wiley & Sons, Inc., (2007).
- [28] Shen, C. -H. and Springer G. S., *Effects of Moisture and Temperature on the Tensile Strength of Composites Materials*, Journal of Composite Materials, (1977), Volume 11,

Number 1, pp. 2-16.

- [29] Shen, C. -H. and Springer G. S., *Environmental Effects on the Elastic Moduli of Composite Materials*, Journal of Composite Materials, (1977), Volume 11, Number 3, pp. 250-264.
- [30] Miyano, Y., Nakada, M., and Kudoh, H., *Prediction of Tensile Fatigue Life for Unidirectional CFRP*, Journal of Composite Materials, (2000), Volume 34, Number 7, pp. 538-550.
- [31] Aklonis, J. J., MacKnight, W. J., and Shen, M., *Introduction to Polymer Viscoelasticity*, John Wiley & Sons, Inc., (1972).
- [32] Thorne, J. L., *Technology of Thermoforming*, Hanser/Gardner Publications, Inc., (1996).
- [33] Reed, R. P. and Golda, M., *Cryogenic Properties of Unidirectional Composites*, Cryogenics, (1994), Volume 34, Number 11, pp. 909-928.
- [34] Jen, M. -H. R., Tseng, Y. -C., Kung, H. -K., and Huang, J. -C., *Fatigue Response of APC-2 Composite Laminates at Elevated Temperatures*, Composites: Part B, (2008), Volume 39, Issue 7-8, pp. 1142-1146.
- [35] Hofer, K. E., JR., Larsen, D., and Humphreys, V. E., *Development of Engineering Data on the Mechanical and Physical Properties of Advanced Composites Materials*, Technical Report AFML-TR-72-205, Part II, (1974), Air force Materials Laboratory, Air force System Command, Wright-Patterson Air force Base, Dayton, Ohio.
- [36] Hertz, J., *Investigation into the High-Temperature Strength Degradation of Fibre-Reinforced Resin Composite During Ambient Aging*, Report No. GDCA-DBG73-005, Contract NAS8-27435, (1973), Convair Aerospace Division, General Dynamics Corporation.

- [37] Browning, C. E., Husman, G. E., and Withney, J. M., *Moisture Effects in Epoxy Matrix Composites*, Composite Materials: Testing and Design, ASTM, STP 617, (1976).
- [38] Kaminski, B. E., *Effects of Specimen Geometry on the Strength of Composite Materials*, Analysis of the Test Methods for High Modulus Fibres and Composites, ASTM STP521, (1973).
- [39] Husman, G. E., *Characterization of Wet Composite Materials*, Presented at the Mechanics of Composites Review, Bergamo Centre, Dayton, Ohio, (1976).
- [40] Kawai, M. and Taniguchi, T., *Off-Axis Fatigue Behavior of Plain Weave Carbon/Epoxy Fabric Laminates at Room and High Temperatures and Its Mechanical Modeling*, Composites: Part A, (2006), Volume 37, Issue 2, pp. 243-256.
- [41] Hiwa, C., Ueda, S.-I., and Nakagawa, T., *Effect of Ambient Temperature on the Fatigue Life of GFRP Composites*, Memories of the Faculty of Engineering, Kobe University, (1986), Number 33, pp. 15-23.

APPENDIX A

Testing Conditions and Mechanical Properties

To assess the proposed temperature dependent monotonic and fatigue models, the amounts of all the constitutive parameters of the models for different specimens and test conditions have been extracted from literature. In this appendix, the information is tabulated and presented for reference and possible future use. The information is listed in Tables A-1 to A-7. There has been a great effort to extract the information from the original literature as accurately as possible. All the specimens used in the references are unnotched.

Table A-1: Summary of the experimental information used for the evaluation of the proposed $\sigma_{ult} - T$ relation.

Composite	Reference	Ply/Laminates	Fibre Volume Fraction, V_f [%]	Ultimate Tensile Strength at RT, σ_{ult} (RT) [MPa]
Boron/Epoxy	[33]	0°	50	1400 (295 K)
Aramid/Epoxy	[33]	0°	60	1400 (295 K)
S-glass/Epoxy	[33]	0°	---	1600 (295 K)
E-glass/Epoxy	[33]	0°	70	1100 (295 K)
Alumina/PEEK	[33]	0°	45	800 (295 K)
AS-4/PEEK	[34]	[0/90] _{4S}	61	1068.4 (298 K)
AS-4/PEEK	[34]	[0/+45/90/-45] _{2S}	61	730.4 (298 K)
Thornel 300/Fiberite 1034	[28]	90°	---	58.6 (300 K)
Thornel 300/Narmco 5208	[28]	90°	---	40.4 (300 K)
HT-S/(8183/137-NDA-BF ₃ :MEA)	[28]	90°	---	49.5 (300 K)
Herculus AS-5/3501	[28]	90°	63	54.8 (300 K)
Boron/Narmco 5505	[28]	90°	---	109.9 (300 K)

Table A-2: Summary of the experimental information (extrapolated and reported) used for the evaluation of the proposed $\sigma_{ult} - T$ relation.

Composite	Reference	Ply/Laminates	Corresponding Constant C (Extrapolated)	Polymer Melting Point, T_m [K] (Extrapolated)
Boron/Epoxy	[33]	0°	0.3	450
Aramid/Epoxy	[33]	0°	0	450
S-glass/Epoxy	[33]	0°	0.25	450
E-glass/Epoxy	[33]	0°	0.2	450
Alumina/PEEK	[33]	0°	0.25	616
AS-4/PEEK	[34]	[0/90] _{4S}	0.4	616 (Reported)
AS-4/PEEK	[34]	[0/+45/90/-45] _{2S}	0.2	616 (Reported)
Thornel 300/Fiberite 1034	[28]	90°	0.4	431
Thornel 300/Narmco 5208	[28]	90°	0.4	532
HT-S/(8183/137-NDA-BF ₃ :MEA)	[28]	90°	0.3	457
Herculus AS-5/3501	[28]	90°	0.2	474
Boron/Narmco 5505	[28]	90°	0.3	546

Table A-3: Summary of the experimental information used for the evaluation of the proposed $E-T$ relation.

Composite	Reference	Plies/Laminates	Fibre Volume Fraction, V_f [%]	Young's Modulus at RT, $E(RT)$ [MPa]
Boron/Epoxy	[33]	0°	50	210000 (295 K)
Aramid/Epoxy	[33]	0°	60	80000 (295 K)
S-glass/Epoxy	[33]	0°	---	57000 (295 K)
E-glass/Epoxy	[33]	0°	70	43000 (295 K)
Alumina/PEEK	[33]	0°	45	90000 (295 K)
AS-4/PEEK	[34]	[0/90] _{4S}	61	77680 (298 K)
AS-4/PEEK	[34]	[0/+45/90/-45] _{2S}	61	55010 (298 K)
Thornel 300/Fiberite 1034	[29]	90°	---	7375 (300 K)
Thornel 300/Narmco 5208	[29]	90°	---	9042 (300 K)
HT-S/(8183/137-NDA-BF ₃ :MEA)	[29]	90°	---	3433 (300 K)
Courtaulds HMS/Herculus 3002M	[29]	90°	---	6979 (300 K)

Table A-4: Summary of the experimental information (extrapolated and reported) used for the evaluation of the proposed $E-T$ relation.

Composite	Reference	Ply/Laminates	Corresponding Constant C (Extrapolated)	Polymer Melting Point, T_m [K] (Extrapolated)
Boron/Epoxy	[33]	0°	0.1	450
Aramid/Epoxy	[33]	0°	0.25	450
S-glass/Epoxy	[33]	0°	0.1	450
E-glass/Epoxy	[33]	0°	0.1	450
Alumina/PEEK	[33]	0°	0.1	616
AS-4/PEEK	[34]	[0/90] _{4S}	0.1	616 (Reported)
AS-4/PEEK	[34]	[0/+45/90/-45] _{2S}	0.1	616 (Reported)
Thornel 300/Fiberite 1034	[29]	90°	0.2	431
Thornel 300/Narmco 5208	[29]	90°	0.2	532
HT-S/(8183/137-NDA-BF ₃ :MEA)	[29]	90°	0.3	457
Courtaulds HMS/Herculus 3002M	[29]	90°	0.1	550

Table A-5: Summary of the experimental information used for the evaluation of the proposed $A-T$, $m-T$, and the temperature dependant S-N relation.

Composite	Reference	Ply/Laminates	Fibre Volume Fraction, V_f [%]	Intercept at RT, $A(RT)$ [MPa]
AS-4/PEEK	[34]	[0/90] _{4S}	61	1207.2 (298 K)
AS-4/PEEK	[34]	[0/+45/90/-45] _{2S}	61	787.6 (298 K)
T300/Epoxy#2500	[40]	Plain-Woven (15°)	---	267.2 (298 K)
T300/Epoxy#2500	[40]	Plain-Woven (30°)	---	204.4 (298 K)
T300/Epoxy#2500	[40]	Plain-Woven (45°)	---	186.8 (298 K)

Table A-6: Summary of the experimental information (extrapolated and reported) used for the evaluation of the proposed $A-T$, $m-T$, and the temperature dependant S-N relation.

Composite	Reference	Plies/Laminates	Corresponding Constant C (Extrapolated)	Polymer Melting Point, T_m [K] (Extrapolated)
AS-4/PEEK	[34]	[0/90] _{4S}	0.4	616 (Reported)
AS-4/PEEK	[34]	[0/+45/90/-45] _{2S}	0.2	616 (Reported)
T300/Epoxy#2500	[40]	Plain-Woven (15°)	0.7	603
T300/Epoxy#2500	[40]	Plain-Woven (30°)	0.85	603
T300/Epoxy#2500	[40]	Plain-Woven (45°)	0.9	603

Table A-7: Summary of the experimental information extracted from Hiwa *et al.* [41] for glass cloth/polyvinyl ester and glass mat/polyvinyl ester used for the evaluation of the proposed temperature dependant fatigue damage model.

Material at T [K]	E_c [MPa]	σ_{ult} [MPa]
Cloth at 298	24000	431
Mat at 298	13900	251

Material at T [K]	T_m [K]	K_f	E_f [MPa]	C for E_c	C for σ_{ult}	V_f	f^*	σ_{max} [MPa]	R	f [Hz]	nN_f [Cycles]
Cloth at 298	433	0.5	78400	0.1	0.2	0.48	0.5	130	0	16.7	67000
Cloth at 323	433	0.5	78400	0.1	0.2	0.48	0.3	130	0	16.7	52000
Cloth at 343	433	0.5	78400	0.1	0.2	0.48	0.1	130	0	16.7	45500
Mat at 298	433	0.375	78400	0.1	0.2	0.35	0.5	90	0	16.7	98939
Mat at 373	433	0.375	78400	0.1	0.2	0.35	0.3	90	0	16.7	95000
Mat at 423	433	0.375	78400	0.1	0.2	0.35	0.1	90	0	16.7	16000

APPENDIX B

Experimental Data

In this appendix, all sets of the experimental data used to evaluate the proposed temperature dependent monotonic and fatigue models are tabulated and presented for reference and possible future use. The data is listed in Tables B-1 to B-38. There has been a great effort to extract the data from the original literature as accurately as possible. All the specimens used in the references are unnotched.

Table B-1: List of the experimental data extracted from Reed and Golda [33] used for the evaluation of the proposed $\sigma_{ult} - T$ and $E - T$ relations for the 0° boron/epoxy composite.

0° Boron/Epoxy		
Temperature, T [K]	Ultimate Tensile Strength, σ_{ult} [MPa]	Young's Modulus, E_t [MPa]
4	1800	240000
76	1700	230000
295	1400	210000

Table B-2: List of the experimental data extracted from Reed and Golda [33] used for the evaluation of the proposed $\sigma_{ult} - T$ and $E - T$ relations for the 0° aramid/epoxy composite.

0° Aramid/Epoxy		
Temperature, T [K]	Ultimate Tensile Strength, σ_{ult} [MPa]	Young's Modulus, E_t [MPa]
4	1400	100000
76	1400	99000
295	1400	80000

Table B-3: List of the experimental data extracted from Reed and Golda [33] used for the evaluation of the proposed $\sigma_{ult} - T$ and $E - T$ relations for the 0° S-glass/epoxy composite.

0° S-glass/Epoxy		
Temperature, T [K]	Ultimate Tensile Strength, σ_{ult} [MPa]	Young's Modulus, E_t [MPa]
4	2000	62000
76	2100	59000
295	1600	57000

Table B-4: List of the experimental data extracted from Reed and Golda [33] used for the evaluation of the proposed $\sigma_{ult} - T$ and $E - T$ relations for the 0° E-glass/epoxy composite.

0° E-glass/Epoxy		
Temperature, T [K]	Ultimate Tensile Strength, σ_{ult} [MPa]	Young's Modulus, E_t [MPa]
4	1300	47000
76	1400	45000
295	1100	43000

Table B-5: List of the experimental data extracted from Reed and Golda [33] used for the evaluation of the proposed $\sigma_{ult} - T$ and $E - T$ relations for the 0° alumina/PEEK composite.

0° Alumina/PEEK		
Temperature, T [K]	Ultimate Tensile Strength, σ_{ult} [MPa]	Young's Modulus, E_t [MPa]
4	1000	100000
76	1300	100000
295	800	90000

Table B-6: List of the experimental data extracted from Jen *et al.* [34] used for the evaluation of the proposed $\sigma_{ult}-T$ and $E-T$ relations for the $[0/90]_{4S}$ AS-4/PEEK composite.

$[0/90]_{4S}$ AS-4/PEEK		
Temperature, T [K]	Ultimate Tensile Strength, σ_{ult} [MPa]	Young's Modulus, E_t [MPa]
300	1068.4	77680
323	1019.6	77040
348	951.2	76700
373	830.16	75230
398	808.42	73530
423	766.68	70640
448	741.01	69810

Table B-7: List of the experimental data extracted from Jen *et al.* [34] used for the evaluation of the proposed $\sigma_{ult} - T$ and $E - T$ relations for the $[0/+45/90/-45]_{2S}$ AS-4/PEEK composite.

$[0/+45/90/-45]_{2S}$ AS-4/PEEK		
Temperature, T [K]	Ultimate Tensile Strength, σ_{ult} [MPa]	Young's Modulus, E_t [MPa]
300	730.42	55010
323	726.73	53290
348	681.07	52680
373	651.85	52090
398	622.27	50680
423	593.51	48510
448	579.64	48350

Table B-8: List of the experimental data extracted from Shen and Springer [28] used for the evaluation of the proposed $\sigma_{ult} - T$ relation for the 90° Thornel 300/Fiberite 1034 composite.

90° Thornel 300/Fiberite 1034	
Temperature, T [K]	Ultimate Tensile Strength, σ_{ult} [MPa]
344.375	50
366.4583	43.75
394.5833	35.5
411.25	21.16667
422.5	12.75

Table B-9: List of the experimental data extracted from Shen and Springer [29] used for the evaluation of the proposed $E-T$ relation for the 90° Thornel 300/Fiberite 1034 composite.

90° Thornel 300/Fiberite 1034	
Temperature, T [K]	Young's Modulus, E_b [MPa]
200	7542
300	7375
367.5	6563
395.8	5521
423.8	3938

Table B-10: List of the experimental data extracted from Shen and Springer [28] used for the evaluation of the proposed $\sigma_{ult} - T$ relation for the 90° Thornel 300/Narmco 5208 composite.

90° Thornel 300/ Narmco 5208	
Temperature, T [K]	Ultimate Tensile Strength, σ_{ult} [MPa]
300	40.41667
400	28.25
450	20

Table B-11: List of the experimental data extracted from Shen and Springer [29] used for the evaluation of the proposed $E-T$ relation for the 90° Thornel 300/Narmco 5208 composite.

90° Thornel 300/ Narmco 5208	
Temperature, T [K]	Young's Modulus, E_t [MPa]
300	9042
366.7	8688
394.2	8354
421.9	7375

Table B-12: List of the experimental data extracted from Shen and Springer [28] used for the evaluation of the proposed $\sigma_{ult} - T$ relation for the 90° HT-S/(8183/137-NDA-BF₃:MEA) composite.

90° HT-S/(8183/137-NDA-BF₃:MEA)	
Temperature, T [K]	Ultimate Tensile Strength, σ_{ult} [MPa]
217.3611	64.06944
301.7361	49.58333
394.0972	38.79167
449.6528	7.777778

Table B-13: List of the experimental data extracted from Shen and Springer [29] used for the evaluation of the proposed $E-T$ relation for the 90° HT-S/(8183/137-NDA-BF₃:MEA) composite.

90° HT-S/(8183/137-NDA-BF₃:MEA)	
Temperature, T [K]	Young's Modulus, E_t [MPa]
217.1	3222
302.6	3433
400.4	2600
450	433.3

Table B-14: List of the experimental data extracted from Shen and Springer [28] used for the evaluation of the proposed $\sigma_{ult} - T$ relation for the 90° Hercules AS-5/3501 composite.

90° Hercules AS-5/3501	
Temperature, T [K]	Ultimate Tensile Strength, σ_{ult} [MPa]
300	54.83333
366.875	50.91667
394.7917	45.33333
422.2917	37.6667

Table B-15: List of the experimental data extracted from Shen and Springer [28] used for the evaluation of the proposed $\sigma_{ult} - T$ relation for the 90° boron/Narmco 5505 composite.

90° Boron/Narmco 5505	
Temperature, T [K]	Ultimate Tensile Strength, σ_{ult} [MPa]
300	109.901
377.5248	90.59406
450	75.74257
488.3168	56.13861

Table B-16: List of the experimental data extracted from Shen and Springer [29] used for the evaluation of the proposed $E-T$ relation for the 90° Courtaulds HMS/Herculus 3002M composite.

90° Courtaulds HMS/Herculus 3002M	
Temperature, T [K]	Young's Modulus, E_t [MPa]
300	6979
400	6583
450	6208

Table B-17: List of the experimental S-N data extracted from Jen *et al.* [34] used for the evaluation of the proposed $A-T$, $m-T$ and S-N relations for the $[0/90]_{4S}$ AS-4/PEEK composite at 298 K.

$f = 5 \text{ Hz}, R = 0.1, \text{ and } T = 298 \text{ K}$	
Number of Cycles to Failure, N_f [Cycles]	Maximum Stress, σ_{max} [MPa]
1000000	571.3
1000000	629.17
429866.2	688.52
123499.9	747.88
52079.48	807.24
7498.942	905.17
3414.549	963.04
114.3756	983.82
58.43414	1043.2
1	1068.4

Table B-18: List of the experimental S-N data extracted from Jen *et al.* [34] used for the evaluation of the proposed $A-T$, $m-T$ and S-N relations for the $[0/90]_{4S}$ AS-4/PEEK composite at 348 K.

$f = 5 \text{ Hz}, R = 0.1, \text{ and } T = 348 \text{ K}$	
Number of Cycles to Failure, N_f [Cycles]	Maximum Stress, σ_{max} [MPa]
1000000	412.52
841395.1	473.36
794328.2	532.72
390541	590.59
22820.93	648.46
2326.305	706.33
1143.756	768.65
101.9373	826.53
66.83439	884.4
1	949.69

Table B-19: List of the experimental S-N data extracted from Jen *et al.* [34] used for the evaluation of the proposed $A-T$, $m-T$ and S-N relations for the $[0/90]_{4S}$ AS-4/PEEK composite at 373 K.

$f = 5 \text{ Hz}, R = 0.1, \text{ and } T = 373 \text{ K}$	
Number of Cycles to Failure, N_f [Cycles]	Maximum Stress, σ_{max} [MPa]
944060.9	394.71
735642.3	412.52
94406.09	471.88
52079.48	531.23
7498.942	590.59
595.6621	648.46
643.1812	707.82
28.18383	767.17
1	829.49

Table B-20: List of the experimental S-N data extracted from Jen *et al.* [34] used for the evaluation of the proposed $A-T$, $m-T$ and S-N relations for the $[0/90]_{4S}$ AS-4/PEEK composite at 398 K.

$f = 5 \text{ Hz}, R = 0.1, \text{ and } T = 398 \text{ K}$	
Number of Cycles to Failure, N_f [Cycles]	Maximum Stress, σ_{max} [MPa]
1000000	333.87
980994.7	373.94
530884.4	412.52
64318.12	471.88
42986.62	531.23
5207.948	590.59
841.3951	649.94
908.5176	707.82
68.12921	767.17
1	807.24

Table B-21: List of the experimental S-N data extracted from Jen *et al.* [34] used for the evaluation of the proposed $A-T$, $m-T$ and S-N relations for the $[0/90]_{4S}$ AS-4/PEEK composite at 423 K.

$f = 5 \text{ Hz}, R = 0.1, \text{ and } T = 423 \text{ K}$	
Number of Cycles to Failure, N_f [Cycles]	Maximum Stress, σ_{max} [MPa]
1000000	314.58
368694.5	344.26
77243	353.17
34807.01	373.94
7356.423	433.3
1267.281	490.67
370	569.81
128.3315	648.46
64.31812	727.11
1	765.69

Table B-22: List of the experimental S-N data extracted from Jen *et al.* [34] used for the evaluation of the proposed $A-T$, $m-T$ and S-N relations for the $[0/+45/90/-45]_{2S}$ AS-4/PEEK composite at 298 K.

$f = 5 \text{ Hz}, R = 0.1, \text{ and } T = 298 \text{ K}$	
Number of Cycles to Failure, N_f [Cycles]	Maximum Stress, σ_{max} [MPa]
1.00E+06	482.89
9.62E+05	493.03
6.68E+05	512.31
63096	571.15
11438	610.71
5207.9	631
891.25	650.28
1211.5	669.55
90.852	688.83
1	730.42

Table B-23: List of the experimental S-N data extracted from Jen *et al.* [34] used for the evaluation of the proposed $A-T$, $m-T$ and S-N relations for the $[0/+45/90/-45]_{2S}$ AS-4/PEEK composite at 348 K.

$f = 5 \text{ Hz}, R = 0.1, \text{ and } T = 348 \text{ K}$	
Number of Cycles to Failure, N_f [Cycles]	Maximum Stress, σ_{max} [MPa]
8.91E+05	393.62
1.12E+05	433.18
4.22E+04	452.45
94406	492.02
10194	531.58
643.18	571.15
520.79	610.71
60.72	649.26
1	681.73

Table B-24: List of the experimental S-N data extracted from Jen *et al.* [34] used for the evaluation of the proposed $A-T$, $m-T$ and S-N relations for the $[0/+45/90/-45]_{2S}$ AS-4/PEEK composite at 373 K.

$f = 5 \text{ Hz}, R = 0.1, \text{ and } T = 373 \text{ K}$	
Number of Cycles to Failure, N_f [Cycles]	Maximum Stress, σ_{max} [MPa]
1.00E+06	344.92
6.43E+05	365.21
1.02E+05	394.63
18127	473.76
794.33	550.86
246.41	591.44
73.564	631
1	652.31

Table B-25: List of the experimental S-N data extracted from Jen *et al.* [34] used for the evaluation of the proposed $A-T$, $m-T$ and S-N relations for the $[0/+45/90/-45]_{2S}$ AS-4/PEEK composite at 398 K.

$f = 5 \text{ Hz}, R = 0.1, \text{ and } T = 398 \text{ K}$	
Number of Cycles to Failure, N_f [Cycles]	Maximum Stress, σ_{max} [MPa]
1.00E+06	315.5
8.25E+05	335.79
98099	374.34
1.02E+05	413.9
76442	433.18
36169	472.74
9261.2	512.31
107.98	551.87
56.234	590.42
1	622.89

Table B-26: List of the experimental S-N data extracted from Jen *et al.* [34] used for the evaluation of the proposed $A-T$, $m-T$ and S-N relations for the $[0/+45/90/-45]_{2S}$ AS-4/PEEK composite at 423 K.

$f = 5 \text{ Hz}, R = 0.1, \text{ and } T = 423 \text{ K}$	
Number of Cycles to Failure, N_f [Cycles]	Maximum Stress, σ_{max} [MPa]
1.00E+06	296.23
7.36E+05	315.5
2.61E+05	334.78
1.24E+05	355.07
89125	393.62
60720	411.27
2417.3	472.74
146.78	512.31
56.234	551.87
1	593.47

Table B-27: List of the experimental S-N data extracted from Kawai and Taniguchi [40] used for the evaluation of the proposed $A-T$, $m-T$ and S-N relations for the plain-woven (15°) T300/Epoxy#2500 composite at 298 K.

$f = 10 \text{ Hz}, R = 0.1, \text{ and } T = 298 \text{ K}$	
Number of Cycles to Failure, N_f [Cycles]	Maximum Stress, σ_{max} [MPa]
1.02E+06	145
8.70E+04	161
4.68E+03	164
3919.2	167
3004.8	174
0.5	293

Table B-28: List of the experimental S-N data extracted from Kawai and Taniguchi [40] used for the evaluation of the proposed $A-T$, $m-T$ and S-N relations for the plain-woven (15°) T300/Epoxy#2500 composite at 373 K.

$f = 10 \text{ Hz}, R = 0.1, \text{ and } T = 373 \text{ K}$	
Number of Cycles to Failure, N_f [Cycles]	Maximum Stress, σ_{max} [MPa]
1.02E+06	85
3.36E+03	87
7.96E+02	112
623.91	123
467.87	134
0.5	223

Table B-29: List of the experimental S-N data extracted from Kawai and Taniguchi [40] used for the evaluation of the proposed $A-T$, $m-T$ and S-N relations for the plain-woven (30°) T300/Epoxy#2500 composite at 298 K.

$f = 10 \text{ Hz}, R = 0.1, \text{ and } T = 298 \text{ K}$	
Number of Cycles to Failure, N_f [Cycles]	Maximum Stress, σ_{max} [MPa]
1.02E+06	94
4.58E+03	100
3.00E+03	105
1239.4	118
652.16	141
0.5	236

Table B-30: List of the experimental S-N data extracted from Kawai and Taniguchi [40] used for the evaluation of the proposed $A-T$, $m-T$ and S-N relations for the plain-woven (30°) T300/Epoxy#2500 composite at 373 K.

$f = 10 \text{ Hz}, R = 0.1, \text{ and } T = 373 \text{ K}$	
Number of Cycles to Failure, N_f [Cycles]	Maximum Stress, σ_{max} [MPa]
9.93E+05	43
4.19E+03	47
2.11E+03	51
1239.4	60
0.5	168

Table B-31: List of the experimental S-N data extracted from Kawai and Taniguchi [40] used for the evaluation of the proposed $A-T$, $m-T$ and S-N relations for the plain-woven (45°) T300/Epoxy#2500 composite at 298 K.

$f = 10 \text{ Hz}, R = 0.1, \text{ and } T = 298 \text{ K}$	
Number of Cycles to Failure, N_f [Cycles]	Maximum Stress, σ_{max} [MPa]
1.02E+06	75
7.96E+03	81
4.10E+03	85.5
2573.4	91
1134.3	108
0.5	221

Table B-32: List of the experimental S-N data extracted from Kawai and Taniguchi [40] used for the evaluation of the proposed $A-T$, $m-T$ and S-N relations for the plain-woven (45°) T300/Epoxy#2500 composite at 373 K.

$f = 10 \text{ Hz}, R = 0.1, \text{ and } T = 373 \text{ K}$	
Number of Cycles to Failure, N_f [Cycles]	Maximum Stress, σ_{max} [MPa]
1.00E+06	36
5.23E+03	40
2.76E+03	43
1212.2	51
850.63	58
0.5	150

Table B-33: List of the D-N data extracted from Hiwa *et al.* [41] used for the evaluation of the proposed D-N relation for the glass cloth/polyvinyl ester composite at 298 K.

$\sigma_{max} = 130 \text{ MPa}, f = 16.7 \text{ Hz}, R = 0, \text{ and}$ $T = 298 \text{ K}$	
Number of Cycles to Failure, N_f [Cycles]	Damage, D
0	0
10560	0.135011
20720	0.175057
30800	0.19222
40400	0.204806
50080	0.256293
60080	0.338673
65280	0.414188
66240	0.466819

Table B-34: List of the D-N data extracted from Hiwa *et al.* [41] used for the evaluation of the proposed D-N relation for the glass cloth/polyvinyl ester composite at 323 K.

$\sigma_{max} = 130 \text{ MPa}, f = 16.7 \text{ Hz}, R = 0, \text{ and}$ $T = 323 \text{ K}$	
Number of Cycles to Failure, N_f [Cycles]	Damage, D
0	0
10560	0.135011
20720	0.208238
30720	0.244851
40320	0.298627
45360	0.343249
49600	0.354691
50160	0.375286
51280	0.485126

Table B-35: List of the D-N data extracted from Hiwa *et al.* [41] used for the evaluation of the proposed D-N relation for the glass cloth/polyvinyl ester composite at 343 K.

$\sigma_{max} = 130 \text{ MPa}, f = 16.7 \text{ Hz}, R = 0, \text{ and}$ $T = 343 \text{ K}$	
Number of Cycles to Failure, N_f [Cycles]	Damage, D
0	0
10560	0.135011
20720	0.208238
30720	0.244851
35280	0.2746
40320	0.298627
44240	0.326087
44960	0.363844

Table B-36: List of the D-N data extracted from Hiwa *et al.* [41] used for the evaluation of the proposed D-N relation for the glass mat/polyvinyl ester composite at 298 K.

$\sigma_{max} = 90 \text{ MPa}, f = 16.7 \text{ Hz}, R = 0, \text{ and}$ $T = 298 \text{ K}$	
Number of Cycles to Failure, N_f [Cycles]	Damage, D
0	0
9828.571	0.012732
19657.14	0.021991
29600	0.060185
49942.86	0.06713
59885.71	0.068287
69942.86	0.078704
74514.29	0.087963
39885.71	0.092593
80114.29	0.118056
89942.86	0.138889
95200	0.178241
97028.57	0.199074

Table B-37: List of the D-N data extracted from Hiwa *et al.* [41] used for the evaluation of the proposed D-N relation for the glass mat/polyvinyl ester composite at 373 K.

$\sigma_{max} = 90 \text{ MPa}$, $f = 16.7 \text{ Hz}$, $R = 0$, and $T = 373 \text{ K}$	
Number of Cycles to Failure, N_f [Cycles]	Damage, D
0	0
4457.143	0.048611
9942.857	0.064815
19885.71	0.153935
29600	0.173611
49942.86	0.200571
60114.29	0.209491
39885.71	0.215278
74742.86	0.22338
84914.29	0.246528
89942.86	0.266204
90857.14	0.28588

Table B-38: List of the D-N data extracted from Hiwa *et al.* [41] used for the evaluation of the proposed D-N relation for the glass mat/polyvinyl ester composite at 423 K.

$\sigma_{max} = 90 \text{ MPa}$, $f = 16.7 \text{ Hz}$, $R = 0$, and $T = 423 \text{ K}$	
Number of Cycles to Failure, N_f [Cycles]	Damage, D
0	0
4457.143	0.083333
9942.857	0.125
13942.86	0.143519
14971.43	0.173611